Digital Control of Superconducting Quantum Bits

by

Edward Matthew Leonard Jr.

A dissertation submitted in partial fulfillment of
the requirements for the degree of

Doctor of Philosophy

(Physics)

at the

UNIVERSITY OF WISCONSIN–MADISON

2018

Date of final oral examination: 28 August 2018

The dissertation is approved by the following members of the Final Oral Committee:

Robert McDermott, Professor, Physics

Mark Eriksson, Professor, Physics

Maxim Vavilov, Professor, Physics

Chang-Beom Eom, Professor, Materials Science & Engineering

ACKNOWLEDGMENTS

There are many people who have in no small way contributed to my time in graduate school, whether their support came in the lab, at home, or anywhere between.

First, and, without any measure of doubt, foremost, I must express my greatest professional gratitude to my advisor Prof. Robert McDermott. When I first approached Robert (Spring '13), I informed him that the extent of my experimental experience was limited to my educational laboratories during my undergraduate studies. He quickly assured me that I'd learn, and I've been working towards making that a true statement since. Robert continued to push me, along with my fellow group members, to be better scientists and engineers than when we first started working with him, and I can certainly say that nothing has been a harder exterior driving force than he in my own professional development.

Beyond Robert, the group wouldn't be what it is today without her people. My project brother Matt and I spent countless hours bringing up a reliable cleanroom process and experimental protocols for the work presented in this thesis, and I can't imagine how long it would have taken if either of us tried to go it alone. I will never forget the months in which we would meet in the morning at the cleanroom, spend the day between the WCAM and Chamberlin Hall, and catch the last bus home in the evening only to repeat it again the next day. Matt and I became friends both in and out of the lab during our time at Wisconsin, and I look forward to seeing he and his family on the East Coast in the future. We also had mentors for various parts along the way: Shaojiang taught me multilayer fabrication and how to make and test Josephson junctions while Umesh demonstrated how to bring up a new process; Ted showed me how to measure and how to care for the details that really matter while not sweating the small stuff; Ivan and Guilhem gave us `experiment.py` and stressed the importance of carefully conducted experiments and proper coding practices; Brad showed us that really, reality isn't real, and that interpretation of the data is always easier when using your arms as pretend state vectors; and Dave gave us a wet DR.

Everyone else in the McDermott Research Ranch (MR^2) has had a positive impact on my time here. Joey was never afraid to attack low-level problems and help debug fabrication or hardware issues. Chris brought up our group's qubit process once we had access to EBL and solved coding issues with a reasoned approach. Alex knew better than most of us how to relax while also being one of the most effective and thoughtful researchers that the group has seen in my tenure. Naveen has grown quickly into a competent researcher and always has just one…small…question with the intent to truly understand what is being said. Once we include Ryan, J.P., and Nathan (our dot family) from across the hall, and the multitude of undergraduate students who have passed through Robert's lab, it's hard to

imagine a better group of folks with whom I could have spent my professional time here as a student.

Whenever I had time to leave the lab, I always had a warm home to which I could return. The inhabitants and members of House on the Rocks – Madison's premiere and relatively non-exclusive nightclub – granted me the easy ability to change gears from work and added a certain spice to life outside the lab. I specifically need to thank Clint and Greg, both of whom were there when the foundation was laid, and also Laura, Laser, Dillon, and Janell for always keeping a warm and welcoming home. As for our frequent visitors and club members – Brian (The Patrón Saint), Laser (The Pet), Ruben (The Amigo), and Tom (The Ambassador) – thanks for sharing and representing the ideals of HotR where ever you may be. There are also several people from my previous life at Michigan Tech with whom I've had the great fortune to stay in touch, and while I can't list every name I will specifically thank the gang – Cameron, Liz, Olivia, and Ruben – for being patient with my sometimes extra-long response times while I was swamped with school; I hope we can all get together again soon!

One of the greatest benefits of choosing Wisconsin for graduate school was the ability to see most of my immediate family on a regular basis. My mother and father along with my grandpa, great-aunt, great-uncle, and many more loved ones have been immensely supportive for the past 10 years of my post-secondary education, and I owe them all the world for that. But while everyone listed above has done everything and more to help propel me to where I am today, there is no driving force in my personal and professional life stronger than that provided by my late grandmother, Carolyn. Carolyn supported me during my youth in every endeavor in which I participated and also pushed me towards goals and objectives that, while I might not have understood it at the time, were ultimately always and only in my best interest. When I was in kindergarten, Carolyn would sometimes pick me up from school; when I was old enough to enjoy it, she made sure that we went to a Green Bay Packer game at least once every season; and we had several vacations where it was just the two of us (most notably: a train trip to the West Coast and back remains one of my most fond vacation memories to date). For all the time in between, she was supportive, loving, and caring while pushing me in a positive direction and her excitement about my accomplishments, big and small, was always welcome (truth be told, I think she was probably more enthusiastic about my going to college than I was). Finishing graduate school is my biggest achievement thus far in life, and I owe more than I can ever repay to Carolyn for the motivation to get this far.

I loved my grandma, and it is to her that I dedicate this work.

For Granny

Go Pack Go!

ABSTRACT

Fault-tolerant quantum computation requires high-fidelity control of qubit states. In superconducting qubits based on Josephson circuits, this is typically achieved via the application of microwave packets generated by mixing the output of a coherent source with an intermediate frequency tone generated and shaped using arbitrary waveform generators. This control style has seen tremendous success, enabling the high-fidelity control of systems comprising many-tens of qubits. However, as systems now scale towards thousands of qubits, the overhead microwave hardware and number of necessary connections to the quantum processor becomes staggering. This will eventually impart a larger-than-practical heat-load on a state-of-the-art large-scale DR. A perhaps natural co-processor technology to superconducting qubits is the family of superconducting electronics based on the Rapid Single Flux Quantum (RSFQ) style of logic circuits, which has been the subject of intense research for the past 30 years and has matured to the point of enabling the construction of complex superconducting arithmetic logic units in a variety of flavors of RSFQ technologies. In this thesis, we present progress towards the integration of superconducting qubits with a simple circuit from the RSFQ family of digital superconducting electronics. A dc/SFQ pulse generator circuit is cofabricated on the same chip as a transmon qubit. Inspired by some early practitioners of nuclear magnetic resonance and their DANTE pulse sequence, we use single flux quantum pulse trains – flux pulses which are quantized to the superconducting flux quantum and pulse-to-pulse timings which are set by the qubit precession period – to drive coherent rotations of the transmon state. We measure the error of our quantum gates in this control scheme using randomized benchmarking and find gate fidelities around 95%. We then characterize the loss in our quantum system in the form of quasiparticle poisoning as a result of operation of the dc/SFQ converter. We conclude with a brief discussion of straightforward improvements to mitigate the deleterious effects of quasiparticles on the quantum circuit and discuss the scalability of this technology in the context of Josephson quantum computing.

Funding and Support

Most of the work in this thesis was supported by the U.S. Government by the Office of the Director of National Intelligence (ODNI), Intelligence Advanced Research Project Activity (IARPA), through Army Research Office Grant Nos. W911NF-14-1-0080 and W911NF-15-1-0248 and by the National Science Foundation (NSF) under Grant Nos. QIS-1720304 and QIS-1720312. Portions of this work were performed at the Wisconsin Center for Applied Microelectronics, a research core facility managed by the College of Engineering Shared Research Facilities and supported by the University of Wisconsin - Madison. Other portions were performed at the Cornell NanoScale Facility, a member of the National Nanotechnology Coordinated Infrastructure (NNCI), which is supported by the NSF under Grant No. ECCS-1542081. Microscopy and materials analysis infrastructure and instrumentation used for this work were supported by the NSF through the University of Wisconsin Materials Research Science and Engineering Center (UW-MRSEC, DMR-1720415). The views and conclusions contained in this document are those of the author and should not be interpreted as representing the official policies, either expressed or implied, of the Board of Regents of the University of Wisconsin System, IARPA, ODNI, NSF, or the U.S. Government.

CONTENTS

LIST OF FIGURES

LIST OF TABLES

1 INTRODUCTION

Computing technology has been the benefactor of significant advances since the first reports of programmable electronic digital computers in the late 1940s into the early 1950s [1]. Indeed, one of the calculations used as a benchmark by Williams in 1948 [2, 3] was simply the long division of $(2^{30}\text{-}1)/31$; their report indicates that their machine took about 1.5 seconds to complete this calculation! At around the same time as this, and spurred by the need for such a device, the transistor was devised to replace then state-of-the-art vacuum tubes as supports of computational information [4]; it is this invention which has spurred the now global effort to squeeze every last ounce of power from classical computational resources. Since then, transistors have been miniaturized to be impossibly small (reported many-atom transistors have reached the 1 nm length scale [5]) and classical computational power has increased at an exponential rate, faithfully following the predictions of Moore [6] for many decades.

The enormous success of classical computing has enabled the calculation and simulation of a great many physical systems, both classical and quantum mechanical; in crude terms, if one is able to write a Hamiltonian which is faithful to the physical system, it in principle can be simulated by a classical machine. This has been done for several small quantum systems. However, simulating a *large* quantum mechanical system on a classical computer can be enormously difficult even for a modestly-sized machine due to the exponential memory requirements – where a classical system of N objects can typically be described by $\mathcal{O}(N)$ bits of information, an entangled quantum mechanical system requires an exponentially harder $\mathcal{O}(2^N)$ bits. This begs the question: if it is quantum mechanics which we are set to simulate, why not use a quantum mechanical system to do so? Of course, this is hard; real-world quantum systems are open to the world which means they can couple to sources of unwanted influence or dissipation (decoherence). In controlled quantum systems which exist today, a great deal of care has gone into the engineering of the unavoidable qubit-

environment coupling while balancing the necessary qubit-control/measurement coupling required to build an effective quantum machine. So far, there has been a great deal of success; in the last two decades or so, progress has been fast and vast in the construction of small-scale quantum bit (qubit) arrays. While the motivator for all of this research could be inferred from the above – the plain desire to efficiently simulate a quantum mechanical system [7, 8] – there are also many concrete examples of other tangible uses for such a quantum computer. These include, for example, the prime factorization of large composite numbers [9] with applications to cryptography [10], efficient database searching [11], and the efficient simulation of molecular spectra [12–14] with applications in quantum chemistry.

In this thesis, we will largely concentrate on a novel form of control of an open quantum system - the already established superconducting transmon qubit. The details of this will be covered later, and many of the concerns of many-qubit applications and what one will actually do once a large-scale quantum processor is constructed will be left to others[1]. What follows in this Chapter is a brief introduction to qubits in Sec. 1.1 including a non-exhaustive overview of some physical qubit implementations being pursued in modern day research and, in Sec 1.2, a short overview for the rest of this thesis.

1.1 Qubits

1.1.1 Brief Introduction

Maths

A quantum computation comprises a series of quantum logic gates which operate on an array of many quantum bits (qubits). A qubit is a quantum mechanical system which can

[1]Indeed, an in-depth discussion and great detail into the applications of a many-qubit system are outside the scope of this thesis. The inspired reader may be interested in a more rigorous theoretical treatment as available in, e.g., [15].

be defined by a wavefunction

$$|\psi\rangle = \alpha|0\rangle + \beta|1\rangle, \tag{1.1}$$

$$1 = |\alpha|^2 + |\beta|^2, \tag{1.2}$$

where α, β are complex probability amplitudes for each of their respective states and their squares sum to unity. From here, we see that a qubit may exist in a superposition of $|0\rangle$ and $|1\rangle$ instead of the classical bit which is only a binary 0 or 1. This can be represented on the Bloch sphere with

$$\alpha = \cos\frac{\theta}{2} \tag{1.3}$$

$$\beta = e^{i\phi}\sin\frac{\theta}{2}, \tag{1.4}$$

using polar angle θ and azimuthal angle ϕ [depicted in Fig. 1.1]. In matrix form, this is commonly written

$$|\psi\rangle = \alpha\begin{bmatrix}1\\0\end{bmatrix} + \beta\begin{bmatrix}0\\1\end{bmatrix}. \tag{1.5}$$

A quantum system which can be described by this wavefunction can be used as a qubit. While this is a necessary element, there are additional constraints on what is required for a technology to be used in a successful quantum processor [16–18]. It is in this definition in which a small part of the power of using a qubit to perform computation lies; a single qubit state is here described by two quantities while the state of a classical bit is described by a binary option. This scales to N bits of information stored in an N-device classical system and an exponentially larger 2^N bits of classical information stored in an array of N qubits. There have been many physical implementations of real physical systems which can be represented (either exactly or in a good approximation) as a quantum two-level system,

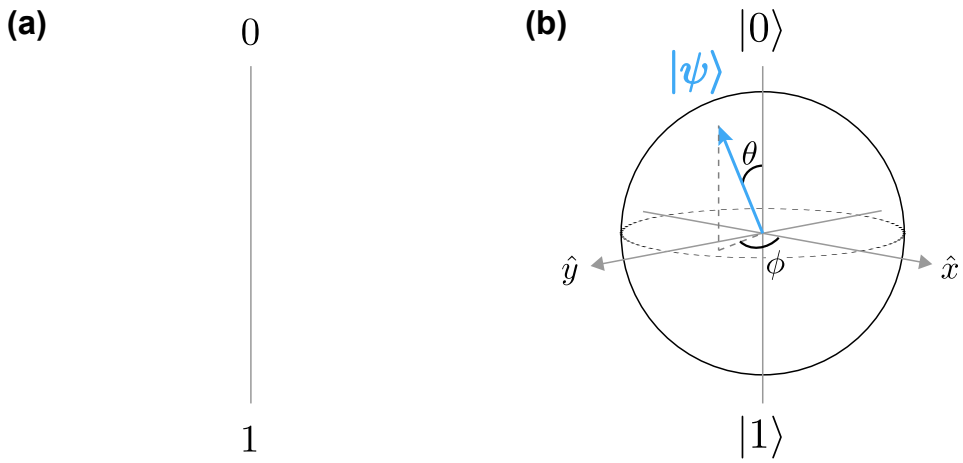

Figure 1.1: Comparison of possible states for a classical versus a quantum bit. **(a)** A classical bit can only be in one of two possible positions: 0 or 1. **(b)** The state of a qubit can be written as a superposition of $|0\rangle$ and $|1\rangle$ and can be fully determined by two quantities: the polar angle θ and azimuthal angle ϕ [15].

some of which are briefly described in the next Section.

Quantum gates act on $|\psi\rangle$ as unitary operators [19], satisfying, for a gate $\hat{U}$, the relation $\hat{U}^\dagger\hat{U} = \hat{I}$. An example is the NOT gate, $\hat{\sigma}_x$, written

$$\hat{\sigma}_x = \begin{bmatrix} 0 & 1 \\ 1 & 0 \end{bmatrix}, \tag{1.6}$$

$$\hat{\sigma}_x \begin{bmatrix} \alpha \\ \beta \end{bmatrix} = \begin{bmatrix} \beta \\ \alpha \end{bmatrix}. \tag{1.7}$$

This is one of the Pauli matrices, $\hat{\sigma}_a$, all of which represent π-rotations about an axis a and can be written

$$\hat{\sigma}_a = \begin{bmatrix} \delta_{az} & \delta_{ax} - i\delta_{ay} \\ \delta_{ax} + i\delta_{ay} & -\delta_{az} \end{bmatrix}, \tag{1.8}$$

where δ_{ij} is the Kronecker Delta. In the later parts of this thesis, we will describe how we use our novel control scheme to achieve both $\hat{\sigma}_x$ and $\hat{\sigma}_y$ gates to control a superconducting

transmon qubit.

Coherence

For a perfect qubit, the system will be prepared in some initial state and it will always be in that state when measured some time later. However, in order to prepare and measure a real qubit, there must be some coupling of the qubit to the control and measurement system. There also exists no such object as a perfect qubit since it must live in the physical world and thus have some interaction with the environment around it (such as local fluctuations in an electromagnetic field, nearby impurities, or other fluctuators which the experimentalist has tried so dashingly to minimize. These coupling provide channels of decoherence, and thus present one of the largest challenges in the construction of a many-qubit device. It is for this reason that a variety of error-protection schemes have been devised for a one-day large-scale processor [20–22] with extensions to a geometry which is readily achievable using planar superconducting qubit circuits [23], the hardware of choice for this thesis.

1.1.2 Qubit Hardware

There have been several demonstrated physical systems which have acted as qubits and which fulfill the numerous requirements for a technology to theoretically function as the same [16–18]. Here, we will provide a nonexhaustive outline of some of these systems and briefly comment on their characteristics.

Photons

It is difficult to imagine a more physically relevant system for quantum information processing than the photon, making it an attractive topic of intense research. The quantum states of a photon are encoded by several physical mechanisms including the spectrum, shape, arrival time, wave vector, and instantaneous position, all of which must be exquisitely controlled to limit the available Hilbert space to a two-level system [24–26]. One of the

primary difficulties of using photons as qubits is the reliable creation of single-photons with such well-engineered parameters [27]. This has spurred many technological advances including "ultra-bright" sources for polarized photons pairs [28, 29] and in modern times other schemes have been introduced which simultaneously use three degrees of freedom in photons to support qubit-like states, including up to 18-qubit entanglement using just six photons [30].

Neutral Atoms

There have been several qubit realizations using the natural energy level splittings within the electronic structure of atoms, with notable progress in using using some of the heavy alkalis like Rb and Cs [31–33]. Here, the two-level system of interest is defined by Nature; for identical atoms, the transitions are identical in splitting (the qubit frequency of one atom will be the same for its neighbor, and so on). This has been hailed as a great boon to neutral atom (and, similarly, trapped-ion) qubits since it significantly simplifies the manufacturing of a qubit array control system as compared to systems of synthetic atoms (read below: Quantum Dots and Josephson Circuits) regardless of the question of being able to individually address qubits without addressing their neighbors [34]. There have been demonstrations of implementing quantum gates and benchmarking them in a 7×7 2D lattice of single Cs atom qubits with high-fidelity [35, 36].

Quantum Dots

One of the signature physical objects which by itself exhibits quantum mechanical behavior is the electron; most of the complexity aside, the field of quantum dots for quantum information processing relies on using the spin of either a single electron or even a single nucleus as a qubit [37, 38]. With the size of the physical implementations being on the atomic scale, there is an enormous modern effort to build solid state qubits out of these devices with the goal being to scale them in a fashion quite similar to the transistor and

Moore's law [6] in classical computing. A great deal of progress has been made in high-fidelity gate operations in silicon based qubit systems [39–41], and there are many more architectures out there based in silicon which each has advantages and disadvantages and have been the subject of intense research in the past two decades [38].

Josephson Circuits

While the previously described implementations of qubits have relied on systems which are inherently quantum mechanical insofar as what physics must be used to fully describe their interactions, the field of Josephson quantum computing relies on micro- and nano-fabricated circuits comprising millions of superconducting atoms which together can be engineered to act as single "artificial atoms [42–45]." These, in turn, can be individually addressed and measured using relatively straightforward methods which are mostly derived from their atomic counterparts. As will be outlined in much greater detail in Sec.2.2, Josephson computing has made rapid progress in the past two decades, and there are now schemes to come up with a test that will show that near-term devices can indeed perform certain calculations which are intractable for typicall classical simulators [46]. It is within this hardware paradigm in which the work in this thesis is firmly situated.

1.2 Thesis Overview

The remainder of this thesis is organized as follows: Chapter 2 provides an outline for a choice selection of superconducting devices and their properties as they are relevant to this work. This will include introducing the Josephson junction as a powerful nonlinear inductor and how it fits into the scope of both quantum and classical logic superconducting computing devices. Then, in Chapter 3, we will introduce circuit quantum electrodynamics (cQED), a powerful toolbox used to design, measure, and analyze superconducting quantum circuits. One necessary element of an effective measurement chain when it comes to

superconducting qubits is the (at least near-) quantum-limited amplifier. One such flavor of this amplifier is the superconducting low-inductance undulatory galvanometer (SLUG) amplifier, and some of its useful properties as an amplifier in the context of qubit measurement will be described therein as well. Later, in Chapter 4, a hybrid device will be introduced in which a superconducting qubit is cofabricated on the same chip as a superconducting logic circuit for the purposes of coherent quantum control. The considerations and challenges related to such an integration are discussed and ultimately the performance of the control circuit is fully characterized. Finally, in Chapter 5, we conclude by summarizing this thesis and providing a brief outlook of some reasonable next steps for the integration of quantum and classical superconducting devices.

2 SUPERCONDUCTIVE DEVICES

Following the discovery of superconductivity of Hg in liquid helium (LHe) by Onnes in 1911 [47, 48] and the successful theoretical treatment of microscopic superconductivity by Bardeen, Cooper, and Schrieffer (BCS) in 1957 [49], a great wealth of research has been done insofar as what sorts of devices can be constructed which take advantage of the superconductive phenomenon. In this Chapter, we present a rather non-exhaustive overview of select low-temperature superconducting devices as well as their physical properties as they are relevant to this work. Here, we will not go into great detail on the nuances of neither superconductivity nor the effect of magnetic fields on superconductors or superconductive devices in favor of highlighting the ideas and facets of the technologies as they are contextually relevant for this work. Assuming the reader's interest, the author suggests Tinkham's introductory text on superconductivity [50] for the uninitiated with follow-up texts specializing on the Josephson effect by Barone [51] and Likharev [52] for the advanced reader.

This Chapter is divided as follows: Section 2.1 introduces the workhorse device of most superconducting devices, the Josephson junction (JJ). Then, in Section 2.2, we give an overview of quantum devices based on superconducting devices, and, most notably, JJs. In Section 2.3, we provide a brief overview of the state of modern superconducting electronics. Finally, in Section 2.4, we summarize this Chapter and help place it firmly in the context of superconducting quantum information processing.

2.1 Josephson Junctions

The workhorse device in the modern-day field of superconducting devices is without doubt the JJ [54, 55] – a device composed of two superconducting wires interrupted by a weak link. If the mitochondrion is the "Powerhouse of the [living] cell" [56], then the JJ is the "Powerhouse of superconductive devices." Whether one is interested in the construction

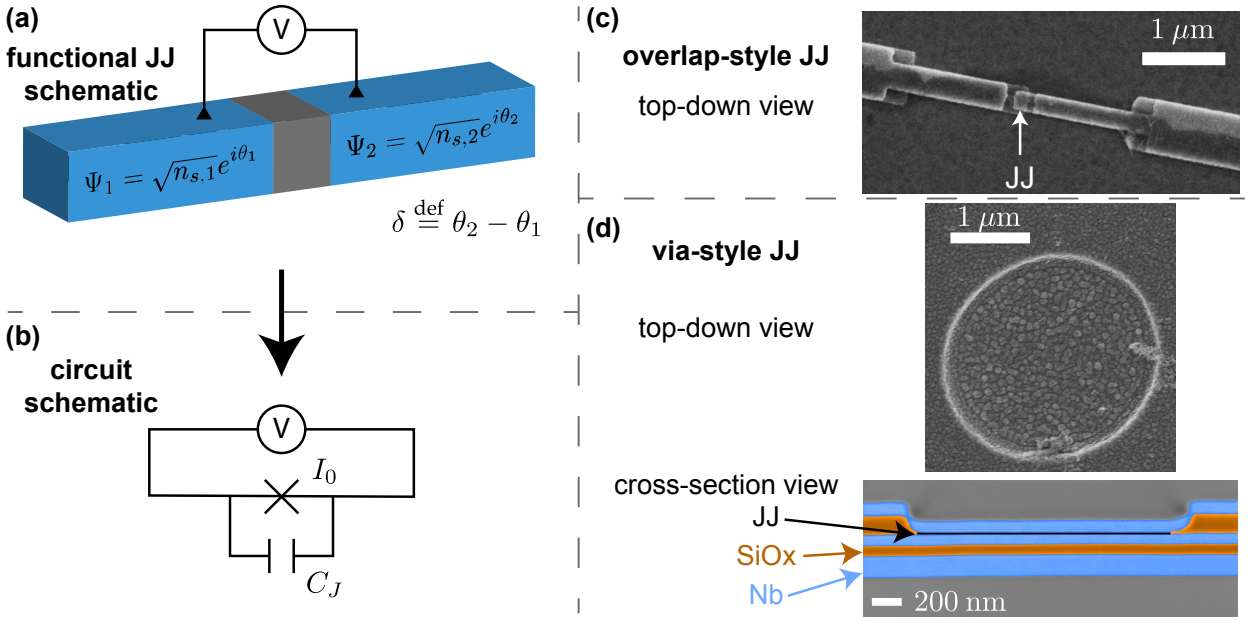

Figure 2.1: **(a)** JJ block diagram of two superconductors (blue), each with respective superconducting wavefunction Ψ_i and phase θ_i, interrupted by a weak link (grey). The phase difference between the two superconductors across the weak link is defined as $\delta \equiv \theta_2 - \theta_1$. **(b)** Circuit representation of the above JJ with critical current I_0 and self-capacitance C_J (an obvious addition given the geometry above). **(c)** SEM image of an overlap-style Al/AlOx/Al JJ fabricated using a standard Dolan bridge process [53] in an electron-beam lithography tool followed by double-angle evaporation of Al electrodes. This technology is useful for achieving low critical current densities ($J_c \approx 10$ A/cm^2) appropriate for modern qubit devices. **(d)** SEM image of a via-style JJ fabricated by interleaving two superconducting Nb layers with a thin AlOx barrier. (top) Top-down view of the device. (bottom)Cross-section showing the layer stack. Here, blue is Nb, orange is SiOx, and the thin black line between the two upper Nb layers is a ~nm-thick AlOx barrier. This technology is useful for achieving high J_c ($\gtrsim 10$ kA/cm^2), which is typical in modern SCE circuitry.

of quantum or classical superconducting circuitry, the JJ is ubiquitous due to its wide variety of use cases and constructions. In this Section, we will provide a brief outline of the dynamics of a single JJ in a few situations to serve as groundwork for the following Sections of this Chapter.

2.1.1 Josephson Relations

JJs are constructed by interleaving two superconducting materials with a weak link. The materials used for the superconductors and weak links largely have an impact on the fabrication needs of a specific technology while not having a significant impact on the mathematical treatment of the JJ. Josephson's theoretical work showed two specific relations for these devices: that the current through such a device and the voltage across it could be described by

$$I(\delta) = I_c \sin(\delta) \tag{2.1}$$

$$V(\delta) = \frac{\Phi_0}{2\pi}\frac{d\delta}{dt}, \tag{2.2}$$

respectively, where δ is the phase difference of the superconducting wavefunction on either side of the JJ [shown diagramatically in Fig. 2.1(a)] and $\Phi_0 \equiv \hbar/2e$ is the magnetic flux quantum. The Josephson effect was first experimentally verified by Anderson [57] after which a number of different constructions including those using an insulator between the two superconductors (so-called Superconductor-Insulator-Superconductor, or SIS), a normal metal (SNS), or simply a narrow constriction of the superconducting material (SsS) – all of which obey the above relations irrespective of which construction is employed. Differentiating Eq. (2.1) and substituting Eq. (2.2) for $d\delta/dt$, one finds

$$V(\delta) = \frac{\Phi_0}{2\pi I_0 \cos\delta}\frac{dI}{dt}, \tag{2.3}$$

or a voltage drop with a linear dependence on dI/dt, implying that the pre-factor here is an inductance

$$L_J(\delta) = \frac{\Phi_0}{2\pi I_0 \cos\delta} \equiv \frac{L_{J0}}{\cos\delta}, \tag{2.4}$$

the so-called Josephson inductance. This makes the JJ a dissipation-free nonlinear inductor, which are the key aspects of the device in its use in superconducting qubits as well as in large-scale SCE components.

2.1.2 Josephson Energy

Since the JJ can be described as an inductor, it is then straightforward to imagine that the JJ is capable of storing energy. This energy is found by integrating the product of Eqs. (2.1,2.2):

$$\begin{aligned} U_J &= \int I(\delta)\, V(\delta)\, dt \\ &= \frac{I_0 \Phi_0}{2\pi} \int \sin(\delta)\, \frac{d\delta}{dt} dt \\ &= -\frac{I_0 \Phi_0}{2\pi} \cos\delta \equiv -E_J \cos\delta, \end{aligned} \tag{2.5}$$

where E_J is defined as the Josephson energy and the integration constant has been ignored since it will only contribute to a global offset and not the dynamics of the circuit. Coupling Eq. (2.5) with Fig. 2.1(b), we can now write an effective Hamiltonian for a single JJ as

$$\mathcal{H}_J = E_C + U_J, \tag{2.6}$$

where E_C is the charging energy of the capacitor shunting the JJ. Substituting in the circuit quantities, the Hamiltonian becomes

$$\hat{\mathcal{H}}_J = \frac{\hat{Q}^2}{2C_J} - E_J \cos\hat{\delta} = 4E_C \hat{n}^2 - E_J \cos\hat{\delta}, \tag{2.7}$$

where the charge Q on the capacitor C_J and the phase difference δ across the JJ have both been promoted to quantum mechanical operators, $\hat{n} = \hat{Q}/2e$ is the operator for the number of Cooper-pairs on the positive side of the JJ, and $E_C = e^2/2C_J$ is the charging energy of

C_J. Here, $\hat{n}$ and $\hat{\delta}$ obey the canonical commutation relation

$$\left[\hat{\delta}, \hat{n}\right] = i, \tag{2.8}$$

Now, a slightly more interesting circuit is the current-biased JJ as shown in Fig. 2.2(a). This modifies the JJ potential energy to the form

$$U_J = \int I(\delta)\, V(\delta)\, dt = -E_J \left(\cos\delta + \delta I_b/I_0\right), \tag{2.9}$$

where I_b is the JJ bias current. This potential energy provides one of the most clear methods through which the dynamics of a JJ can be understood. In Fig. 2.2(a), we plot Eq. (2.9), known as the "tilted washboard potential," for three different values of $i \equiv I_b/I_0$ and we superpose a so-called "phase particle" (black circle) atop two of the lines ($i = \{0.5, 1\}$) to illustrate potential dynamics of δ. Using this illustration, it is plain to see that for a sufficiently small kinetic energy of the phase particle, it can become trapped in a well of $U(\delta)$ and simply slosh back and forth. However, once $I_b \geqslant I_0$, the wells of the potential no longer have a local minima into which the phase particle may settle, and instead it will continue to free-evolve[1].

2.1.3 Over- vs. Under-damped JJs (The RCSJ Model)

A shunt resistor in parallel with a JJ [depicted in Fig. 2.2(b)] will induce different JJ dynamics with regard to the aforementioned phase particle on a tilted washboard; these dynamics are well described by the **R**esistor and **C**apacitor **S**hunted **J**unction (RCSJ) model [59, 60].

[1] The author suggests [58] for more perspective on this analogy.

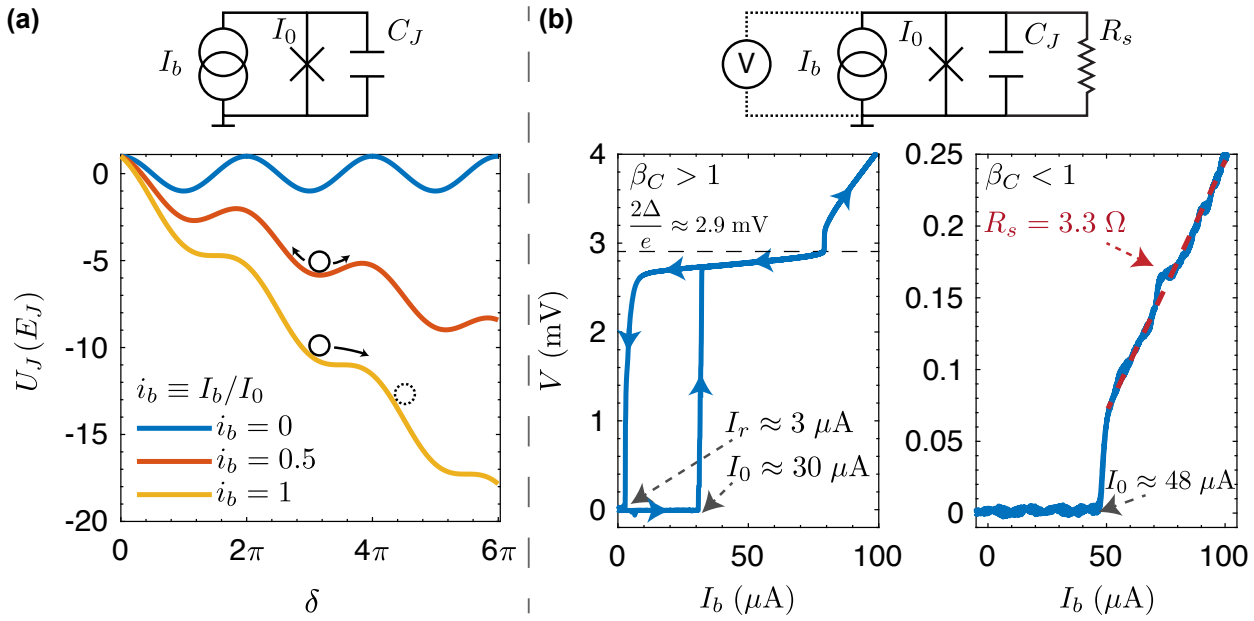

Figure 2.2: **(a)** (circuit) Simple current-biased JJ with the JJ self-capacitance for completeness. (plot) The potential energy U_J of the JJ for different bias currents as prescribed by Eq. (2.9). Here, the fictitious phase particle is drawn in black rolling along the $i_b = \{0.5, 1\}$ curves; using this analogy, it is simple to see that there are local minima in which the phase particle can become trapped so long as $i_b < 1$ with the alternate being a phase particle in free fall, resulting in a continuous evolution of δ. **(b)** (circuit) A resistively and capacitively shunted JJ (RCSJ) including a voltmeter V to monitor the response of the circuit to changing bias I_b. (left plot) Sample IV curve from an unshunted JJ ($R_s \to \infty$). Here, the critical current is $I_0 \sim 30\ \mu$A, retrapping current $I_r \sim 3\mu$A and the superconducting gap of the JJ is $2\Delta \sim 2.9$ meV, $\sim 3\%$ lower than bulk Nb. (right plot) Over-damped JJ shunted by a resistance $R_s = 3.3\ \Omega$ with critical current $I_0 \approx 48\ \mu$A. Here, we see the voltage response is single-valued for all current bias space.

Current conservation for such a circuit gives

$$I_b = I_J + I_C + I_R \tag{2.10}$$

$$= I_0 \sin\delta + C_J \frac{dV}{dt} + \frac{V}{R_s}, \tag{2.11}$$

where R_s is the shunt resistance and V is the voltage across the JJ. Here, we are ignoring the non-zero thermal noise provided by R at finite temperature. Using Eq. (2.2), dimensionless

time $\tau = 2\pi I_0 R_s t/\Phi_0$, and dimensionless current $i = I/I_0$, one re-writes this as

$$\beta_C \ddot{\delta} = i_b - \sin\delta - \dot{\delta}, \tag{2.12}$$

where $\beta_C = 2\pi I_0 C_J R_s^2/\Phi_0$ is known as the Stewart-McCumber damping parameter [59, 60] and governs the latching dynamics of the circuit. Perhaps more naturally, it is written as a ratio of the RC time constant to the competing L/R time constant provided by the Josephson inductance Eq. (2.4)

$$\beta_C \overset{\text{def}}{=} \frac{\tau_{RC}}{\tau_J} = \frac{R_s C_J}{L_{J0}/R_s} = \frac{R_s C}{(\Phi_0/2\pi I_0)/R_s} = \frac{2\pi}{\Phi_0} I_0 C_J R_s^2. \tag{2.13}$$

This provides an avenue for a qualitative understanding of β_C: if $\beta_C \geqslant 1$, then the characteristic trapping time of the $R_s C_J$ tank circuit is slower than that of the competing L_J/R_s time – this implies that the RL oscillator dynamics will dominate, and since the L is representative of the JJ, this will cause the phase particle in Fig. 2.2(a) to evolve unchecked for sufficiently steep slopes even if $I_b/I_0 < 1$. This is called the "latched" state, in which a single 2π evolution of δ will result in many more 2π oscillations until the slope of the tilt is significantly reduced; this will "retrap" the phase particle into one of the potential wells. Conversely, if $\beta_C < 1$, the $R_s C_J$ circuit clocks in faster than the inductive JJ, dominating the dynamics when $I_b < I_0$. Here, it is possible to induce a single 2π phase evolution of our fictitious particle in Fig. 2.2(a) by dynamically modulating I_b to (or slightly above) I_0 for a very brief amount of time after which the JJ returns to the supercurrent state.

An experiment one may perform to ascertain whether or not a JJ is over- or underdamped is described as follows [using the circuit in Fig. 2.2(b)]:

1. Connect a JJ with parallel resistor to a variable current source I_b and monitor the voltage V across the JJ

2. Sweep I_b up from zero while monitoring the voltage across the JJ until a large step

appears at I_0 followed by a resistive segment

3. Sweep I_b back down to zero, and plot the two directions together; a JJ with single-valued (multi-valued) voltage responses for similar values of I_b is over-damped with $\beta_C < 1$ (under-damped with $\beta_C \geqslant 1$). In the multi-valued case, the current at which the voltage drops back down to zero is called the retrapping current I_r.

Sample data from such an experiment for both the over- and under-damped case is shown in Fig. 2.2(b).

2.1.4 Superconducting QUantum Interference Devices (SQUIDs)

Up to this point, a rather glaring omission has been made in the discussion of JJs: the effect of a magnetic field on a JJ circuit. A hallmark device one is able to construct using JJs is a superconducting quantum interference device (SQUID). There are two flavors of SQUID: the rf SQUID comprising a single JJ interrupting an inductor loop and the dc SQUID comprising an inductor loop which is interrupted by two JJs in parallel. Replacing the single JJ of Fig. 2.2(a) with two JJs in parallel, each with critical current $I_0/2$, does nothing to change the expected dynamics of the circuit. However, in the presence of an external magnetic flux Φ_e, or if the two JJ critical currents are non-equal, special considerations must be made. The current through the two JJ loop would then be written (ignoring the JJ capacitance)

$$I_b = \sum_n I_{0,n} \sin \delta_n = I_{0,1} \sin \delta_1 + I_{0,2} \sin \delta_2, \tag{2.14}$$

where the continuity of the superconducting wavefunction in the loop stipulates that the two JJ phases are related by

$$\delta_2 - \delta_1 = 2\pi \frac{\Phi}{\Phi_0} \tag{2.15}$$

where Φ is the total flux through the loop comprising the two parallel JJs and can be written as $\Phi = \Phi_e + LI_l$ in which $I_l = (I_2 - I_1)/2$ is the circulating current in the JJ loop of inductance L. Using this, and assuming $I_{0,1} = I_{0,2} \equiv I_0$, the dc SQUID overall critical current is modulated by

$$I_c(\Phi_e) = 2I_0 \cos\left(\frac{\pi\Phi_e}{\Phi_0}\right), \tag{2.16}$$

implying immediately that the dc SQUID is useful as a magnetometer with exceedingly high sensitivity [50, 51].

dc SQUID Hamiltonian

The Hamiltonian of a dc SQUID comprising two JJs, when considering only the Josephson energies, can be written as

$$\begin{aligned} H_J &= U_{J1} + U_{J2} \\ &= -E_{J1}\cos\delta_1 - E_{J2}\cos\delta_2, \end{aligned} \tag{2.17}$$

where δ_1, δ_2 are constrained by Eq. (2.15). Defining an effective phase $\delta = (\delta_1 + \delta_2)/2$ and Josephson energy $E_{J\Sigma} = E_{J1} + E_{J2}$, the Hamiltonian becomes

$$\hat{\mathcal{H}}_J = -E_{J\Sigma}\cos\left(\frac{\pi\Phi}{\Phi_0}\right)\sqrt{1 + d^2\tan^2\left(\frac{\pi\Phi}{\Phi_0}\right)}\cos\left(\hat{\delta} - \delta_0\right), \tag{2.18}$$

where $d \equiv (I_2 - I_1)/(I_2 + I_1)$ is a term representing the asymmetry of the two JJs in the loop and $\tan\delta_0 = d\tan(\pi\Phi/\Phi_0)$ is a term which can be discarded by a variable change for a constant flux Φ. This means that the results of the above section concerning single JJ circuits can still be applied to an asymmetric dc SQUID circuit so long as the flux is

constant by replacing the JJ energy with [61]

$$E_J \rightarrow E_{J\Sigma} \cos\left(\frac{\pi\Phi}{\Phi_0}\right)\sqrt{1 + d^2 \tan^2\left(\frac{\pi\Phi}{\Phi_0}\right)}. \tag{2.19}$$

This expression is useful when considering the energy levels of superconducting qubits which employ a dc SQUID (e.g. the split transmon, which is the style of device employed for the work covered in Chapter 4).

2.2 Superconducting Qubits

Given that a JJ is a dissipationless nonlinear circuit element, it follows that a variety of interesting devices which may be treated quantum mechanically can be constructed using it along with other dissipationless items such as inductors and capacitors. One of the most important requirements for a qubit is that the transition between the two states being used as the computational manifold is able to be addressable without exciting the system to an undesired level (this is alluded to in Sec. 1.1.1). It is for this reason that a quantum harmonic oscillator (QHO) is a poor choice as the level spacings between transitions are all degenerate in energy. However, if one is able to introduce a nonlinearity into the potential, the oscillator may become anharmonic (i.e., $E_{21} \neq E_{10}$), implying that the ground and first excited state of the oscillator may be treated to first order as a two-level system; it is convenient in many ways to use a JJ as this nonlinearity in superconducting quantum circuits. What follows in this Section is a brief overview of some traditional superconducting qubit circuits based on JJs and some of their respective properties, advantages, and shortfalls, with special care taken in Sec. 2.2.4 in discussing the transmon since it was the flavor of qubit used for the work in this thesis. While enough detail for the other flavors of qubits will be shown to provide context for this work, the advanced reader will be interested in reading some of the wealth of literature resulting from the last 20 years of research of these devices and their properties, which has been reviewed from time to time since the early 2000's [42–45, 62–64].

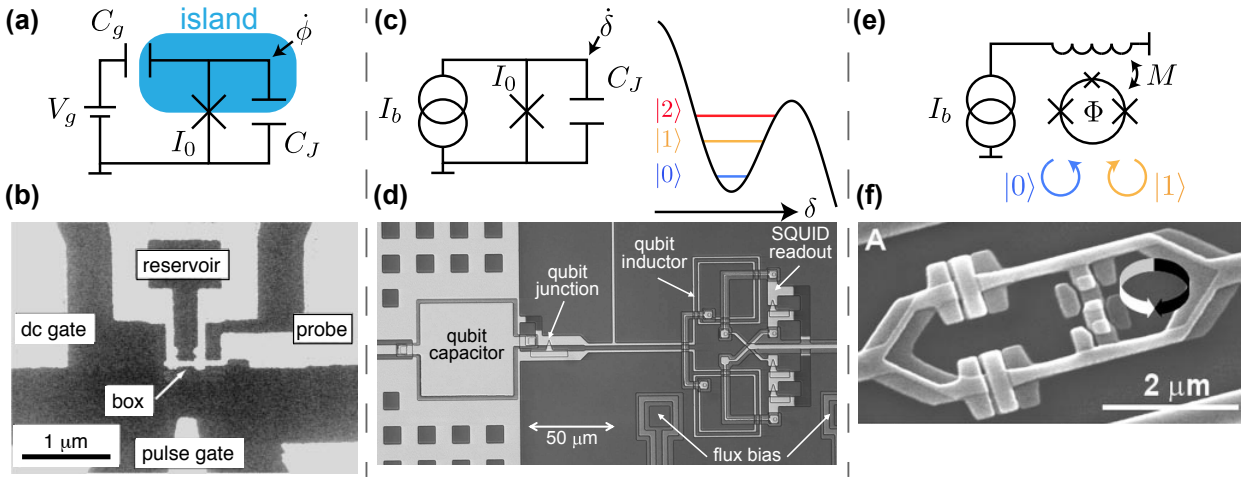

Figure 2.3: **(a)** Circuit for a basic CPB with single bias voltage V_g. The "box" – or island – is highlighted in blue. The voltage across the JJ is written as $V = 2\pi\dot{\delta}/\Phi_0 \equiv \dot{\phi}$. **(b)** Micrograph of the first CPB which was coherently manipulated by electrical signals. Here, the CPB island is connected to a reservoir by two JJs in parallel and is capacitively control by both a dc gate (V_g) and a rf pulse gate for coherent control. The state of the CPB is measured using a probe JJ. Image direct from [65]. **(c)** Simplified circuit diagram for a simple current-biased phase qubit. The potential energy landscape for this circuit is described by Eq. (2.9) and shown in Fig. 2.2(a). **(d)** Micrograph of a relatively modern phase qubit device with various additional circuit elements labeled. Here, the phase qubit is shunted by an explicit capacitor and measured via SQUID readout. Image direct from [66]. **(e)** Circuit diagram for a simple flux qubit wherein a three JJ SQUID is biased by $\Phi_b = MI_b$. **(f)** SEM micrograph of the first flux qubit in which coherent operations were performed and measured. The qubit circuit comprises the loop on right right while the loop on the left constitutes the measurement circuit for this particular device. Image direct from [67].

Here, we will readily make use of circuit quantum electrodynamics nomenclature, a brief introduction to which is presented later, in Section 3.1.

2.2.1 Cooper-pair box

The Cooper-pair box (CPB) [68] (also known as a charge qubit) was the first solid-state device in which a macroscopic quantum state was coherently manipulated using electrical signals[2] [65]. In this style of qubit, the "macroscopic" degree of freedom which is to

[2]In the year prior to Nakamura's 1999 work in coherently manipulating the state of a CPB [65], another successful effort resulted in the coherent manipulation of a solid-state quantum dot device using optical excitations instead of electrical signals [69].

be coherently manipulated is the number of excess Cooper-pairs n which reside on a superconducting metal island which is connected to a Cooper-pair bath via a JJ [depicted in Fig. 2.3(a)]. The charging energy of the island is similar to before

$$E_C = \frac{e^2}{2C_\Sigma} \tag{2.20}$$

except now the total island capacitance includes both the gate capacitor C_g as well as the JJ self-capacitance C_J as $C_\Sigma = C_g + C_J$. The JJ energy remains unchanged, but there is now an additional term to the kinetic and potential energy due to C_g, making the Hamiltonian

$$\mathcal{H}_{CPB} = Q\dot{\phi} - (T - U) = Q\dot{\phi} - \left[\underbrace{\frac{C_g\dot{\phi}^2}{2} + \frac{C_J\dot{\phi}^2}{2}}_{\text{kinetic}} - \underbrace{\left[-E_J \cos\frac{2\pi\phi}{\Phi_0} + V_g Q_g \right]}_{\text{potential}} \right]. \tag{2.21}$$

Using the conjugate momentum $Q = \partial\mathcal{L}/\partial\dot{\phi}$, the total capacitance $C_\Sigma = C_g + C_J$, defining the charge $Q_g = (-\dot{\phi})V_g C_g$, and elevating Q and δ to operators, this is written in a simple form

$$\hat{\mathcal{H}}_{CPB} = \frac{\left(\hat{Q} - C_g V_g\right)^2}{2C_\Sigma} + E_J \cos\hat{\delta}. \tag{2.22}$$

Through a change of basis, this can be written in a more convenient form. The ingredients needed are: define a number operator $\hat{n} = \hat{Q}/2e$ representing the number of Cooper-pairs on the island, $n_g = C_g V_g/2e$ for the bias circuit, and also that the $\cos\hat{\delta}$ term for the JJ coupling energy can be re-written using the relationship $e^{\pm i\hat{\delta}}|n\rangle = |n \pm 1\rangle$. We can now re-write Eq. (2.22) in matrix form as [68]

$$\hat{\mathcal{H}}_{CPB} = \sum_n \left[4E_C \left(n - n_g\right)^2 |n\rangle\langle n| - \frac{E_J}{2}\left(|n+1\rangle\langle n| + |n-1\rangle\langle n|\right) \right]. \tag{2.23}$$

For typical qubits of this style, it is generally a goal to make devices satisfying $E_C \gg E_J$ such that the system is very sensitive to small differences in $\hat{n}$. However, while this was required such that the system could be controlled, it made the device impractical for large-scale systems due to both charge noise and quasiparticle (unbound electrons/holes in the superconductor) tunneling to/from the island causing system instabilities and fast decoherence. As far as the author is aware, no major efforts at present are attempting to further advance CPB technology.

2.2.2 Phase qubit

One design that was hailed for its simplicity in the early days of superconducting qubits was the current-biased phase qubit, which saw its first coherent oscillations in devices tested in the early 2000s [70, 71]. This device has been already described in Sec. 2.1.2 wherein it is shown that the Hamiltonian of the circuit can be written such that the potential energy of the circuit includes wells which tilt according to a dc bias current, allowing the states of the wells to be tuned into operable regimes. The energy structure in the wells is not purely quadratic, giving rise to an anharmonic structure [i.e., $E_{21} \neq E_{10}$; depicted in Fig. 2.2(c)] between energy levels which is tunable via adjusting I_b.

In the early tests, qubit frequencies tested were around 2-7 GHz [58, 71] with coherence times in the 20 ns range [71]. In the years that followed, it was shown the the most major sources of decoherence in these devices was due to the use of lossy dielectrics – initial devices used SiN_x while state-of-the-art used hydrogenated amorphous silicon (a-Si:H) – as well as two-level fluctuators which naturally existed in the AlO_x barrier of the JJs used in these devices – the overall size of the JJ was reduced here to in turn reduce the number of these fluctuators and the qubit frequency was then tuned away from the remaining fluctuators to obtain optimal performance. However, even with all of these updates to design and fabrication considerations, the state-of-the-art phase qubit coherence times remained $\sim$ 1 μs [66], making future technologies with longer coherence times more

attractive from a computational depth potential point of view.

2.2.3 Flux qubit

The persistent-current flux qubit was first examined in the late 1990s [72, 73] with superpostiion observations [74] and coherent operations [67] first taking place in devices tested in the early 2000s. Here, circuits are designed such that the quantum variable of interest is the direction of flux (current) through (around) a three-JJ SQUID loop[3], a sample schematic of which is drawn in Fig. 2.3(e).

One of the biggest drawbacks of the traditional flux qubit is its sensitivity noise in this channel of control, and in particular the ubiquitous $1/f$ flux noise which has been observed in superconducting devices without full explanation since the 1980s[4] [76, 77]. However, in recent years progress has been realized in using a capacitively-shunted flux qubit [78] with a modern fabrication process (reducing additional lossy dielectrics and using high quality materials) resulting in coherence times around 50 μs. While this is a major improvement from early devices, these qubits are still dominated by flux noise as a source of decoherence [78].

2.2.4 Transmon

The transmon qubit, or the *transmission-line shunted plasma oscillation qubit*, is in principle designed to function similarly to the previously described CPB, but with exponentially lower sensitivity to charge noise on the drive line and is also designed to be embedded into a microwave environment (planar or 3D) which is engineered such that noise at the qubit transition frequency ω_{10} is suppressed [61]. Both of these effects, coupled with other advances in materials research and fabrication advances, have had a dramatic effect on

[3] One of the reasons that three JJs are in use here instead of one is to add more inductance to the loop while also keeping the loop size small [64].

[4] It is worth note here that recent work has shown a potential explanation of this noise in surface adsorbed O_2 onto the superconducting circuits under test [75].

qubit coherence in the transmon regime where the relationship between E_J and E_C is typically $E_J/E_C \sim 50$, meaning that the JJ coupling energy dominates the dynamics of the system (and thus $\hat{\delta}$ is a good quantum variable while $\hat{n}$ has minimal effect). One can take the Hamiltonian from Eq. (2.7) and assume small δ to expand the cosine term to fourth order

$$\hat{\mathcal{H}} = 4E_C\hat{n}^2 - E_J\cos\hat{\delta} \approx \underbrace{4E_C\hat{n}^2 + \frac{E_J}{2}\hat{\delta}^2}_{\text{HO}} - \frac{E_J}{4!}\hat{\delta}^4, \tag{2.24}$$

where the harmonic oscillator (HO) term is perturbed by the quartic term of the cosine expansion. Using perturbation theory, one extracts energy transition frequencies

$$E_{m+1} - E_m = \hbar\omega_{m+1,m} \simeq \sqrt{8E_JE_C} - E_C(m+1), \tag{2.25}$$

giving the lowest two energy splittings as

$$\hbar\omega_{10} \simeq \sqrt{8E_JE_C} - E_C, \tag{2.26}$$

$$\hbar\omega_{21} \simeq \sqrt{8E_JE_C} - 2E_C, \tag{2.27}$$

showing that the anharmonicity of these two transitions is

$$\alpha = \omega_{21} - \omega_{10} \simeq -E_C/\hbar, \tag{2.28}$$

making it a parameter which is tunable by changing the geometric capacitance shunting the JJ in this circuit [61]. Typical device parameters for modern transmon qubits include fundamental transition frequencies near $\omega_{10} \sim 5$ GHz, anharmonicities around $\alpha/2\pi \sim 200-400$ MHz, and exhibit coherence times approaching 100 μs[5] enabling the construction

[5] As is outlined in much of the cited material on this topic, a cause for the explosion in coherence is the use of fabrication processes with careful attention to the use of lossy dielectrics; they are either minimized or completely absent in modern devices. A sample processing flow will be described in detail in Chapter 4.

and operation of modestly complex circuits [44, 45, 64].

2.3 Superconducting Electronics

The field of superconducting classical electronics (SCE) relies heavily on JJs as their primary active element[6]. SCE as a field of study has a long history dating back to the late 1960s with the first demonstration of a flip-flop circuit employing a JJ [80] inspiring visions and devices for potential large-scale integration (LSI) showing up as early as 1980 [81]. An explosion of activity kicked off in the early 1990s after the seminal work describing a technology family which addressed the shortcomings of prior SCE devices and increased clock speeds to the order of 100 GHz using relatively simple building blocks [82–84]. Since then, the field has spawned new technologies for superconducting logic circuits, all of which rely on JJs as their primary building blocks.

In this Section, we aim to provide a topical introduction to SCE devices based on JJs without diving into all possible details. While in Section 2.1, we primarily treated the JJ for its quantum mechanical properties, we will now utilize the JJ in circuits which are ultimately treated as classical logic gates. Here, we will provide detail where it is relevant for the context of this thesis and more broadly overview the more advanced topics of SCE to whet the reader's appetite for further delving into this massively-researched field.

2.3.1 Superconducting Flux Quanta as Classical Bits

The basic act of data transfer in typical superconducting logic circuits is accomplished via the shuttling around of flux pulses which propagate in time from point to point while

However, it is worth noting that even with modern fabrication processes, qubit-environment coupling remains a dynamic issue which requires careful attention and calibration in larger-scale systems [79].

[6]The transistor is to CMOS as the JJ is to SCE.

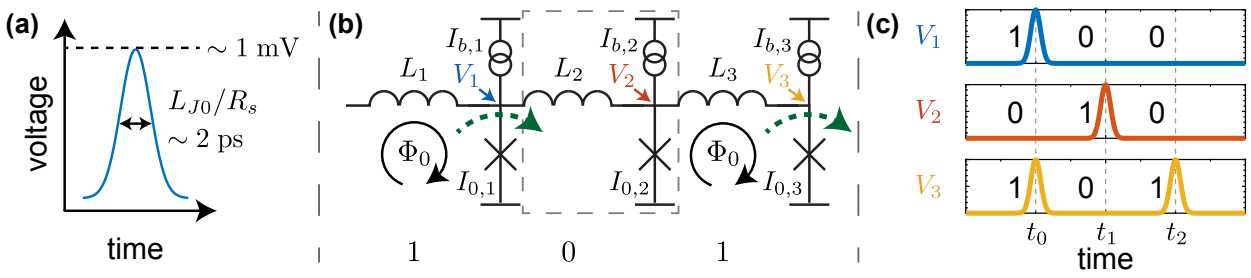

Figure 2.4: **(a)** Depiction of a typical SFQ flux pulse wherein the area under the curve is quantized to $\Phi_0 = 2.068$ mV $\times$ ps $= 2.068$ mA $\times$ pH. The width of this pulse is given by the L/R time constant of the JJ/resistor circuit which for typical parameters is on the order of ~ 1 ps. **(b)** Sample Josephson transmission line (JTL) circuit at a point in time wherein the first and third JTL cell contain a flux quantum, making the "binary" representation of this circuit "101." Each clock cycle of this circuit (the action during the next cycle is drawn with a green dashed-line) will cause the binary code to advance one cell to the right; assuming no incident pulse from the lab, the new binary code will be "010." (dashed-line box) The ith JTL unit cell, each of which comprises an overdamped JJ (shunt elements not drawn) with critical current $I_{0,i}$, inductor L_i, and bias source $I_{b,i}$. Here, $I_{b,i} \approx 0.7 I_{0,i}$ and $L_i I_{0,i} \sim \Phi_0/2$ (see main text). **(c)** Voltage traces for the V_i nodes identified in the previous panel. The circuit is temporally binned with t_0 representing the initial state of the circuit; the trace in each time bin represents the classical state of the circuit during that clock cycle, where the clock frequency here is $\omega_{clk} = 2\pi/(t_{n+1} - t_n)$.

maintaining a time integral governed by the second Josephson relation Eq. (2.2)

$$\int_{\substack{\text{one}\\\text{pulse}}} V(t)\,dt = \frac{\Phi_0}{2\pi}\int_{\delta_0}^{\delta_0+2\pi}\frac{d\delta}{dt}dt = \Phi_0 = 2.068\ \text{mV}\times\text{ps} = 2.068\ \text{mA}\times\text{pH}, \tag{2.29}$$

the superconducting flux quantum (SFQ). A sample curve of such a pulse is drawn in Fig 2.4(a). Shuttling bits from one part of a circuit to another in so-called rapid SFQ (RSFQ) circuits is typically done either with superconducting passive transmission line (PTL) – typically a microstrip geometry [85, 86] – or with a Josephson transmission line (JTL) comprising serial inductors and parallel JJs through which SFQ pulses propagate [depicted in Figs. 2.4(b),2.4(c)]. Typical parameters of the JTL include biasing individual JJs near their critical current $I_{b,i} \simeq 0.7 I_{0,i}$ and constraining the cell inductance by $L_i I_{0,i} \simeq \Phi_0/2$ [83, 84].

Using these inductor/JJ combinations as building blocks, one can establish a complete classical logic gate set – following deMorgan's theorem – by showing that both NOT and

either AND or OR operations can be defined. This was first shown in RSFQ circuits in the early 1990s [87, 88], paving the way for the multitude of circuit design and research that has taken place since.

2.3.2 Modern SCE

Since the early 1990s with the advent of RSFQ technology [84] which relied heavily on resistor networks for distributed bias currents throughout the circuit chip, other technologies have been devised with different advantages and drawbacks. Here, we will briefly outline a select few of them and provide an overview as to the differences between the variants. For the advanced reader, the author recommends a more detailed overview of these technologies plus others that will not be covered here [89].

Energy-efficient RSFQ

The primary difference between traditional RSFQ and ERSFQ is the bias network. Whereas in traditional RSFQ resistor networks are used to distribute bias current, in ERSFQ variants these networks are replaced by combinations of JJs and inductors. This leads to a background power dissipation which is substantially lower than RSFQ [90]. Due to all of the extra JJ dynamics in the circuit from the bias JJ network, special care must be taken when evolving the phase of the logic elements since there is now phase dynamics in the bias to account for which was not present when using simple resistors [89]. For the most part, however, the circuit is operated in a very similar fashion to RSFQ circuit counterparts with the difference that there are approximately $30 - 40\%$ more JJs required for proper operation [91]. Some of the earlier devices tested using this new scheme were shown to correctly operate up to 67 GHz.

Reciprocal Quantum Logic

A variant of superconducting logic circuit which replaces dc bias sources with an ac bias (similar to the quantum flux parametron technology [92–95]that also acts as the circuit clock is the reciprocal quantum logic (RQL) circuit family [96]. Here, devices are comprised of JJ/inductor networks for both biasing and operation and data bits are transmitted as fluxon-antifluxon pairs (i.e., instead of a single positive fluxon constituting a logical 1 as in Fig. 2.4(a), here a logical 1 is a positive-negative pulse pair). Tested circuits are shown to operate correctly and with very low bit-error-rates up to 12 GHz.

2.4 Summary

In this Chapter, we have briefly described several technologies which are powered by JJs in various configurations. Ever since Josephson's prediction about JJ dynamics in 1962, a vast wealth of research has been done in using these non-dissipative, non-linear devices in a variety of superconducting circuits. In the late 1980s, a major leap forward was made with the invention of RSFQ circuits which are able to compute and transmit data at speeds which are at least a factor of 20 faster than typical modern computer processors today. We briefly described this technology and provided several avenues of further reading for the interested reader.

Along with the classical logic circuitry enabled by JJs, over the past 20 years, the field of superconducting quantum information processing (sQIP) has benefited greatly from the careful use of JJs as nonlinear inductors in slightly anharmonic oscillator potentials wherein the bottom two energy levels serve as a quantum computational manifold. Here, JJs are embedded in circuits which are carefully engineered to protect the coherence of the quantum state, taking into the consideration not only the coupling to the outside world but also the materials and fabrication required to create such devices. We have laid out a short introduction to some styles of superconducting qubits that have been studied and

described some of their properties.

These two technologies – superconducting classical and quantum circuits – each are topics of intense research today, and this thesis represents one work which requires the use of both. While in this Chapter we have introduced basic elements of the two in a separate fashion, Chapter 4 will be an overview of a successful combination of the two technologies into one operable device in which the classical SFQ circuit is used as a controller for the quantum transmon qubit. This work represents a major step towards the tight integration of the two technologies, the potential benefits of which are outlined with the presented results.

3 CQED & JOSEPHSON AMPLIFIERS

The toolbox known as circuit quantum electrodynamics (cQED; based on much of the same ideas and reasonings as cavity QED; see, e.g., [97, 98]) has been reported on many times since its inception in the mid-2000s including rigorous theoretical and numerical studies [61, 99] as well as several advances on the practical design, fabrication, and measurement of quantum circuits [100–102]. There have also been some very practical and encyclopedic summaries overviewing the quantum nature of electrical circuits [103] as well as cQED from a first-principles point of view [104]. That being said, while the primary works in this thesis rely on the past progress of previous and current practitioners of cQED, the author does not make any claim to have furthered cQED itself.

In this Chapter, we will briefly outline cQED as it is relevant for the context of this thesis. In Section 3.1, a brief overview of the tools born out of cQED as they are useful for full understanding of this work is provided, most notably including details about the control and measurement of quantum states of transmon qubits (see Sec. 2.2.4) in the cQED framework [61]. Then, in Section 3.2, we will briefly outline the need for high-gain, low noise amplifiers when considering the measurement aspect of a practical qubit system. This will include a brief overview of both the historical and modern landscape of near-quantum-limited amplifiers used to perform qubit state measurement in superconducting qubit architectures, and in particular will focus on the superconducting low-inductance undulatory galvanometer (SLUG) amplifier; a detailed SLUG device description will be provided as well as details about modeling, fabrication, and circuit characterization is included. Finally, we will summarize the Chapter in Section 3.3.

3.1 cQED: a brief overview

3.1.1 LC Oscillator

One of the most simple circuits to use as a diving board into the sea of more complex cQED circuits is the parallel LC tank resonator. Here, an inductor L_r is in parallel with a capacitor C_r, drawn in Fig. 3.1(a). Here, for reasons that will become clear later when we introduce a JJ into the circuit, we will use the node flux in similar fashion to [104], defining it

$$\phi(t) = \int^t V(\tau)d\tau, \tag{3.1}$$

implying that

$$V(t) = \dot{\phi}. \tag{3.2}$$

A physical understanding of ϕ comes when considering the voltage across the inductor, which is $V(t) = L_r\dot{I}$, where I is the current through the device. With Eqs. (3.1,3.2), this immediately implies that ϕ is simply the flux threading the inductor coil. Hence, the energy stored in the inductor can be written

$$U_L = \frac{1}{2}I^2L_r = \frac{(IL_r)^2}{2L_r} = \frac{1}{2L_r}\phi^2; \tag{3.3}$$

similarly, since we know the voltage across the capacitor C_r we can write the energy related to it as

$$U_C = \frac{1}{2}C_rV^2 = \frac{C_r}{2}\dot{\phi}^2. \tag{3.4}$$

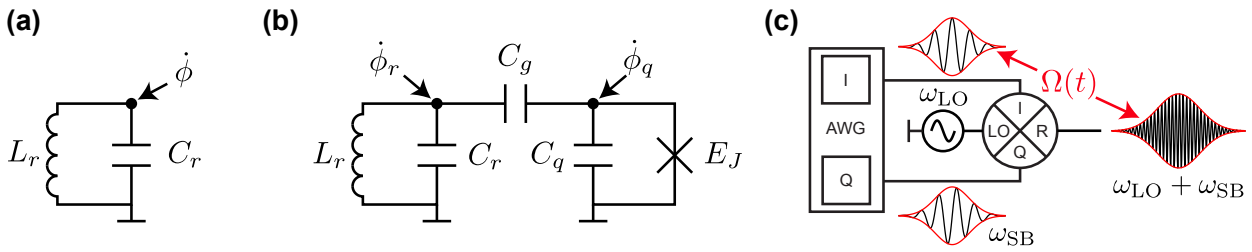

Figure 3.1: Relevant cQED circuits. **(a)** An LC tank circuit with denoted branch flux ϕ. **(b)** A transmon (Sec. 2.2.4) coupled to an LC tank circuit by a capacitor C_g. **(c)** Single-sideband signal generation setup with the ability to modulate both the amplitude and phase of the resulting signal.

The two expressions for U_C and U_L look like the kinetic and potential, respectively, energy terms of a Lagrangian system with coordinate ϕ written like

$$\mathcal{L} = T - U = \frac{C_r}{2}\dot{\phi}^2 - \frac{1}{2L_r}\phi^2 \tag{3.5}$$

with conjugate momentum

$$p = \frac{\partial \mathcal{L}}{\partial \dot{\phi}} = C_r\dot{\phi} = C_r V = q. \tag{3.6}$$

Running this through Euler-Lagrange, we can immediately see this resonance as

$$\ddot{\phi} = -\frac{1}{L_r C_r}\phi \equiv -\omega_r^2\phi, \tag{3.7}$$

where a natural resonance frequency of the cavity ω_r has become apparent. However this isn't the most useful way for us to view the dynamics of this system. Instead, we'll make a change of variables using Eq. (3.6) and write the Hamiltonian

$$\mathcal{H}_{LC} = q\frac{\partial \mathcal{L}}{\partial \dot{\phi}} - \mathcal{L} = \frac{q^2}{2C_r} + \frac{\phi^2}{2L_r}, \tag{3.8}$$

the familiar form of the quantum harmonic oscillator (QHO). Now, we will elevate the charge and flux to their operator representations, $\hat{q}$ an $\hat{\phi}$, respectively, and we will expand[1] the Hamiltonian to

$$\hat{\mathcal{H}}_{LC} = \left(\frac{\hat{\phi}^2}{\sqrt{2L_r}} + i\frac{\hat{q}^2}{\sqrt{2C_r}}\right)\left(\frac{\hat{\phi}^2}{\sqrt{2L_r}} - i\frac{\hat{q}^2}{\sqrt{2C_r}}\right) - i\left[\frac{\hat{\phi}}{\sqrt{2L_r}}, \frac{\hat{q}}{\sqrt{2C_r}}\right]. \tag{3.9}$$

Further simplification comes in the form of utilizing the fact that $\hat{q}$ and $\hat{\phi}$ are conjugate variables [Eq. (3.6)] and thus follow the relationship $[\hat{q}, \hat{\phi}] = -i\hbar$, and using a natural substitution suggested by the present form of Eq. (3.9):

$$\hat{a}^\dagger = \frac{(L_r C_r)^{1/4}}{\sqrt{\hbar}}\left(\frac{\hat{\phi}^2}{\sqrt{2L_r}} + i\frac{\hat{q}^2}{\sqrt{2C_r}}\right) \tag{3.10}$$

$$\hat{a} = \frac{(L_r C_r)^{1/4}}{\sqrt{\hbar}}\left(\frac{\hat{\phi}^2}{\sqrt{2L_r}} - i\frac{\hat{q}^2}{\sqrt{2C_r}}\right), \tag{3.11}$$

the so-called creation and annihilation operators, respectively, to arrive at the familiar

$$\hat{\mathcal{H}}_{LC} = \hbar\omega_r\left(\hat{a}^\dagger\hat{a} + \frac{1}{2}\right), \tag{3.12}$$

the QHO with $\hat{a}^\dagger\hat{a} = \hat{n}$, the number operator.

3.1.2 Transmon-cavity coupling

The circuit drawn in Fig. 3.1(b) can be used to write a Lagrangian

$$\mathcal{L} = \underbrace{\frac{1}{2}C_q\dot{\phi}_q^2 + E_J\cos\frac{2\pi\phi_q}{\Phi_0}}_{\text{transmon}} + \underbrace{\frac{1}{2}C_r\dot{\phi}_r^2 - \frac{1}{2L_r}\phi_r^2}_{\text{cavity}} + \underbrace{\frac{1}{2}C_g\left(\dot{\phi}_q - \dot{\phi}_r\right)^2}_{\text{coupling}}, \tag{3.13}$$

where ϕ_q, ϕ_r are the node flux at the qubit and resonator branches, respectively, of the coupled circuit. Here, the voltage across the coupling capacitor C_g is written as $(\dot{\phi}_q -$

[1] Using $\hat{x}^2 + \hat{y}^2 = (\hat{x} + i\hat{y})(\hat{x} - i\hat{y}) - i[\hat{x}, \hat{y}]$.

$\dot{\phi}_r$), defining the qubit side of the branch to be positive for no technical reason besides convention. Following a procedure similar to the previous section, the Hamiltonian for this circuit can be written as

$$\begin{aligned}\mathcal{H} &= \sum_i \dot{q}_i \frac{\partial \mathcal{L}}{\partial \dot{q}_i} - \mathcal{L} \\ &= \underbrace{\left[\frac{1}{2}(C_q + C_g)\dot{\phi}_q^2 - E_J \cos\frac{2\pi\phi_q}{\Phi_0}\right]}_{\text{transmon}} + \underbrace{\left[\frac{1}{2}(C_r + C_g)\dot{\phi}_r^2 + \frac{1}{2L_r}\phi_r^2\right]}_{\text{cavity}} + \underbrace{C_g\dot{\phi}_q\dot{\phi}_r}_{\text{coupling}}. \end{aligned} \tag{3.14}$$

Here, we will stop to identify that this Hamiltonian is really the sum of three parts: the qubit, the cavity, and a coupling between the two mediated by C_g. As discussed previously [Eq (2.24)], a transmon can be modeled as a CPB with Hamiltonian

$$\mathcal{H} = \underbrace{4E_C\hat{n}^2 + \frac{E_J}{2}\hat{\delta}^2}_{\text{HO}} - \frac{E_J}{4!}\hat{\delta}^4 + \mathcal{O}(\hat{\delta}^6) \tag{3.15}$$

where the good quantum variable of the system is $\hat{\delta}$ since the operable regime making the Josephson coupling energy much stronger than the electrostatic energy like $E_J/E_C \gtrsim 50$ [61]. Including up to the $\mathcal{O}(\hat{\delta}^4)$ terms and neglecting higher orders, neighboring energy splittings are anharmonic [Eq. (2.25,2.28)], allowing this circuit to be treated as a two-level quantum system to be used as a qubit. This means that the transmon part of the Hamiltonian can be written as

$$\hat{\mathcal{H}}_{\text{transmon}} \simeq \frac{\hbar\omega_q}{2}\hat{\sigma}_z, \tag{3.16}$$

where we can exclude all but the lowest energy splitting $\hbar\omega_q$, giving us a two-level system. Here, the frequency is shifted by the presence of C_g. The cavity Hamiltonian, following

the steps from the previous section, is written

$$\hat{\mathcal{H}}_{\text{cavity}} = \hbar\omega_r \left(\hat{a}^\dagger \hat{a} + \frac{1}{2}\right), \tag{3.17}$$

but here the resonance frequency is shifted by the presence of C_g to $\omega_r \sim (L_r(C_r + C_g))^{-1/2}$. The interaction Hamiltonian can be re-written using $q = C\dot{\phi}$ to

$$\hat{\mathcal{H}}_{\text{coupling}} = \frac{C_g}{\widetilde{C}^2} \hat{q}_q \hat{q}_r, \tag{3.18}$$

where $\widetilde{C} = \sqrt{C_g C_r + C_r C_q + C_q C_g}$ [104] and the charges on the respective branches have been elevated to capacitors. Using the charge operator[2]

$$\hat{q} = -i\sqrt{\frac{\hbar\omega C}{2}} \left(\hat{a} - \hat{a}^\dagger\right), \tag{3.19}$$

the coupling is written in a more accessible form

$$\hat{\mathcal{H}}_{\text{coupling}} = -\hbar \frac{C_g}{2} \sqrt{\frac{\omega_q \omega_r}{(C_q + C_g)(C_r + C_g)}} \left(\hat{a} - \hat{a}^\dagger\right) \left(\hat{\sigma}^- - \hat{\sigma}^+\right). \tag{3.20}$$

If we throw out terms in which energy isn't conserved[3], we can simplify the above to a familiar

$$\hat{\mathcal{H}}_{\text{coupling}} = \hbar \underbrace{\frac{C_g}{2} \sqrt{\frac{\omega_q \omega_r}{(C_q + C_g)(C_r + C_g)}}}_{g} \left(\hat{a}\hat{\sigma}^+ + \hat{a}^\dagger \hat{\sigma}^-\right) \stackrel{\text{def}}{=} \hbar g \left(\hat{a}\hat{\sigma}^+ + \hat{a}^\dagger \hat{\sigma}^-\right), \tag{3.21}$$

[2] Here, we will use the traditional annihilation (creation) operators $\hat{a}^{(\dagger)}$ for the linear resonator and the Pauli lowering (raising) operators $\hat{\sigma}^{-(+)}$ for the approximate two-level qubit.

[3] $\left(\hat{a} - \hat{a}^\dagger\right)\left(\hat{\sigma}^- - \hat{\sigma}^+\right) = \cancel{\hat{a}\hat{\sigma}^-} - \hat{a}\hat{\sigma}^+ - \hat{a}^\dagger\hat{\sigma}^- + \cancel{\hat{a}^\dagger\hat{\sigma}^+}$, where the slashed terms are terms which do not conserve photon number.

allowing us to write the full Hamiltonian for this system as

$$\begin{aligned}\mathcal{H}_{\text{JC}} &= \mathrm{H}_{\text{transmon}} + \mathrm{H}_{\text{cavity}} + \mathrm{H}_{\text{coupling}} \\ &= \frac{\hbar\omega_q}{2}\hat{\sigma}_z + \hbar\omega_r\left(\hat{a}^\dagger\hat{a} + \frac{1}{2}\right) + \hbar g\left(\hat{a}\hat{\sigma}^+ + \hat{a}^\dagger\hat{\sigma}^-\right),\end{aligned} \tag{3.22}$$

the Jaynes-Cummings Hamiltonian [105]. Here, we will finish by stating the results of [61] for the specific case where g satisfies $g \ll \Delta$ and $g \ll (\Delta + \alpha)$ where $\Delta \equiv \omega_q - \omega_r$ and α is the anharmonicity between the ω_{10} and ω_{21} transitions [see, for example, Eq. (2.28)]. In this limit, the Hamiltonian can be transformed to the effective system

$$\hat{\mathcal{H}}_{\text{eff}} = \frac{\hbar(\omega_{10} + \chi_{10})}{2}\hat{\sigma}_z + \hbar\left(\omega_r - \chi_{21}/2 + \chi\hat{\sigma}_z\right)\hat{a}^\dagger\hat{a}, \tag{3.23}$$

where $\chi = \chi_{10} - \chi_{21}/2$ is the effective dispersive shift of the cavity with $\chi_{ij} = g_{ij}^2/(\omega_{ij} - \omega_r)$ [61]. See also, e.g., Appendix C of [106] for a detailed derivation of the dispersive interaction in a similar qubit-cavity system. It is plain to infer from Eq. (3.23) that cavity frequency is dispersively shifted to a new effective frequency $\omega_r^{|i\rangle}$ which is dependent on the state of the qubit as measured with observable $\hat{\sigma}_z$. In this nomenclature, ω_r is the bare cavity frequency – the frequency of the cavity without regard to the qubit – and $\omega_r^{|i\rangle}$ is the so-called "dressed-$|i\rangle$" frequency of the cavity. More explicitly, this new frequency yields[4]

$$\omega_r^{|i\rangle} = \omega_r - \chi_{21}/2 \pm \chi, \tag{3.24}$$

$$\omega_r^{|1\rangle} - \omega_r^{|0\rangle} = 2\chi \simeq \frac{2g^2}{\Delta}\left(\frac{-\alpha}{\Delta - \alpha}\right). \tag{3.25}$$

For practical numbers such as qubit frequency $\omega_{10}/2\pi = 5$ GHz, cavity frequency $\omega_r/2\pi = 6$ GHz, and qubit-cavity coupling $g/2\pi = 100$ MHz, this yields a difference between the two dressed resonances of about $2\pi \times 3.3$ MHz. In crude terms, this alone shows that by

[4] Here, we will make the assumption that the system is only weakly anharmonic and thus $g_{21} \approx g_{10}$, $\Delta_{21} \approx \Delta_{10}$.

measuring the state of the cavity, one infers the state of the qubit[5]. The measurement of the state of a transmon qubit via a dispersively coupled resonator such as the system we've discussed above is discussed below.

Transmon Control

Control in cQED with superconducting circuits is traditionally done via the application of shaped microwave pulses wherein the control pulse can typically be modeled by $\Omega(t)\cos(\omega_d t - \gamma)$ where $\Omega(t)$ is the drive amplitude, ω_d is the drive frequency, and γ is the drive phase. In the lab, the experimentalist may achieve this by using a circuit like that seen in Fig 3.1(c); the in-phase (I) and quadrature (Q) ports of an IQ mixer are driven by arbitrary waveform generators (AWGs), providing control for both $\Omega(t)$ and γ by modulating the input local oscillator (L). The output tone leaves through the rf (R) port and heads to the qubit. This results in a waveform with functional form

$$V_{rf}(t) = \Omega(t)\cos\left[(\omega_{LO} + \omega_{SB})t - \gamma\right], \tag{3.26}$$

where ω_{LO} is the frequency of the tone generated by the LO and ω_{SB} is the sideband (SB) frequency driving the mixer's IQ ports [107][6]. Relying on the fact that the transmon is an anharmonic oscillator, we ignore the upper transmon levels and write an effective control Hamiltonian for a series of n control pulses [107]

$$\mathcal{H} = \hbar \sum_n \Omega_n(t)\cos(\omega_d t - \gamma_n)\hat{\sigma}_x - \frac{\hbar\omega_{10}}{2}\hat{\sigma}_z, \tag{3.27}$$

[5]This statement relies implicitly on the fact that the linewidth of the LC mode is smaller than the state-dependent frequency shift, i.e., $\kappa < 2\chi$. This will be discussed later in the context of measurement.

[6]The way this is written implies that the setup in use is that which is usually referred to as "single-sideband" mixing due to the fact that the output tone is dominated by a single frequency. Details on this can be found in [107].

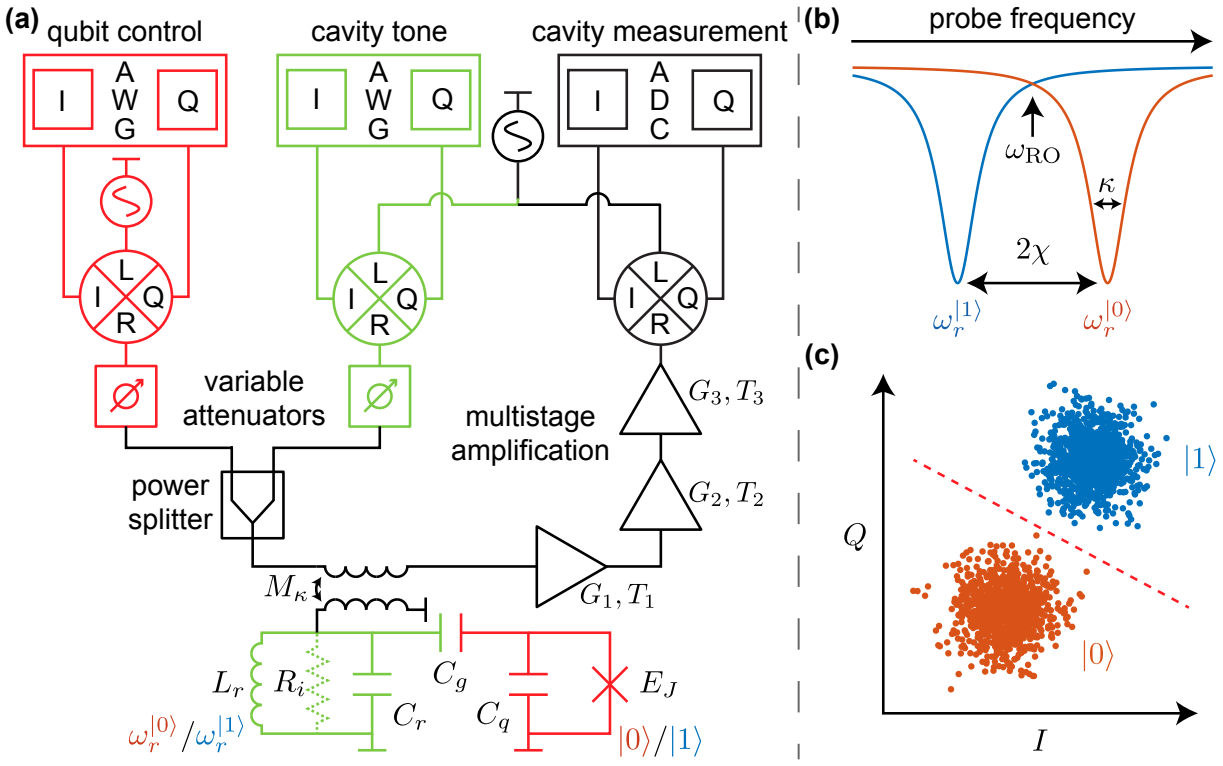

Figure 3.2: Sample signal setup for a cQED experiment with heterodyne detection. **(a)** Dual-channel arbitrary waveform generators (AWGs) drive mixer I and Q ports, modulating the amplitude, frequency, and phase of the coherent microwave tones at the mixer input. The resulting signals interact with the qubit-cavity system [similar to that depicted in Fig. 3.1(b)] via a coupling mutual inductance M_κ, after which they are amplified and mixed back down against the same local oscillator (heterodyne detection); the in-phase and quadrature information resulting from this process are then measured with a dual-channel analog-to-digital converter (ADC). **(b)** Simulated cavity response for the drawn circuit when the qubit is in state $|0\rangle/|1\rangle$. Here, $\mathrm{sgn}(\Delta) = -1$ and $g \ll |\Delta|$. **(c)** Simulated amplitude/phase cavity response for the drawn circuit for the states $|0\rangle/|1\rangle$ for many experiments. A simple way to assign a state to a given data point is to find the IQ-space centroids for both states and perform a simple threshold calculation; here, the points to the NE (SW) of the dashed line are assigned to the $|0\rangle$ ($|1\rangle$) state.

where here the amplitudes $\Omega_n(t)$ and phases γ_n of the n pulses are tuned to perform arbitrary coherent unitary rotations of the qubit state. This is more obvious when considering the control pulses in the rotating frame of the qubit where the Hamiltonian is transformed

to [107]

$$\widetilde{\mathcal{H}} = \frac{\hbar}{2} \sum_{n} \left[\cos(\gamma_n)\hat{\sigma}_x + \sin(\gamma_n)\hat{\sigma}_y \right]. \tag{3.28}$$

It is plain from the above that if one tunes γ appropriately for applied microwave tones [e.g. $\gamma = 0$ $(\pi/2)$ implies a rotation about the $x(y)$-axis]. A generic wire-up is presented in Fig. 3.2(a), showing how the control circuitry is often combined with measurement circuitry.

Measurement

Measurement of the transmon state via the resonant LC mode is traditionally accomplished in a standard heterodyne detection experiment; the essential components of such a measurement are included in Fig. 3.2(a). According to Eq.(3.25), one is able to infer the state of the transmon by measuring the resonance frequency of the LC mode to which is it coupled. This is depicted in Fig. 3.2(b) wherein the two different transmon states result in a state-dependent frequency of the dressed cavity $\omega_r^{|i\rangle}$. An important feature, as previously mentioned, is the total cavity mode linewidth (and decay rate) κ defined

$$Q_r = \omega/\kappa, \tag{3.29}$$

where Q_r is the quality factor of the resonant cavity mode and comprises a engineered coupling to the outside world Q_c and an internal quality Q_i as

$$\frac{1}{Q_r} = \frac{1}{Q_c} + \frac{1}{Q_i}. \tag{3.30}$$

Here, the internal quality factor Q_i is dependent on an intrinsic internal loss typically denoted as a parallel resistor R_i [depicted in Fig. 3.2(a)]. A physically useful way to describe these different contributions to the total quality factor is to consider through

which mechanism energy in the resonator will leave – or dissipate; in our experiments, we want our energy to leave through the engineered coupling mechanism such that we might measure the resonance frequency even when an exceedingly small amount of energy exists in the cavity instead of that energy being dissipated by the intrinsic loss of the cavity. This means that we desire $Q_c \ll Q_i,\ Q_r \sim Q_c$, implying that the total loss of the resonant mode is through the engineered coupling of the measurement circuit to the cavity. In the specific implementation drawn in Fig. 3.2(a), the coupling of the cavity mode out to the $Z_0 = 50\ \Omega$ environment can be written

$$Q_c = \omega_r \times \left(\frac{L_r}{R_{ext}/2}\right), \tag{3.31}$$

where R_{ext} is the coupling circuit as seen by the LC tank[7]. This can be written

$$\begin{aligned} R_{ext} = \mathrm{Re}(Z_{ext}) &= \left(\frac{1}{i\omega_r M_\kappa} + \frac{1}{Z_0}\right)^{-1} \\ &= \frac{\omega_r^2 M_\kappa^2/Z_0}{\left(1 + \omega_r^2 M_\kappa^2/Z_0^2\right)} \simeq \frac{\omega_r^2 M_\kappa^2}{Z_0}, \end{aligned} \tag{3.32}$$

making the coupling quality factor in this circuit

$$Q_c = \frac{2L_r Z_0}{\omega_r M_\kappa^2}, \tag{3.33}$$

which is easily tunable by choosing different values of M_κ. For some practical numbers – e.g., a cavity frequency $\omega_r/2\pi = 6$ GHz, coupling mutual of $M_\kappa = 20$ pH, and equivalent lumped element inductance of a $Z_0 = 50\ \Omega$-$\lambda/4$ coplanar waveguide (CPW) cavity resonator [108] $L_r = 4Z_0/\pi\omega_r$ – one acquires $Q_c \approx 11,000$ or a cavity decay rate of $1/\tau = \kappa \approx 1/(300\ \mathrm{ns})$. These choices are not purely arbitrary; the work presented in this thesis uses these CPW resonators as the LC mode to which transmon qubits are ultimately coupled and measured. The cavity decay rate in some sense sets a speed limit on mea-

[7] The factor of two here is because there are two leads in parallel through which energy may leave.

surement; if cavity photons take a long time to actually exit the cavity and move towards the detector, then measurement will take a long time regardless of any other influence. It should also be noted here that the above discussion relies on the aforementioned fact that $Q_c \ll Q_i$. Details on these types of resonators including many design considerations and fabrication optimization have been presented in the context of cQED-style experiments [102, 109–111]. The fabrication process used in the work presented in this thesis to produce a high Q_i CPW resonator is described later in Sec. 4.2.4.

A typical procedure for measuring the frequence difference in a short amount of time is to choose a single readout frequency ω_{RO} at the midpoint between the two dressed cavity states and record both the amplitude and phase information of the transmitted signal[8] via the usual heterodyne detection. Each experiment will result in a single point in IQ-space which when plotted results in a Gaussian blob as shown in Fig. 3.2(c). Here, two separate experiments were performed: one in which the $|0\rangle$ state is prepared and another for the $|1\rangle$ state. This allows the experimenter to calibrate their detection setup for the two states and then to continue on performing the next experiment of interest. This scheme is outlined in detail in a variety of works, and a vast wealth of research has gone into the improvement and optimization of such a readout scheme in recent years [61, 99, 112–115].

3.2 Josephson Amplifiers

Motivated by the need to perform fast, accurate measurements of the state of a linear cavity (see previous Section and [100, 116]), here we will briefly outline some of the first-stage amplifiers based on JJ devices with particular detail being given on the SLUG amplifier [117, 118], an amplifier based on a variant of a dc SQUID [119]. A wish list of properties for such an amplifier includes, but is not limited to:

- **Large gain×bandwidth:** While it may be obvious that an amplifier should have high

[8] n.b. in the circuit drawn in Fig 3.2(a), the readout is performed in transmission mode; similar analysis applies if instead one reflects a probe tone off of the LC cavity and measures the response that way.

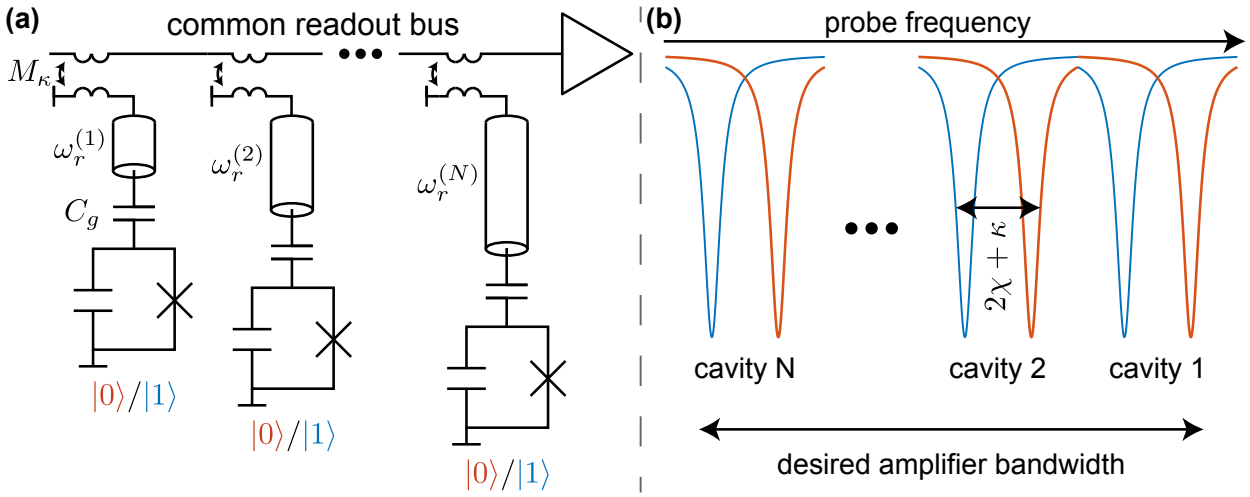

Figure 3.3: Multiplex scheme for multi-qubit cQED readout. **(a)** Circuit diagram; here, the cavities have undressed resonances $\omega_r^{(i)}$ which vary by changing the cavity length. Each cavity is coupled to a feedline in similar fashion to Fig. 3.2(a). **(b)** Sweeping a probe frequency on the common feedline will reveal state-dependent dressed resonance frequencies for each cavity. The goal of this panel is to give an eye to the desired bandwidth of an amplifier used to readout this circuit.

power gain, the usual tradeoff one needs to make is in the gain×bandwidth product. This is because there exists a desire to use as few amplifiers as possible to effectively readout the cavities of an eventual many-qubit processor. Figure 3.3 shows this schematically; here, a single amplifier is used to readout N cavities simultaneously. Since the cavities must be spaced apart such that the state-dependent shift 2χ of each cavity of width κ is visible, the bandwidth of our amplifier of choice must be *at least* $> N(2\chi + \kappa)$. In practice, though, there is typically an appreciable additional spacing between the resonances to account for any errors in design versus reality for ω_r, κ, and χ.

- **High saturation power:** If we want to simultaneously readout the state of N cavities, then we need to apply a multiplexed probe tone with N separate frequency components; this means the total signal has a higher power than any of the constituent separate tones. A reasonable amplifier should be able to simultaneously measure at

least 2-4 cavities without saturating[9].

- **High directionality:** In cQED measurement chains, typically the experimentalist needs to take many precautions to protect the quantum qubit-cavity circuit from classical noise from both the input and output of the measurement chain. By including an amplifier which is intrinsically nonreciprocal, one is simultaneously improving the signal of the measurement chain while also protecting the quantum circuit from downstream noisy devices (like other amplifiers or room temperature electronics). There is no "optimal" value for the directionality of an amplifier in this sense; in this case, bigger is always better.

- **Low added noise:** Using an amplifier is only going to help if it doesn't also add an overwhelming amount of noise to the measurement; in that sense, lower is always better. However, there exists a quantum limit as far as how much noise an amplifier must, at minimum, add [120]; amplifiers which follow this are typically called "quantum-limited amplifiers," or "near-quantum-limited amplifiers" depending on how close they operate to the limit of one-half of a quanta of added noise, the quantum limit. This is a particularly important metric for the first-stage amplifier in a measurement circuit since it will have the highest contribution to the noise temperature of the whole chain. For example, the three amplifiers in Fig. 3.2(a) would have an effective noise temperature provided by the Friis equation [121]

$$T_{\text{eff}} = T_1 + \frac{T_2}{G_1} + \frac{T_3}{G_2 G_1}, \tag{3.34}$$

  immediately implying that the temperature of the first stage dominates the effective noise temperature of the chain (provided that all $G_i \gg 1$).

- **Low added hardware:** In the context of scaling up to a one-day many-qubit processor,

[9] Saturation occurs when an amplifier's output no longer linearly increases with an increasing amplitude input signal.

the necessary auxiliary equipment required to realize its control and measurement must scale well with the number of qubits. Hence, if each added amplifier adds a significant amount of hardware, this must be taken into consideration when planning to move to a large number of qubits. An amplifier that requires only a small amount of additional hardware while perhaps otherwise performing not as well as another amplifier which requires significantly more hardware might be more attractive to someone constructing a very large scale quantum processor system.

To provide context for some of these requirements, a popular cryogenic amplifier and a current workhorse in cQED system measurement is the high-electron-mobility transistor (HEMT) amplifier. A HEMT, for most intents and purposes, is very powerful: the gain$\times$bandwidth of these amplifiers typically exceeds (40 dB$\times$5 GHz), they are not reciprocal devices, and they only require simple dc biases to function[10]. The downside to HEMT amplifiers in the context of cQED is noise and backaction; the HEMT is notorious for having a noisy input, meaning that it will send noise back towards the elements whose signal it is amplifying, as well as adding a relatively high number of noise photons ($\sim$ 20 [123]) to the signal to be amplified. It is for these reasons that the HEMT alone is not sufficient as a first-stage amplifier for high-fidelity cQED measurements, and thus many cQED practitioners have researched and developed several superconducting alternatives.

3.2.1 Superconducting Microwave Amplifier Zoo

JPA

The Josephson parametric amplifier (JPA) is essentially a nonlinear resonator where the key nonlinearity arises from the Josephson inductance; they have been demonstrated and characterized in a variety of implementations, including several in the context of cQED measurement chains [124–130]. The gain$\times$bandwidth of one of the more modern

[10]Here, the numbers quoted are for the Low-noise Factory HEMT model LNF-LNC4_8C [122].

implementations [130] is approximately (15 dB×700 MHz), with noise performance very near the quantum limit over the entire band. The JPA is likely the most widely used amplifier in cQED today due to these results. However, typical implementations of JPAs employ the amplifier in reflection mode, necessitating the use of at least cryogenic circulators and high-power rf pump tones, and also usually additional isolators and directional couplers to prevent the high-power rf field from propagating towards the quantum circuit; see wiring diagrams in, e.g., [127] or the supplement of [130].

JPC & JDA

The Josephson parametric converter (JPC) is a device which relies on coupling resonant modes to a four-JJ Josephson ring modulator as a nonlinear mixing element, which when pumped appropriately provides for amplification [128, 131, 132]. Here, devices typically maximize their gain×bandwidth to be about (20 dB×10 MHz) with center frequencies which are tunable via the pump tone frequency. While these amplifiers operate near the quantum limit, the limited bandwidth coupled with the extra rf wiring hardware requirements (circulators and couplers for the additional rf tones) for device operation hinder them in the context of a scalable amplifier system. A recent device in which two JPCs are coupled together is called the Josephson directional amplifier (JDA) [133, 134]. The JDA operates in a similar fashion to the JPC but the input and output ports are separated from the pump and idler and it has been shown to be non-amplifying in the reverse direction (see supplement of [134]), yielding a more convenient device than the JPC as far as scaling up.

TWPA

An amplifier which relies on the nonlinear inductance of a distributed resonant mode (the Kerr nonlinearity) has been developed in several realizations, the most common of which in the context of cQED are those which rely on high-kinetic inductance materials [135–138]

and also another family which relies more on the nonlinear inductance of the JJ [139–141]. These devices have demonstrated extremely broadband gain profiles, exceeding (15 dB×4.5 GHz) and have demonstrated to be near quantum limited as far as noise added (see, e.g., [139]). These devices, similar to those mentioned in the prior sections, also rely on exterior non-reciprocal devices like isolators, circulators, and directional couplers to manage the addition and subtraction of pump and idler tones and to provide for nonreciprocity (the theoretical reverse gain of these devices is unity). The Josephson TWPA (JTWPA) has grown in popularity in recent years and is finding its way into several modern cQED experimental apparatuses.

3.2.2 The SLUG

The superconducting low-inductance undulatory galvanometer (SLUG) amplifier [117, 118] is a variant of the dc superconducting quantum interference device (SQUID). While the so-far reported gain×bandwidth of the SLUG has stayed relatively low compared to other amplifiers (about 19 dB×50 MHz in [142]), the luxury is in the amplifier's simplicity of use; for a typical setup, one only needs two dc bias sources and, as mentioned below and in [143], one can use the inherent directionality of the SLUG to remove microwave isolators entirely from the measurement chain. This simplicity and inherent directionality, coupled with a relatively high saturation power [118] makes the SLUG particularly attractive as a first-stage amplifier in cQED measurements. Indeed, the SLUG has already been used as an amplifier for high-fidelity qubit readout, showing large improvements of SNR [142, 144].

Modeling

The SLUG can be modeled by considering the total current through two RCSJ model JJs which are interrupted by explicit inductances. Here, the current through the two JJs

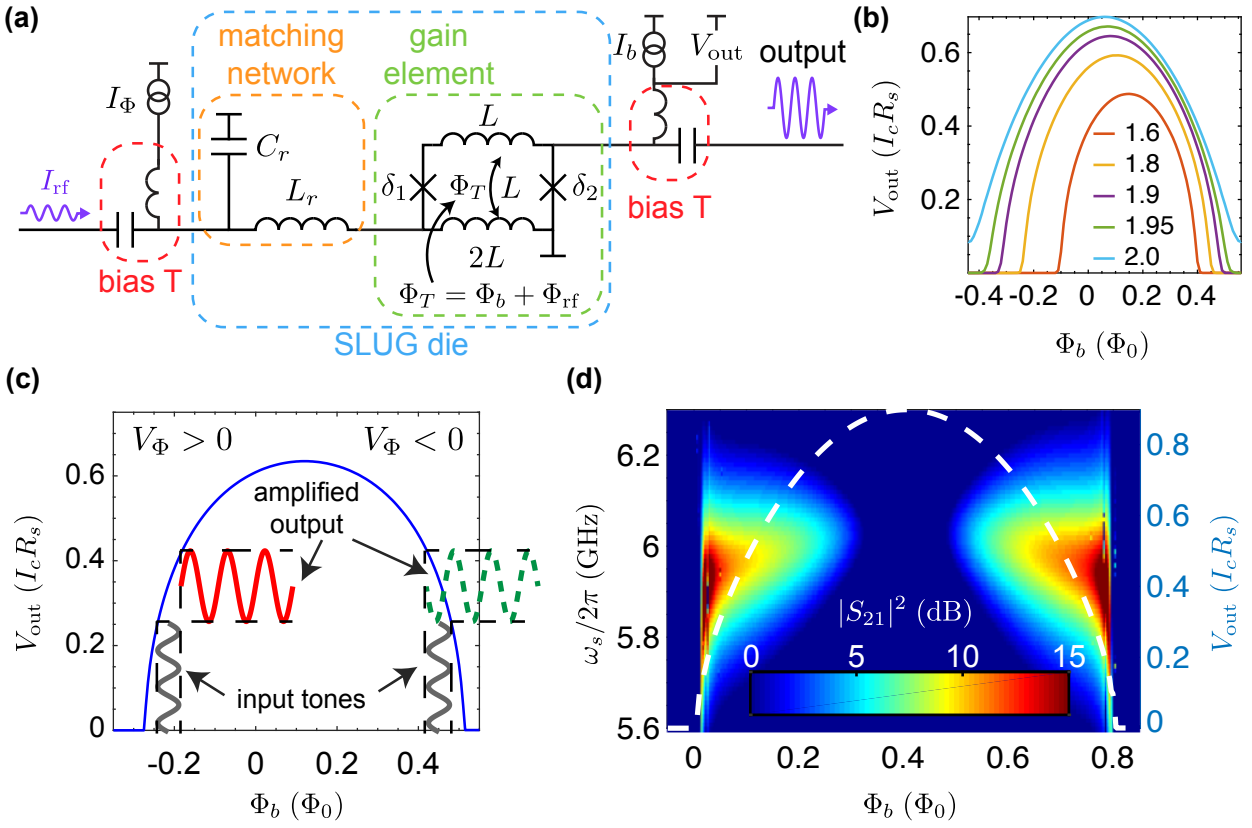

Figure 3.4: SLUG circuit model. **(a)** Basic wiring diagram for operation of a SLUG amplifier. Here, two dc biases I_b and I_Φ are added to the circuit via bias-T hardware. The signal to amplified I_{rf} is input to the SLUG via a single-pole lumped-element LC matching network. Here, the box labeled "SLUG die" indicated the microfabricated device circuit. This box will be replaced by the traditional triangle symbol for an amplifier in future figures. An optical micrograph of the circuit is shown in Fig. 3.5. **(b)** Simulated flux-to-voltage response curves for various values of current bias i_b. Simulation tools and methodologies used identical to those used in [117]. **(c)** Depiction of the gain mechanism in the SLUG; here, the operating point of the amplifier is chosen to be at a high $V_\Phi = dV_{out}/d\Phi_b$ value such that a small change in Φ will result in a large swing in V_{out}. We also note here that following [143], we have indicated the sign of V_Φ, as this plays a role in the reverse gain of the device. **(d)** Simulated gain (colormap) of the device as a function of both applied flux and signal tone frequency ω_s with overlaid flux-to-voltage curve (dashed white line) to show where the regions of highest gain in simulation should be. For this simulation, $\beta_C, \beta_L = 0.2$, the matching network is designed to center the gain curve at $\omega_r = 2\pi \times 6$ GHz with a characteristic impedance of 10 Ω. Here, the SLUG inductance is L = 10 pH.

($i \in \{1, 2\}$) is written, respectively,

$$I_i = I_0 \sin \delta_i + \frac{V_i - V_{N,i}}{R_s} + C_J \frac{dV_i}{dt}, \tag{3.35}$$

where $V_{N,i}$ is the voltage noise associated with lossy elements of the circuit, like the shunt resistors operating at finite temperature. Using the ac Josephson effect Eq. (2.2) for each JJ and defining a circulating current $J = (I_1 - I_2)/2$, along with quantizing the flux through the loop as $\Phi_T = (\Phi_0/2\pi)(\delta_2 - \delta_1)$, one re-writes this in a dimensionless form, for both JJs,

$$\beta_C \ddot{\delta}_1 = \frac{\delta_2 - \delta_1 - 2\pi\phi_b}{\pi\beta_L} - i_\Phi - \sin \delta_1 - \dot{\delta}_1 + \nu_{N,1} \tag{3.36}$$

$$\beta_C \ddot{\delta}_2 = -\frac{\delta_2 - \delta_1 - 2\pi\phi_b}{\pi\beta_L} + i_b + i_\Phi - \sin \delta_2 - \dot{\delta}_2 + \nu_{N,2}, \tag{3.37}$$

where here several dimensionless parameters $i \equiv I/I_0$, $\nu \equiv V/I_0R_s$, $\beta_C = (2\pi/\Phi_0)I_0C_JR_s^2$, and $\beta_L = 2I_0L/\Phi_0$ have been introduced; the dimensionless time is $\theta \equiv t/(\Phi_0/2\pi I_0R_s)$ [117]. The modeling for this circuit includes the leading LC matching network used to better match the low impedance SLUG circuit to the 50 Ω microwave environment. Figure 3.4(a) is the circuit diagram. The SLUG is both current-biased by I_b and flux-biased by I_Φ. In practice, the biases are T'd in off-chip using standard bias-T hardware. The signal input to the SLUG is partially impedance matched by a single-pole LC lumped-element mode before direct injection into the SQUID loop as a flux Φ_{rf}. Both JJs have critical current I_0 and are shunted by an explicit resistance R_s and capacitance C_J [not drawn; similar to the circuit diagram in Fig. 2.2(b)]. This will operate in the overdamped regime with $\beta_C = (2\pi/\Phi_0)I_0C_JR_s^2 < 1$. Full details for simulation of this circuit are available in [117, 143].

Figure 3.4(b) are simulated flux to voltage curves for various values of i_b ($i_b = 2$ is the total critical current of the device). The slope of these curves $V_\Phi \equiv dV/d\Phi$ plays an important role of the gain in the device; where V_Φ is large, a small change in flux results in a larger swing in voltage. Since we inject the signal into the SLUG as a directly coupled

flux Φ_{rf}, this immediately gives us the gain mechanism of the device [117, 143].

Device Fabrication

The SLUG microwave ground plane is realized in a 90 nm-thick Nb film grown by dc magnetron sputtering. The dielectric materials required for the multilayer stack are deposited using plasma enhanced chemical vapor deposition (PECVD). The SLUG amplifier circuit incorporates three superconducting Nb layers, two insulating SiO_x layers, one normal metal Pd layer, and two Nb/Al-AlO_x-Al/Nb JJs with critical current density $J_c \sim 3\,kA/cm^2$ and areas $2 \times 1\mu m^2$. The JJs are shunted by thin-film Pd resistors formed by electron-beam evaporation and liftoff. In areas where good metallic contact is required between wiring layers, an *in situ* Ar ion mill cleaning step is used to remove native NbO_x prior to metal deposition. Figure 3.4(f, g) shows a cross-sectional depiction of the layer stack and a top-down optical micrograph, respectively. In Fig. 3.4(f), the Nb layers are false-colored in blue, the SiO_x dielectric layers are colored brown, and the Pd shunt resistor is shown in red. A black $\times$ marks the location of a Nb/Al-AlO_x-Al/Nb junction interface. Figure 3.5 shows an optical micrograph of a completed device.

1. **Layer M1:** An Si wafer with 150 nm of thermal SiO_2 is coated with a film of Nb. Here and below, sputter conditions are tuned to yield films with slight compressive stress [145]; the deposition rate is 45 nm/min. This layer is patterned with an i-line step-and-repeat (stepper) lithography tool and etched with an SF_6-based RIE plasma.

2. **Layer D1:** A plasma-enhanced chemical vapor deposition (PECVD) process is used to grow a conformal layer of SiO_x. This layer is patterned with an i-line stepper and etched with a CHF_3-based reactive ion etch (RIE) plasma. The RIE power and pressure are optimized to transfer a 45° slope into the dielectric sidewalls in order to promote step coverage of subsequent layers. This is depicted by the illustration in Fig. 3.4(a).

Layer ID	Material	Thickness (nm)	Surface Pre-treatment	Deposition Method	Patterning	Etch Chemistry	Function
M1	Nb	90	–	dc sputtered	i-line	SF_6	ground plane CPW feedlines
D1	SiO_x	180	–	PECVD	i-line	CHF_3	SLUG circuit wiring ground vias
M2	Nb	90	*in situ* ion mill	dc sputtered	i-line	SF_6	inductors SLUG JJ base layer
D2	SiO_x	180	–	PECVD	i-line	CHF_3	JJ definition shunt resistor vias
M3	Nb Al-AlO_x-Al	100	*in situ* ion mill	dc sputtered w/*in situ* oxidation	i-line	SF_6 TranseneA	SLUG input coupling SLUG JJ counterelectrodes CPW crossovers
R	Ti/Pd	20	*in situ* ion mill	e-beam evaporated	i-line	–	shunt resistors

Table 3.1: Layer stack description of the SLUG amplifier circuit.

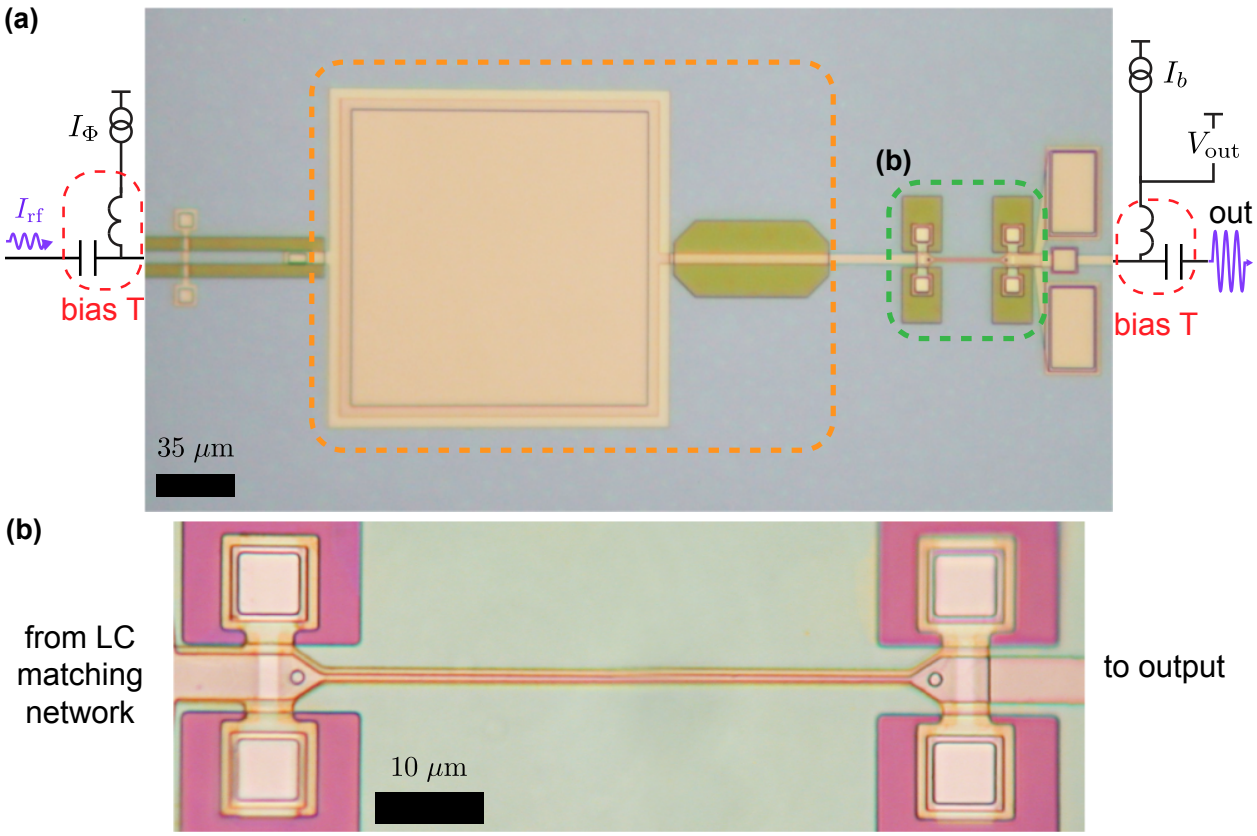

Figure 3.5: Optical micrograph of the fabricated SLUG amplifier circuit. **(a)** The full on-chip circuit including both the LC lumped element resonator and the gain element. **(b)** Zoom-in on the gain element. The two photographs in **(a)** and **(b)** are from two different devices with different SLUG inductance.

3. **Layer M2:** The bottom Nb electrode for the SLUG JJs is sputtered. This layer is patterned with an i-line stepper and etched with an SF_6-based RIE plasma.

4. **Layer D2:** Another SiO_x layer is grown by PECVD. This layer is patterned in the same manner as in step 2. At this step, particular care is taken to eliminate solvent or other organic residues from the dielectric vias, as these vias will define the SLUG JJs.

5. **Layer M3:** The SLUG JJs and signal wiring are formed in the following process:

   (a) The wafer is transferred into the sputter system load-lock chamber and the chamber is pumped down for ~ 1 hour.

   (b) While the load lock is pumping out, the primary vacuum chamber is "seeded"

with pure O_2 using similar conditions to the actual junction oxidation. We find that this step improves the reproducibility of the junction specific resistance by ensuring as similar a chamber chemistry as possible from run to run.

(c) The wafer is transferred into the primary vacuum chamber and the system is allowed to pump down to base pressure (about 5×10^{-8} Torr).

(d) An *in situ* ion mill is used to remove the NbO_x from the M2 electrode layer.

(e) An Al seed layer of thickness ~ 8 nm is sputtered.

(f) The barrier oxide is grown. The AlO_x barrier layer is seeded by flowing O_2 at low pressure (~ 1 mTorr) for 2 minutes. The chamber is then valved off from the pumps and the O_2 pressure is quickly ramped to the target value (typically ~ 10 mTorr), where it remains for the duration of the oxide growth (typically about 2 minutes).

(g) The growth chamber is pumped back to vacuum. An Al cap layer of ~ 6 nm thickness is sputtered, followed by the 90 nm Nb junction counterelectrode.

This layer is patterned with an i-line stepper. The Nb is removed with an SF_6-based RIE plasma while the Al-AlO_x-Al is removed with a Transene A Al wet-etch.

6. At this point, it is possible to probe the 4-wire resistances of witness junctions cofabricated on the die with the SLUG circuit. The expected critical currents are extracted using the Ambegaokar-Baratoff relation [146].

7. **Layer R:** A negative photoresist is patterned with an i-line stepper to define the shunt resistors. The resistors are formed by electron-beam evaporation of Pd following an *in situ* ion mill and deposition of a thin (~3 nm) Ti adhesion layer. Liftoff is performed in acetone at room temperature over several hours with slight manual agitation of the wafer.

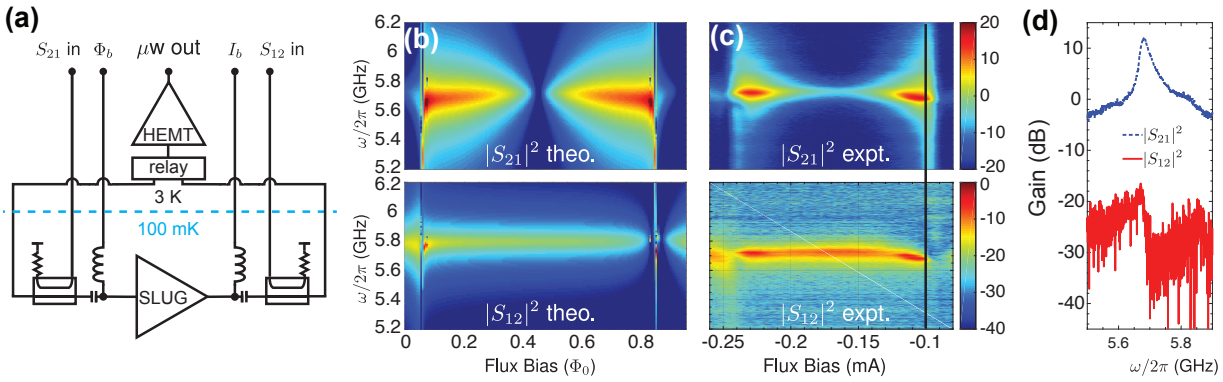

Figure 3.6: SLUG forward and reverse gain [143]. (a) Circuit for measurement of forward and reverse gain. (b) Numerical calculation of the forward and reverse scattering parameters as a function of flux bias and frequency. (c) Measured forward and reverse scattering parameters. (d) 1D cuts from (c), showing forward and reverse gain versus frequency for large $|V_\Phi|$, $V_\Phi < 0$.

3.2.3 Reverse backaction and directionality of the SLUG

As mentioned previously in the amplifier wishlist (the beginning of Sec. 3.2), one desirable aspect to an amplifier for use in cQED experiments is that the amplifier will protect the quantum circuit from upstream noise; this includes not being a generator of noise itself. The SLUG is well-poised to fit both of those criteria. The SLUG is a variant of the dc SQUID, which has been previously shown to be an intrinsically non-reciprocal amplifier [147, 148]. Here we will briefly outline the some of the experiments performed in [143] while pointing the intrepid reader to the referenced article for full details.

Scattering Parameters

Measuring the scattering parameters[11] of the 2-port SLUG amplifier is a straightforward experiment. The wiring diagram in Fig. 3.6(a) [143] allows for the measurement of both $|S_{12}|^2$ and $|S_{21}|^2$ in the same cooldown, though not simultaneously since the HEMT amplifier only has a singular input. Essentially, a probe tone at frequency ω is sent to the SLUG via the S_{21} (S_{12}) input port to measure the forward (reverse) gain of the amplifier and

[11]The author assumes the reader has a familiarity with scattering parameters of microwave circuits. That not being the case, the author recommends [108] as a reference on the subject.

reflections from these ports allow a full S-matrix measurement of the device [149]. The measured forward and reverse gain, along with the respective simulation for a nominally similar device [118], are shown in Fig. 3.6(b, c) with linecuts along the $V_\Phi < 0$ shoulder of the flux-to-voltage curve in Fig. 3.6(d), highlighting the fact that the SLUG is intrinsically non-reciprocal as an amplifier when operated in this fashion [143].

Backaction from the SLUG

Backaction from the SLUG, i.e., noise from the SLUG input towards the quantum circuit, can be studied using a qubit-cavity system which is upstream from the amplifier. There are two primary experiments which have been presented in detail in [143]. Treating the SLUG as a thermal noise source implies that the noise which it emits follows a broadband distribution. Looking specifically at noise at the qubit frequency, one expects dephasing [150, 151], however in the qubit-cavity system the noise at this frequency is significantly filtered by the cavity (the transfer function of noise into the cavity is strongly dependent on the cavity frequency and linewidth). However, being a broadband noise source implies that noise is also being emitted at the cavity frequency, which will both Stark shift the qubit and induce dephasing [152, 153].

Detecting cavity photons using the qubit can be done by the following protocol: when the SLUG is not in use, leave it in the supercurrent state using flux bias Φ_{off}. Some time prior to the start of the experiment, adjust the flux bias to Φ_{on} to "turn on" the SLUG to use it both as an amplifier for readout and a noise source for the experiment. Here, we have no isolators or circulators between the qubit-cavity system and the SLUG [see wiring diagram in Fig. 3.7(a)] and a depiction of Φ_{on} vs Φ_{off} in Fig. 3.7(b)]. The experiment sequence is outlined in the panel atop Fig. 3.7(c); here, we pulse the SLUG on a variable time ("heat start" time) prior to a Ramsey experiment. This will cause the SLUG to begin noise emission towards the qubit-cavity system. The Ramsey fringe data in Fig. 3.7(c) shows that for longer head-start times, we see a degradation of qubit coherence as well as a shift in the qubit

frequency. This shift in the qubit frequency can be explained by photons in the cavity ac Stark shifting the qubit frequency and is detailed in [143].

Another experiment carried out is to check that the SLUG can protect the qubit-cavity system from downstream noise in the measurement chain. It is also interesting here to measure this effect as a function of frequency since noise sources can be broadband. One method of measuring such an effect is outlined by the pulse sequence atop Fig. 3.7(d). Here, motivated by the results of the previous paragraph, the SLUG is only pulsed on just prior to the measurement pulse. Thus, the full sequence is as follows: while the SLUG is off, invert the qubit population with an X pulse. Immediately following, adjust the qubit frequency using the flux threading the qubit SQUID loop (recall Sec 2.1.4) for the duration of the idle time in an otherwise standard T_1 experiment. After the idle time has finished, flux pulse both the qubit back to where it started and the SLUG to the "on" position and measure the state of the qubit. This allows us to sample noise at various frequencies during the time in which the qubit is flux-shifted to those frequencies [151]. The data for such an experiment is shown in Fig. 3.7(d) both for using the SLUG versus using an isolator to protect the qubit-cavity system from downstream noise (from, e.g., the HEMT noisy HEMT amplifier). We see no significant difference in T_1 over the entire sampled qubit frequency space, implying that the SLUG operated in this fashion protects the qubit-cavity system just as well as a commercial isolator.

3.3 Summary

In this Section, we have briefly outlined several aspects of cQED as they are relevant to this thesis. Starting with the LC harmonic oscillator and moving to a coupled qubit-cavity system using the transmon model, we have skimmed the surface of rich physics which can be done using relatively simple macroscopic circuit elements. Once through the introduction to cQED, we then outlined the need for a high-quality first-stage amplifier in

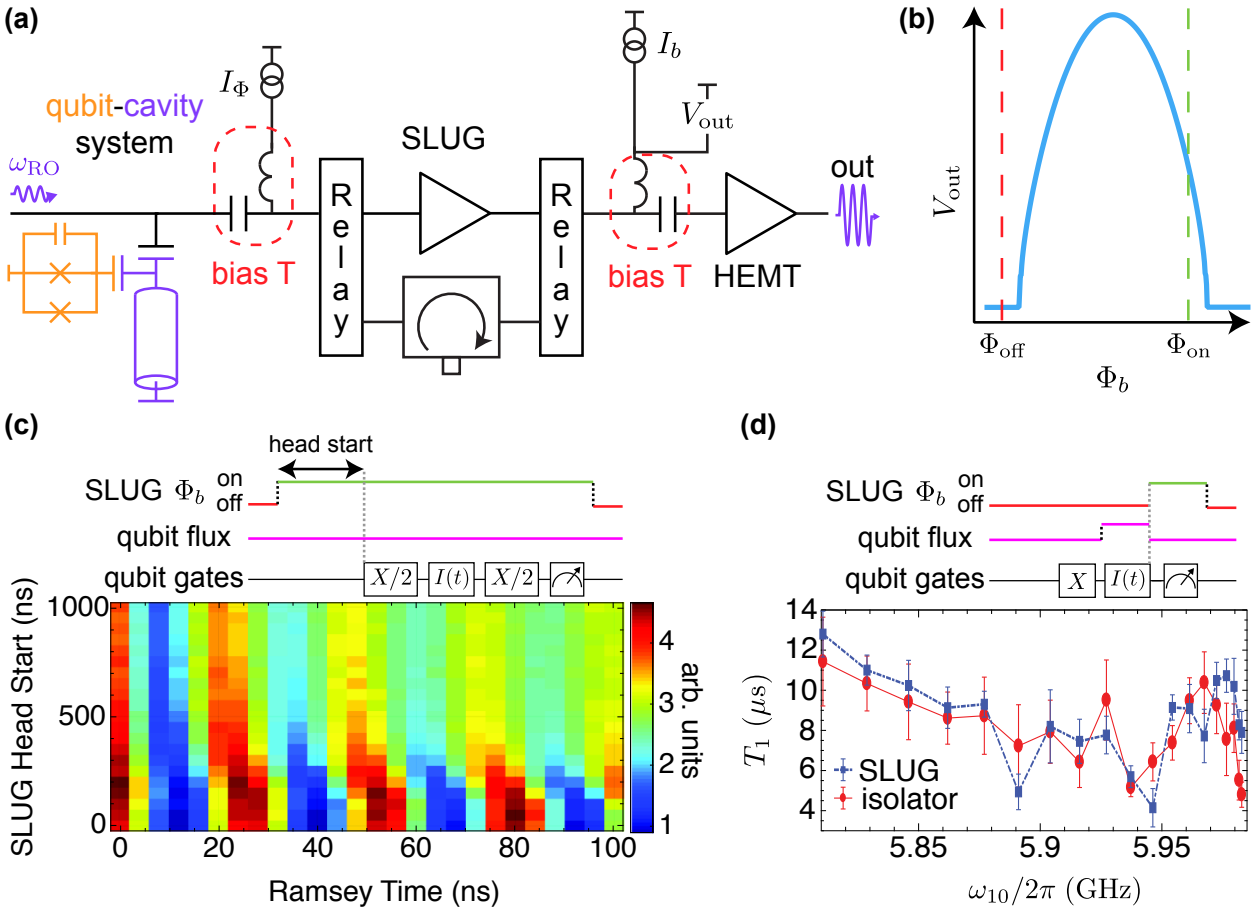

Figure 3.7: SLUG backaction experiments. **(a)** Wiring diagram for the experiments in hand. Here, the source for I_Φ is a combined dc current source with a 1 GS/s AWG assist such that one can quickly switch from one flux point to another. An exceedingly similar circuit is in Fig S3 of [154] where the qubit control Z-DAC and a voltage source are T'd together in the mK environment. There are no additional isolators or circulators other than the explicitly drawn isolator in the panel. **(b)** Diagrammatic depiction of example "SLUG on" (Φ_{on}) and "SLUG off" (Φ_{off}) flux bias points. In the "off" position, the SLUG is a superconducting short to ground. In the "on" position, the SLUG is both acting as an amplifier and a noise source for these experiments. **(c)** Ramsey fringes acquired for various SLUG head start times. Here we see that for longer head-start times, the coherence is degraded and the frequency of the fringes shifts. This implies that if the SLUG can be pulsed-on just prior to measurement, it will not poison the quantum circuit. **(d)** Comparing T_1 times as a function of qubit frequency and SLUG vs. isolator in the measurement chain. Here, the SLUG is pulsed on just prior to the measurement pulse. No significant difference is found between using the SLUG versus an isolator.

cQED systems. This motivated a brief overview of some of the current leading amplifiers in use by practitioners of cQED as well as a more in-depth dive into the SLUG amplifier as a low-noise, intrinsically non-reciprocal first-stage amplifier. Where most of the other leading amplifiers in the field require the use of a variety of other non-reciprocal hardware – such as cryogenic microwave isolators and circulators – it has been shown here (and in greater detail here [143]) that the SLUG is able to act as both an isolator and an amplifier simultaneously while requiring minimal additional cryogenic hardware to enable its utilization. It is the author's view that the SLUG amplifier could play an important role in a one-day large-scale quantum processor based on superconducting qubit-cavity systems since most of the alternatives require an enormous amount of hardware overhead to enable their utilization.

4 DIGITAL CONTROL OF A SUPERCONDUCTING QUBIT

4.1 Introduction

As has been discussed in the past Chapters of this work, Josephson qubits are a promising candidate for the construction of a large-scale quantum processor [42–45]. Gate and measurement fidelities have surpassed the threshold for fault-tolerant operations in the two-dimensional surface code [23, 154], and the successful demonstration of small repetition codes [155, 156] provides a direct validation of the fidelity of the quantum hardware and control and measurement elements that will be needed for a first demonstration of error-protected logical qubits. Current approaches to the control of superconducting qubits rely on the application of pulsed microwave signals. The generation and routing of these control pulses involve substantial experimental overhead in the form of room-temperature and cryogenic electronics hardware. This includes, but is not limited to, coherent microwave sources, arbitrary waveform generators, quadrature mixers, and amplifiers, as well as coaxial lines and signal conditioning elements required to transmit these signals into the low-temperature experimental environment.

While brute-force scaling of current technology may work for moderate-sized superconducting qubit arrays comprising hundreds of devices, the control of large-scale systems of thousands or more qubits will require fundamentally new approaches. An attractive candidate for the control of large-scale qubit arrays is the SFQ digital logic family [84] which has been previously introduced in Chapter 2. In SFQ digital logic, classical bits of information are encoded in fluxons, propagating voltage pulses whose time integral is precisely quantized to $h/2e \equiv \Phi_0$, the superconducting flux quantum. Here, the presence (absence) of a quantized flux pulse across a Josephson junction (JJ) in the SFQ circuit during a given clock cycle constitutes the classical bit “1" (“0"). There have been prior attempts to integrate SFQ digital logic with superconducting qubits [157–159], with some notable recent successes in the area of qubit measurement [160]. The work presented here is motivated by

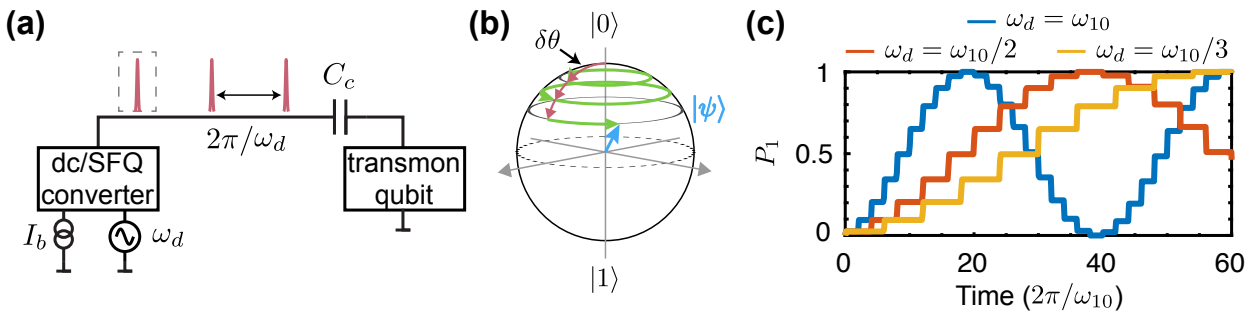

Figure 4.1: Coherent control of a qubit using SFQ pulses. **(a)** Block diagram of the experiment. An external microwave tone with frequency ω_d is used to trigger a dc/SFQ converter, which generates a train of pulses with interpulse timing of $2\pi/\omega_d$; the resulting pulse train is coupled capacitively to a transmon qubit. **(b)** Trajectory of the qubit state vector on the Bloch sphere due to a resonant train of SFQ pulses. Each SFQ pulse induces an incremental rotation; the green parallels represent qubit free precession in between SFQ pulses. **(c)** Simulated qubit Rabi oscillations for SFQ drive at various subharmonics of the qubit transition frequency ω_{10}. Discrete steps in excited state population $P_1(t)$ are induced by the arrival of single SFQ pulses; in between pulses, the qubit undergoes free precession with no change in $P_1(t)$. In **(b)** and **(c)**, a large, non-optimal value of $\delta\theta = \pi/10$ is chosen for the purpose of display.

a previous study which showed that resonant trains of SFQ pulses can be used to induce high-fidelity qubit rotations, with gate fidelity limited by leakage errors [161]. Subsequent work based on optimal control theory provided a proof-of-principle demonstration that leakage errors can be suppressed significantly by clocking control bits at a higher frequency and allowing variation in the pulse-to-pulse timing intervals [162].

In this Chapter, we describe the arbitrary coherent control of a superconducting transmon qubit driven by SFQ pulses. The SFQ pulses are generated by a dc/SFQ converter [83, 84] cofabricated on the same chip as the qubit. The basic scheme of the experiment is shown in Fig. 4.1(a). The SFQ driver circuit is biased with a dc current and an external microwave tone is applied to the trigger port of the driver. When the trigger tone amplitude exceeds a certain threshold, SFQ pulses are generated and coupled capacitively to the qubit. Each

pulse induces an incremental rotation on the Bloch sphere ([161], also see Sec. 4.2.1)

$$\delta\theta = C_c \Phi_0 \sqrt{\frac{2\omega_{10}}{\hbar C_\Sigma}}, \tag{4.1}$$

where C_c is the coupling capacitance between the SFQ driver and qubit, C_Σ is the qubit self-capacitance, and ω_{10} is the qubit fundamental transition frequency. When the pulse-to-pulse spacing is matched to an integer multiple n of the qubit precession period $2\pi/\omega_{10}$, the state vector undergoes a coherent rotation on the Bloch sphere [see Fig. 4.1(b)] about a control vector whose direction is determined by the relative timing of the pulse sequence. In Fig. 4.1(c) we show simulated SFQ-induced Rabi oscillations for SFQ pulse trains resonant with ω_{10} as well as subharmonics $\omega_{10}/2$ and $\omega_{10}/3$; here, for the purposes of display we assume a large, non-optimal, per-pulse rotation $\delta\theta = \pi/10$. A related idea for selective excitation was pursued by some early practitioners of nuclear magnetic resonance, who termed the pulse sequence DANTE (Delays Alternating with Nutations for Tailored Excitation), as the terraced trajectory of the state vector on the Bloch sphere recalls the multilevel structure of the *Inferno* [163, 164].

This Chapter is organized as follows. First, in Section 4.2, we provide select details behind the theory of SFQ based qubit control, describe the SFQ driving circuit used in this work, and detail the cofabrication of the SFQ pulse driver and transmon qubit on a single chip; in our design, we are able to then separately characterize the SFQ driver and qubit circuits. In Section 4.3, we discuss implementation of an arbitrary gate set using SFQ pulses and present the results of gate characterization using interleaved randomized benchmarking (RB) [165]; the achieved gate fidelities $\mathcal{F} \sim 95\%$ are limited by quasiparticle (QP) poisoning of the qubit induced by operation of the dissipative SFQ pulse driver. Motivated by the QP-induced gate infidelity, Section 4.4 discusses experiments to characterize the real and imaginary parts of the QP admittance seen by the qubit and explores the dynamics of QP generation and relaxation in the circuit. Finally, in Section 4.5 we summarize this Chapter

and detail future devices based on an MCM flip-chip architecture which will help mitigate the deleterious effects of QPs on qubit coherence. The work presented in this Chapter is presented in journal article form here [166], albeit with slightly fewer details.

4.2 The Quantum-Classical Hybrid Circuit

4.2.1 SFQ control of a transmon

Starting with the Cooper-pair box Hamiltonian from Eq. (2.22) and performing a similar expansion of the $\cos\delta$ term as in Eq. (2.24), one is able to write a Hamiltonian for the SFQ-control system as seen in Fig. 4.1(a) as

$$\hat{\mathcal{H}} \approx \frac{\left(\hat{Q} - C_c V(t)\right)^2}{2C_\Sigma} + \frac{E_J}{2}\hat{\delta}^2 - \frac{E_J}{4!}\hat{\delta}^4, \tag{4.2}$$

where $V(t)$ is the output of the dc/SFQ converter block and C_Σ is the total capacitance of the transmon island. If we make the assumption that C_c is sufficiently small, we can write this like

$$\hat{\mathcal{H}} \approx \underbrace{\frac{\hat{Q}^2}{2C_\Sigma} + \frac{E_J}{2}\hat{\delta}^2 - \frac{E_J}{4!}\hat{\delta}^4}_{\text{transmon}} - \underbrace{\hat{Q}V(t)\frac{C_c}{C_\Sigma}}_{\text{control}}. \tag{4.3}$$

The control term of this Hamiltonian can be treated on its own; using the charge operator in the basis of an oscillator $\hat{Q} = -\sqrt{\hbar\omega_{10}C_\Sigma/2}\hat{\sigma}_y$, the control Hamiltonian becomes

$$\hat{\mathcal{H}}_{\text{control}} = -\hat{Q}V(t)\frac{C_c}{C_\Sigma} = C_c V(t)\sqrt{\frac{\hbar\omega_{10}}{2C_\Sigma}}\hat{\sigma}_y. \tag{4.4}$$

Integrating this Hamiltonian using the time-dependent Schrödinger equation, one arrives at

$$|\psi(t)\rangle = \exp\left[-i\underbrace{\left(C_c\sqrt{\frac{2\omega_{10}}{\hbar C_\Sigma}}\int V(t)dt\right)}_{\delta\theta}\hat{\sigma}_y/2\right]|\psi(t=0)\rangle, \tag{4.5}$$

where the angle of rotation $\delta\theta$ can now readily be identified by equating Eq. (4.5) to the general rotation operator $\mathcal{D}_y(\delta\theta) = \exp(-i\delta\theta\hat{\sigma}_y/2)$. In the preceeding text, we have stated that the pulses to be used are sharp in time with respect to the qubit precession period, and so we will treat them as Dirac-δ functions for the time being, implying that a single pulse has a voltage waveform

$$V(t) = \Phi_0\delta(t), \tag{4.6}$$

which means that the $\delta\theta$ term in Eq. (4.5) becomes

$$\delta\theta = C_c\sqrt{\frac{2\omega_{10}}{\hbar C_\Sigma}}\int \Phi_0\delta(t)dt = C_c\Phi_0\sqrt{\frac{2\omega_{10}}{\hbar C_\Sigma}}, \tag{4.7}$$

which is tunable via a simple geometric capacitance C_c, as previously prescribed [161]. A more interesting – and for reasons that will soon be clear – and practical pulse waveform, however, is the resonant pulse train of δ-like pulses which are timed with the qubit precession period or a subharmonic thereof. The form of this train for N pulses with a time T between them is given by

$$V(t) = \Phi_0\left[\delta(t) + \delta(t-T) + \cdots + \delta(t-(N-1)T)\right], \tag{4.8}$$

where in the case for this work $T = 2\pi n/\omega_{10},\ n \in \mathbb{N}$. Here, the number of pulses required to effect a rotation of angle Θ is given by $n\delta\theta = \Theta$.

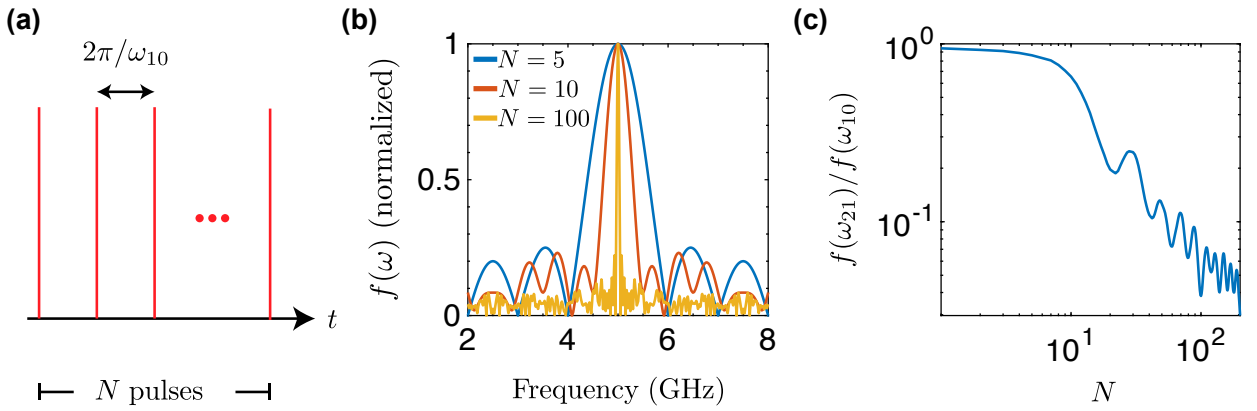

Figure 4.2: Fourier spectrum of SFQ pulse trains. **(a)** A train of N pulses spaced by a time $T = 2\pi n/\omega_{10}$. **(b)** Fourier spectrum for various pulse train lengths. The more pulses in a train, the more concentrated the spectral content of the train is at the frequency of interest, in this case $\omega_{10}/2\pi = 5$ GHz. **(c)** The relative magnitude of the Fourier spectrum $f(\omega)$ at $\omega_{21} = 2\pi \times 4.75$ GHz, implying an anharmonicity of $\alpha/2\pi = -250$ MHz, as a function of pulse train length N. For longer trains, the relative spectral power at the ω_{21} transition becomes smaller. This is important since we do not want to inadvertently excite the qubit out of the computational manifold, but we also do not want our gate times to be infinite; a practical trade-off between gate time and leakage error must be made [161, 162].

An obvious question to ask is: if shorter gate times is the goal, why not set $\delta\theta$ – by changing C_c – to be large such that a short pulse train can be used for the rotation? The answer is two-fold: the first reason lies in the spectral content of the overall pulse train; a single δ-like pulse is broadband in spectral content while a train of several pulses can be used to concentrate the spectral energy at a frequency of interest. This is outlined in Fig. 4.2 where the Fourier spectrum of various pulse lengths is shown as well as the relative magnitude of the spectral component for frequency ω_{21}, which could excite the qubit out of the computational manifold. This is described in detail in the context of a multi-level transmon in previous works [161, 162]. The second reason is that a large capacitance from the dc/SFQ converter could provide access to a significant loss channel to the qubit limit its coherence times [167]. In this case, a smaller capacitance is always better to reduce the coupling of the qubit to the outside world, but it doesn't practically limit our circuits today; state of the art planar transmon devices with coherence times approaching ~ 100 µs have

been demonstrated [44, 45] while the Purcell limited T_1 of our circuit is found to be [112]

$$RC = \left[\frac{1+\omega_{10}^2 C_c^2 R_s^2}{\omega_{10}^2 C_c^2 R_s}\right] C \sim 470\ \mu s, \tag{4.9}$$

where $R_s = 1\ \Omega$ is the total shunt resistance of the dc/SFQ converter, $C = 75$ fF is the qubit self-capacitance, $C_c = 400$ aF is the SFQ-qubit coupling capacitance, and $\omega_{10}/2\pi = 5$ GHz is the qubit frequency ; this assumes a qubit frequency of $\omega_{10}/2\pi = 5$ GHz. The implication here is that other factors are limiting current transmons devices, so the extra coupling from this control line should have minimal effect. We are also not motivated in going to a larger C_c for the reasons outlined above as far as the spectral content of pulse trains with small N.

4.2.2 dc/SFQ Converter

The SFQ pulse circuit used to perform qubit control in this circuit is a dc/SFQ converter [83, 84][1]. Figures 4.3(a, b) show a detailed circuit diagram of the converter and a top-down optical micrograph of the fabricated device, respectively. This particular circuit is heavily inspired by [168]. The parameters for the various elements of this circuit, as simulated, are listed in Table 4.1.

Figure 4.3(c) shows the simulated output of the converter circuit (green) for a given input tone (purple); here, a single SFQ pulse is output for each clock cycle of the trigger tone with interpulse timing equal to $2\pi/\omega_d$. In the setup used for these experiments, however, we are not able to directly measure the time-trace of the converter circuit output as it is plotted here. Instead, in the lab we measure a time-average of this voltage output, which for one cycle of the trigger tone is $(1/T)\int \Phi_0\delta(t)dt = \Phi_0/T$ where $T = 2\pi/\omega_d$, giving the familiar Shapiro step voltage relation [169]

$$\Delta V = (\Phi_0/2\pi)\omega_d. \tag{4.10}$$

[1]The author also acknowledges the RSFQ cell library maintained by D. Zinoviev and hosted by The State University of New York for being a useful resource in finding these informative journal articles [168].

Figure 4.3(d) shows a simulated Shapiro step induced by the presence of a trigger tone at frequency $\omega_d/2\pi = 5$ GHz and power -60 dBm while the presence of no trigger tone shows instead no step before the circuit jumps out to the pure voltage state. This plot represents the most basic fashion in which we can tell both in simulation (and in the lab) whether or not our dc/SFQ converter circuit is behaving correctly.

Another way in which we were able to check if our circuit made good sense and was being properly simulated was to change the magnetic hysteresis parameter of the switching SQUID

$$\beta_L = \frac{2\pi}{\Phi_0} I_{sw} L_{sw} \tag{4.11}$$

and check the bias margins – as in, check how "large" the operable region is for the circuit in terms of I_b as a function of β_L. Since we were interested in a circuit with critical current density on the order of ~ 1 kA/cm^2, the knob we turned in simulation was L_{sw}. In Figs. 4.3(e, f), we show simulated IV curves for the converter circuit both without and with an applied trigger tone at frequency $\omega_d/2\pi = 5$ GHz and power -60 dBm. In this configuration, we see in simulation the expected Shapiro step [Eq. (4.10)] of height $\Delta V \approx 10$ μV. However, we also want to ensure that we are able to choose a bias point which will both a) allow the converter to stay in the supercurrent state while no trigger tone is applied (and thus dissipate zero power while doing nothing) and b) provide for the generation of single phase slips (SFQ pulses) for each clock cycle of an applied trigger tone. Hence, while Figs. 4.3(e, f) show that there indeed is a region in which Shapiro steps are formed, Fig. 4.3(g) shows the true operable region: the region in which (not) applying a trigger tone results in (staying in the supercurrent branch) the output of single SFQ pulses. The results of our simulation show that the operable region really starts becoming wide at $L_{sw} \gtrsim 23$ pH, implying $\beta_L \gtrsim 2.8$, which is compatible with previous documentations of this circuit [83, 84, 168] which suggest $2 < \beta_L < 6$.

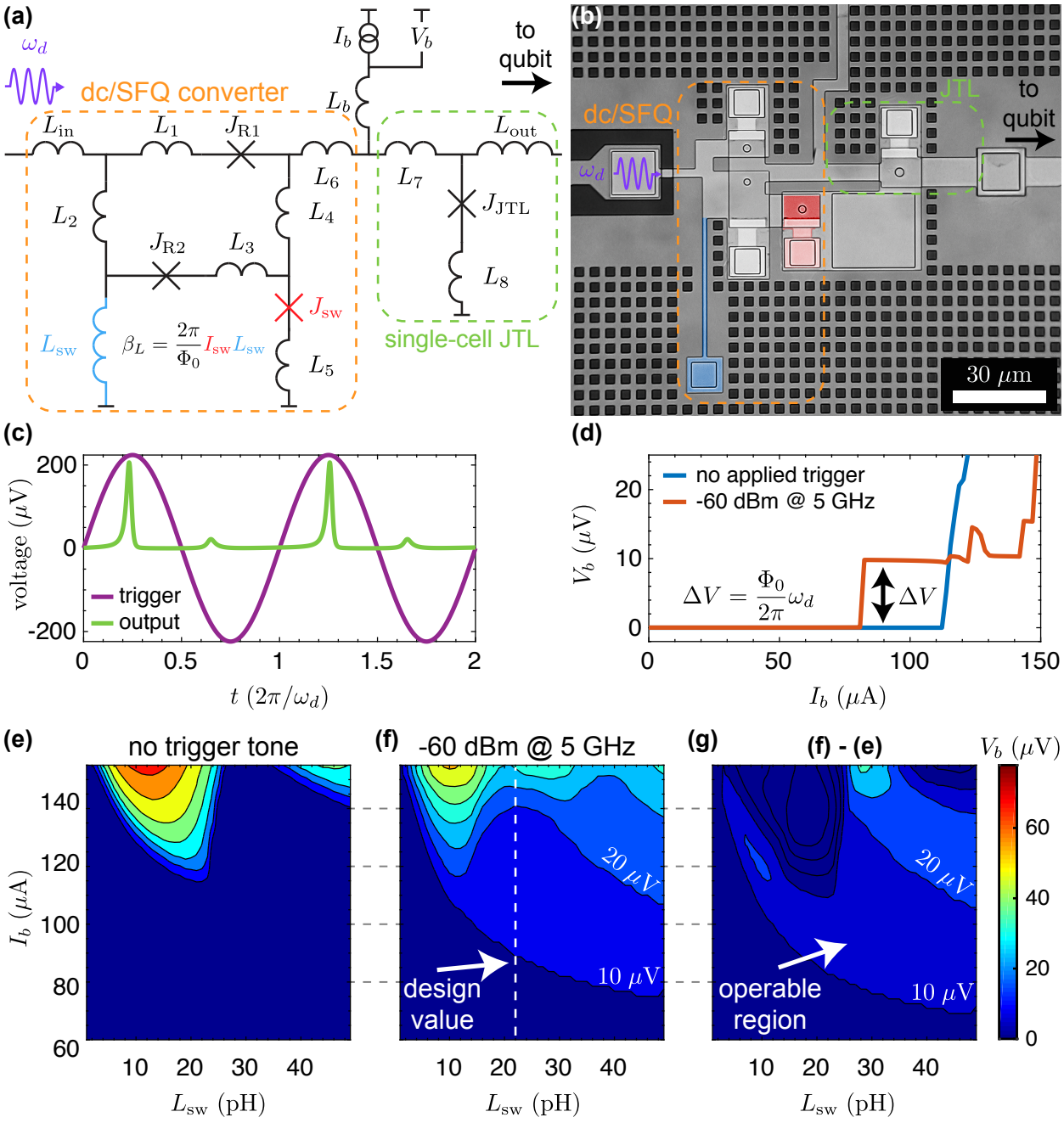

Figure 4.3: dc/SFQ converter WRSpice simulation results **(a)** Circuit diagram used for the dc/SFQ converter described in this work. Each JJ is overdamped by an explicit shunt resistor (not drawn). Circuit parameters are listed in Table 4.1. **(b)** Optical micrograph of the dc/SFQ converter circuit used in this work. **(c)** Simulated time response of a properly functioning converter circuit; for each cycle of ω_d, a single SFQ pulse is output. **(d)** Simulated IV characteristic curve of the converter circuit; a Shapiro step of height $\Delta V = (\Phi_0/2\pi)\omega_d$ implies one SFQ pulse per cycle of ω_d. **(e)** Simulated IV curve as a function of L_{sw} with no trigger tone. **(f)** Simulated IV curve as a function of L_{sw} with $\omega_d/2\pi = 5$ GHz and power -60 dBm. **(g)** Difference between **(e)** and **(f)**, highlighting the 10 μV Shapiro step.

Inductors		Junctions	
inductor	value (pH)	junction	area (μm^2)
L_b	0.08	J_{R1}	4
L_{in}	3.35	J_{R2}	3
L_{sw}	22.0	J_{sw}	4
L_{out}	2.11	J_{JTL}	5.5
L_1	1.29	**Resistors**	
L_2	1.29	resistor	resistance (Ω)
L_3	0.69	R_{R1}	5.5
L_4	0.21	R_{R2}	3
L_5	0.18	R_{sw}	3.7
L_6	1.14	R_{JTL}	3
L_7	1.74		
L_8	0.13		

Table 4.1: List of parameters for the circuit elements comprising the dc/SFQ converter in Fig. 4.3(a).

4.2.3 Hybrid Device Overview

The experiment involves a transmon qubit cofabricated with an SFQ driver circuit on a high-resistivity Si(100) substrate. In Fig. 4.4(a) we show a micrograph of the completed circuit, and in Fig. 4.4(b) we present the circuit diagram. The transmon qubit [blue in Fig. 4.4(a, b)] includes a flux-tunable compound JJ with asymmetry of approximately 2:1 [or $d = 1/3$ in Eq. (2.19)] [170]. For the experiments described here, the qubit is tuned to its upper flux-insensitive sweet spot with fundamental transition frequency of $\omega_{10}/2\pi = 4.958$ GHz; the qubit anharmonicity is $\alpha/2\pi \approx -220$ MHz. The qubit is independently addressable with either shaped microwave tones or SFQ pulses and is measured via standard heterodyne detection through a $\lambda/4$ coplanar waveguide (CPW) resonator (yellow) with a resonance frequency of 6.15 GHz, decay rate $\kappa = (500\,\text{ns})^{-1}$, and resonator-qubit coupling of $g/2\pi \sim 100$ MHz. The SFQ driver circuit [green in Fig. 4.4(a, b)] is based on a standard dc/SFQ converter [83, 84] and is detailed previously in Sec. 4.2.2. The output of the driver is coupled via a single-cell Josephson transmission line (JTL) to a short superconducting microstrip with characteristic impedance $\sim 1\ \Omega$; the microstrip is

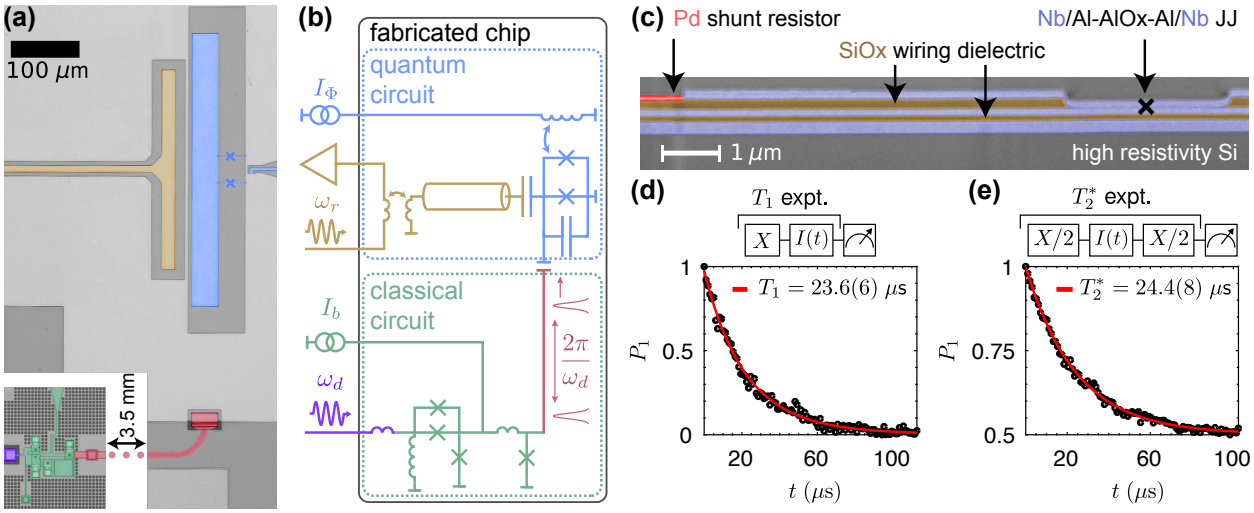

Figure 4.4: Overview of the quantum-classical hybrid circuit. **(a)** False-color optical micrograph of the SFQ driver circuit (green) with capacitive coupling (red) to the superconducting transmon qubit (blue). The qubit is coupled to the voltage antinode of a λ/4 coplanar waveguide resonator (yellow) and is biased by a dc flux line (blue). The SFQ driver is triggered by a microwave tone delivered via a $Z = 50\ \Omega$ CPW transmission line (purple). The distance between the SFQ driver and qubit is approximately 3.5 mm. **(b)** Circuit diagram for the device of **(a)**. Each JJ in the classical circuit is shunted by a thin-film Pd resistor (not shown). **(c)** False-color cross-sectional SEM micrograph showing layer stack in the vicinity of a Nb/Al-AlO_x-Al/Nb JJ of the SFQ driver. The Nb wiring layers (blue) are separated by SiO_x dielectric layers (brown); the driver junctions are formed in vias in the dielectric layer separating the second and third Nb metal layers. Pd resistors (red) shunt the junctions of the driver circuit. **(d-e)** Conventional microwave-based characterization of qubit energy relaxation **(d)** and dephasing **(e)** with extracted characteristic times $T_1 = 23.6(6)$ μs and $T_2^* = 24.4(8)$ μs, respectively.

terminated in a coupling capacitance C_c [red in Fig. 4.4(a, b)], which delivers SFQ pulses to the qubit. The SFQ driver circuit is biased with a dc current I_b (green) and an external microwave trigger tone at frequency ω_d (purple); a properly biased circuit will output a single SFQ pulse for each cycle of the trigger waveform. We summarize the key fabrication steps used to realize the hybrid circuit below and describe the methods used to find an operating point after.

4.2.4 Hybrid Device Fabrication

The qubit capacitor, CPW readout resonator, and surrounding microwave ground plane are realized in a 180 nm-thick Nb film grown by dc magnetron sputtering. The dielectric materials required for the multilayer stack are deposited using plasma enhanced chemical vapor deposition (PECVD). The SFQ driver circuit incorporates three superconducting Nb layers, two insulating SiO_x layers, one normal metal Pd layer, and four Nb/Al-AlO_x-Al/Nb JJs with critical current density $J_c \sim 1$ kA/cm^2 and areas $\{3, 4, 4, 5.5\}$ μm^2. The SFQ driver JJs are shunted by thin-film Pd resistors formed by electron-beam evaporation and liftoff. In areas where good metallic contact is required between wiring layers, an *in situ* Ar ion mill cleaning step is used to remove native NbO_x prior to metal deposition. Figure 4.4(c) shows a cross-sectional scanning electron microscope (SEM) image of the layer stack in the vicinity of the SFQ driver obtained following a focused ion beam mill through the circuit. Here, the Nb layers are false-colored in blue, the SiO_x dielectric layers are colored brown, and the Pd shunt resistor is shown in red. A black $\times$ marks the location of a Nb/Al-AlO_x-Al/Nb junction interface.

Throughout fabrication of the multilayer SFQ driver, a blanket layer of SiO_x is used to protect the areas where the readout resonator and qubit capacitor and junctions will be formed. Following completion of the SFQ driver circuit, this dielectric protection layer is completely removed [171] and the quantum circuit is patterned and etched. Formation of the qubit junctions is the final step of the process. The transmon junction electrodes are defined using electron-beam lithography with a standard MMA/PMMA resist bilayer. The qubit junctions are grown via double-angle Al evaporation with a controlled *in situ* oxidation between the two deposition steps. A detailed and sequential list of steps to fabricate the device follows below with a summary of each layer in Table 4.2

1. **Layer M1:** A bare intrinsic Si wafer is coated with a film of Nb after stripping the native SiO_x with hydrofluoric (HF) acid. Here and below, sputter conditions are tuned

Layer ID	Material	Thickness (nm)	Surface Pre-treatment	Deposition Method	Patterning	Etch Chemistry	Function
M1	Nb	180	hydrofluoric acid	dc sputtered	i-line	Cl_2/BCl_3	ground plane resonators capacitors
D1	SiO_x	130	–	PECVD	i-line	CHF_3	SFQ circuit wiring ground vias
M2	Nb	90	*in situ* ion mill	dc sputtered	i-line	SF_6	inductors SFQ JJ base layer
D2	SiO_x	180	–	PECVD	i-line	CHF_3	junction definition shunt resistor vias
M3	Nb Al-AlO_x-Al	100	*in situ* ion mill	dc sputtered w/*in situ* oxidation	i-line	SF_6 TMAH	SFQ bias wiring SFQ JJ counterelectrodes CPW crossovers
R	Ti/Pd	23	*in situ* ion mill	e-beam evaporated	i-line	–	shunt resistors
QP	Ti/Cu/Pd	93	*in situ* ion mill	e-beam evaporated	i-line	– quasiparticle traps	
QB	Al-AlO_x-Al	100	*in situ* ion mill	e-beam evaporated (double-angle)	e-writing (Dolan Bridge)	–	qubit JJs

Table 4.2: Layer stack description of the hybrid quantum-classical circuit.

to yield films with slight compressive stress [145]; the deposition rate is 45 nm/min. This layer is patterned with an i-line step-and-repeat (stepper) lithography tool and etched with a Cl_2/BCl_3-based inductively coupled plasma (ICP). During this and the following six steps, the area of the die that will ultimately support the readout resonator and qubit is left unpatterned and unetched.

2. **Layer D1:** A plasma-enhanced chemical vapor deposition (PECVD) process is used to grow a conformal layer of SiO_x. This layer is patterned with an i-line stepper and etched with a CHF_3-based reactive ion etch (RIE) plasma. The RIE power and pressure are optimized to transfer a 45° slope into the dielectric sidewalls in order to promote step coverage of subsequent layers [see Fig. 4.4(c)].

3. **Layer M2:** The bottom Nb electrode for the SFQ JJs is sputtered. This layer is patterned with an i-line stepper and etched with an SF_6-based RIE plasma.

4. **Layer D2:** Another SiO_x layer is grown by PECVD. This layer is patterned in the same manner as in step 2. At this step, particular care is taken to eliminate solvent or other organic residues from the dielectric vias, as these vias will define the SFQ JJs.

5. **Layer M3:** The SFQ JJs and bias wiring are formed in the following process:

   (a) The wafer is transferred into the sputter system load-lock chamber and the chamber is pumped down for ~ 1 hour.

   (b) While the load lock is pumping out, the primary vacuum chamber is "seeded" with pure O_2 using similar conditions to the actual junction oxidation. We find that this step improves the reproducibility of the junction specific resistance by ensuring as similar a chamber chemistry as possible from run to run.

   (c) The wafer is transferred into the primary vacuum chamber and the system is allowed to pump down to base pressure (about 5×10^{-8} Torr).

   (d) An *in situ* ion mill is used to remove the NbO_x from the M2 electrode layer.

(e) An Al seed layer of thickness ~ 8 nm is sputtered.

(f) The barrier oxide is grown. The AlO_x barrier layer is seeded by flowing O_2 at low pressure (~ 1 mTorr) for 2 minutes. The chamber is then valved off from the pumps and the O_2 pressure is quickly ramped to the target value (typically ~ 100 mTorr), where it remains for the duration of the oxide growth (typically about 10 minutes).

(g) The growth chamber is pumped back to vacuum. An Al cap layer of ~ 6 nm thickness is sputtered, followed by the 90 nm Nb junction counterelectrode.

This layer is patterned with an i-line stepper. The Nb is removed with an SF_6-based RIE plasma while the Al-AlO_x-Al is removed with a TMAH-based photoresist developer wet etch.

6. At this point, it is possible to probe the 4-wire resistances of witness junctions co-fabricated on the die with the SFQ/qubit circuit. The expected critical currents are extracted using the Ambegaokar-Baratoff relation [146].

7. The SiO_x layer protecting the area of the qubit and readout resonator is now patterned and etched as in step 2.

8. The readout resonators and qubit capacitor are defined in the M1 Nb layer using pattern and etch processes as in step 1.

9. **Layer R:** A negative photoresist is patterned with an i-line stepper to define the shunt resistors. The resistors are formed by electron-beam evaporation of Pd following an *in situ* ion mill and deposition of a thin (~3 nm) Ti adhesion layer. Liftoff is performed in acetone at room temperature over several hours with slight manual agitation of the wafer.

10. **Layer QP (optional):** A negative photoresist is patterned with an i-line stepper to define the normal metal QP traps. The traps are formed by electron-beam evaporation

of Cu following an *in situ* ion mill and deposition of a thin (~3 nm) Ti adhesion layer. Liftoff is performed in acetone at room temperature over several hours with slight manual agitation of the wafer.

11. **Layer QB:** The qubit junctions are defined using a Dolan bridge process [53] involving an MMA/PMMA stack patterned with a 100 keV electron-beam writer. The Al-AlO_x-Al stack is shadow evaporated in a high vacuum electron beam evaporation tool following an *in situ* ion mill to ensure good metallic contact to the base layer (M1).

4.2.5 Experimental Setup

The device is wirebonded in an SMA-connectorized Al package and loaded on the experimental stage of a dilution refrigerator. Low-bandwidth coaxial cabling is used for the current bias I_b of the SFQ driver and the flux bias I_Φ of the transmon qubit. The measurement setup is shown in Fig. 4.6. The microwave tones used to read out the qubit, perform microwave control of the qubit, and trigger the SFQ pulse driver are all generated through single-sideband modulation of a local oscillator (LO) carrier wave with shaped intermediate frequency (IF) signals. Arbitrary waveform generators (AWG) with an output rate of 1 GS/s and 14-bit resolution generate the IF tones and are directly connected to the in-phase (I) and quadrature (Q) ports of an IQ mixer. The shaped microwave pulses for qubit control and readout are passed through digital variable attenuators before merging on a 3 dB combiner and entering the cryostat. The readout and microwave control tones pass through multiple stages of attenuation and filtering at the 4 K and mK stages of the dilution refrigerator prior to reaching the device. After interacting with the device, the qubit readout tone passes through several stages of isolation and filtering prior to amplification at 4 K using a high electron mobility transistor (HEMT) amplifier. The readout tone is further amplified at room temperature. The same LO used to generate the readout signal is used for heterodyne detection of the qubit state. The downconverted IF tones from qubit measurement are sampled at 500 MS/s with 8-bit resolution and demodulated and

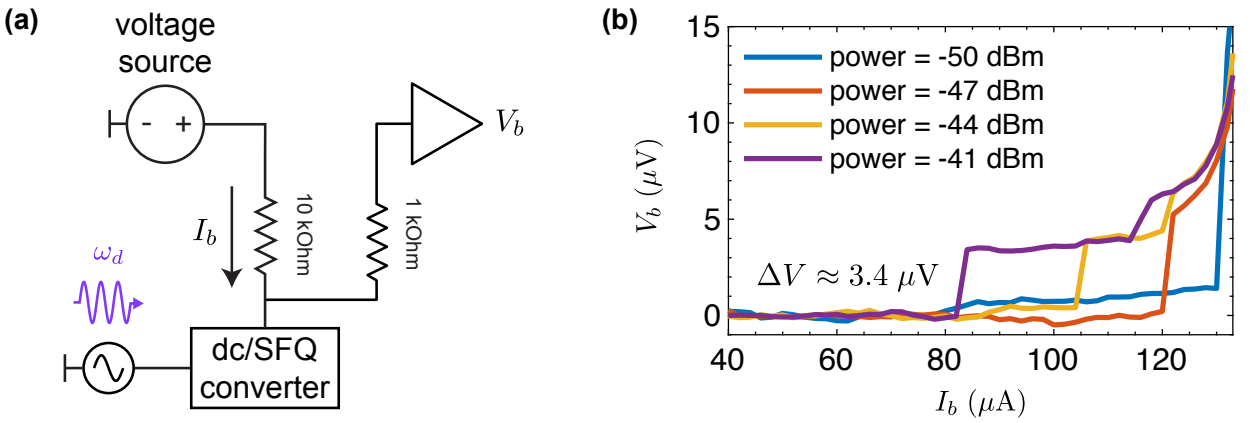

Figure 4.5: Shapiro step data for the dc/SFQ converter. **(a)** Basic wiring diagram for this experiment. A trigger tone at frequency ω_d irradiates the dc/SFQ converter input and a dc bias current I_b is generated by a room-temperature low-noise voltage source in series with a resistor-capacitor filter network (capacitors not drawn; the knee frequency was approx. $1/RC \sim 10$ kHz); the voltage response of the converter V_b is measured using a similarly filtered network and a room-temperature low-noise amplifier. This diagram is meant only to show the essential components needed for this experiment; the full wiring diagram is shown in Fig. 4.6. **(b)** Characteristic IV curves for the dc/SFQ converter where $\omega_d/2\pi = 1.65$ GHz. Here, we can see the Shapiro step of height $\Delta V \approx 3.4$ μV for appropriate applied trigger power.

analyzed in software. For all of the work presented here, we employ so-called "bright-state" readout of the qubit [114]. The microwave tone used to trigger the SFQ pulse driver is conditioned with a low-pass filter that provides strong rejection at the qubit fundamental frequency ω_{10}. The trigger tone passes through multiple stages of attenuation and filtering at the 4 K and mK stages of the cryostat before reaching the device. Both the qubit flux bias and the dc bias current for the SFQ pulse driver are generated by isolated low-noise voltage sources at room temperature. These signals are conditioned by multiple stages of filtering at the 4 K and mK stages of the cryostat.

Prior to investigation of SFQ-based gates, the transmon qubit and SFQ pulse driver are characterized separately. The qubit is flux tuned to its upper sweet spot to reduce susceptibility to flux noise [170]. Microwave excitation pulses are coupled to the qubit via off-resonant drive through the readout resonator. Standard inversion recovery and Ramsey sequences are used to determine the qubit energy relaxation and dephasing times

T_1 and T_2^*, respectively; data from these experiments are shown in Fig. 4.4(d, e). We find relaxation times in excess of 20 μs. These times are compatible with relaxation times that are achieved in planar transmon qubits fabricated using a single double-angle evaporation step that avoids lossy dielectrics [43]. Meanwhile, bringup of the SFQ driver circuit involves measurement of the device IV-characteristic curves. In the absence of applied microwave drive at the trigger input, the critical current I_c of the device is around 130 μA. Proper operation of the SFQ driver is determined by biasing I_b near the critical current and applying microwave drive to the trigger input. For appropriate drive amplitude, the application of an oscillatory tone at frequency ω_d induces a Shapiro step in the driver IV curve [Eq. (4.10)]. Figure 4.5 shows such data acquired for the circuit used in this work.

While the data presented here is taken on the mK stage of a DR, we did find it useful to pre-screen these devices. A typical workflow is as follows:

- Use a room-temperature four-wire probe station to measure the room-temperature characteristics of witness JJs and resistors. Using these values and [59, 60, 146], verify that the damping parameter is expected to be $\beta_C < 1$.

- Wirebond the sample to a custom PCB outfitted with bias resistors which emulate the dc bias circuitry in Fig. 4.6 and submerge it into liquid He. IV curves for both the unshunted witness Nb/Al-AlOx/Nb JJs as well as for the dc/SFQ converter circuit are obtained. An rf tone is used at this point to induce Shapiro steps [169], ensuring proper circuit operation.

- Wirebond the sample to an Al package and mount in the cold stage of an adiabatic demagnetization refrigerator using dc and rf wiring and filtering substantially similar to that of Fig. 4.6. Once cold, verify that the dc/SFQ converter circuit works as intended at mK. Next, perform simple measurements with a vector network analyzer and dc sources to learn if the qubit fabrication was successful (e.g., look for a dispersive

shift in the lower-power regime of the qubit-cavity system and flux-tune the qubit to pull the dressed-cavity).

- If all previous steps pass, load the device into the cold stage of a DR and perform detailed measurements, the results of which are presented here.

4.3 SFQ Pulses for Qubit Control

Following establishment of coarse operating points for the qubit and SFQ driver, the qubit itself is used to fine-tune SFQ-based gate operations. We apply a microwave tone at a subharmonic of the qubit frequency $\omega_d = \omega_{10}/n$, where $n \in \{2, 3, 4, \dots\}$, to the driver trigger input for varying time and sweep the converter bias $I_b \lesssim I_c$ while monitoring the state of the qubit [Fig. 4.7(a)]. In this device, subharmonic drive is essential in order to circumvent direct microwave crosstalk from the trigger line to the qubit. For a broad range of driver bias current, the qubit Rabi frequency is approximately independent of driver bias. Similarly, the Rabi frequency is independent of microwave trigger drive power over a broad range (not shown); this is expected, as the SFQ driver acts as a threshold comparator generating a single SFQ pulse per period of the trigger waveform. From this measurement, we select the optimal current bias and microwave trigger power to produce clear qubit Rabi oscillations.

At this point, we use SFQ pulse trains to perform conventional qubit experiments. In Fig. 4.7(b) we show the results of an SFQ-based Rabi experiment where the SFQ pulse frequency is swept over a narrow interval in the vicinity of $\omega_{10}/3$ to produce the familiar "chevron" interference pattern. From the data we determine the length of SFQ-based $\pi/2$ and π gates, which we denote as $X_{SFQ}/2$ and X_{SFQ}, respectively. For $n = 3$, the duration of the $X_{SFQ}/2$ (X_{SFQ}) gate is 14 (28) ns, corresponding to 23 (46) discrete SFQ pulses. From the measured Rabi frequency and Eq. (4.1) we determine the coupling capacitance $C_c = 400$ aF between the driver and qubit circuits. Once the $X_{SFQ}/2$ gate is defined, we perform a Ramsey

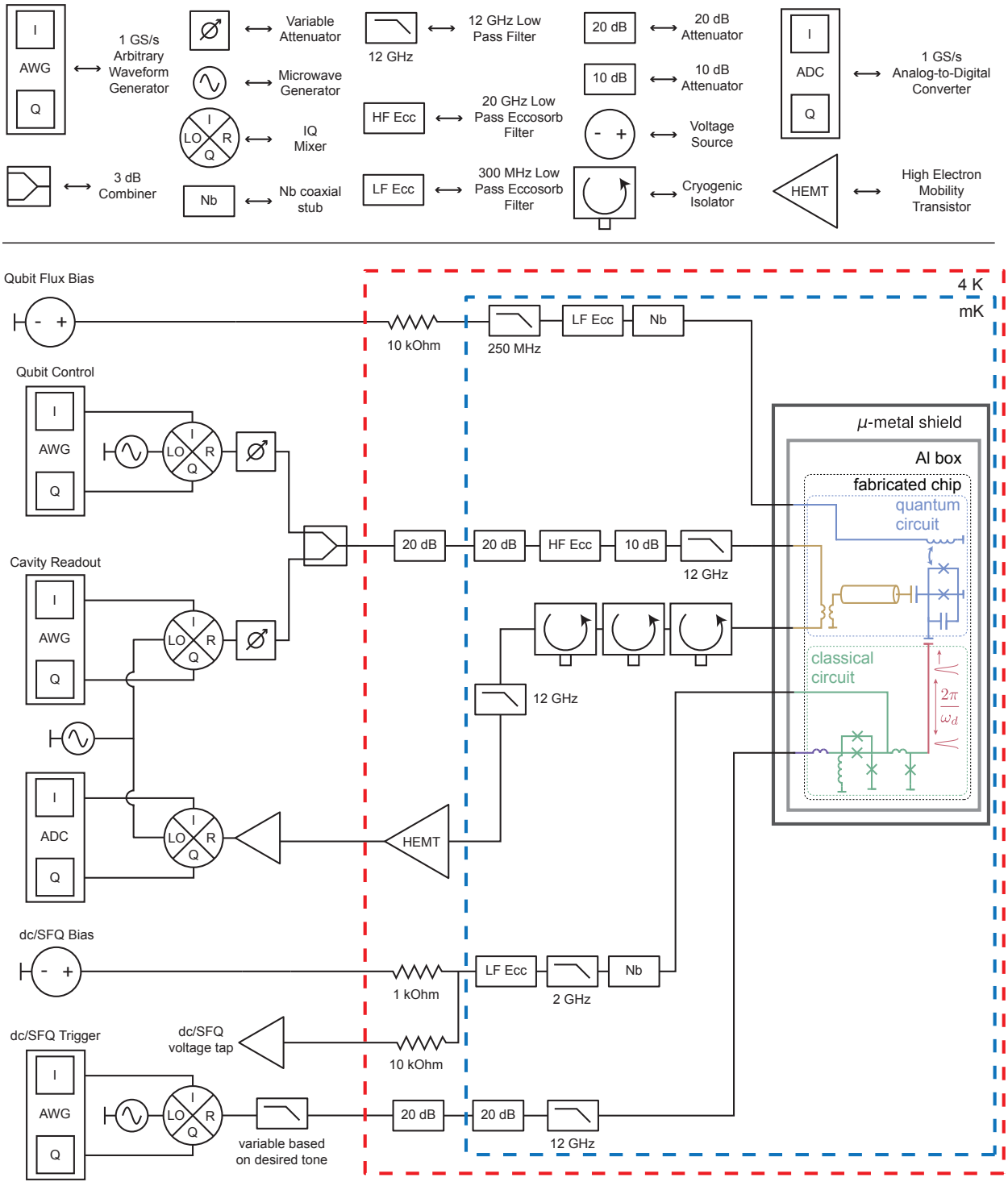

Figure 4.6: Experimental wiring diagram. Component symbols are defined in the panel above the wiring diagram. All components within the μ-metal shield (grey box) were made of either non-ferric or certified non-magnetic materials.

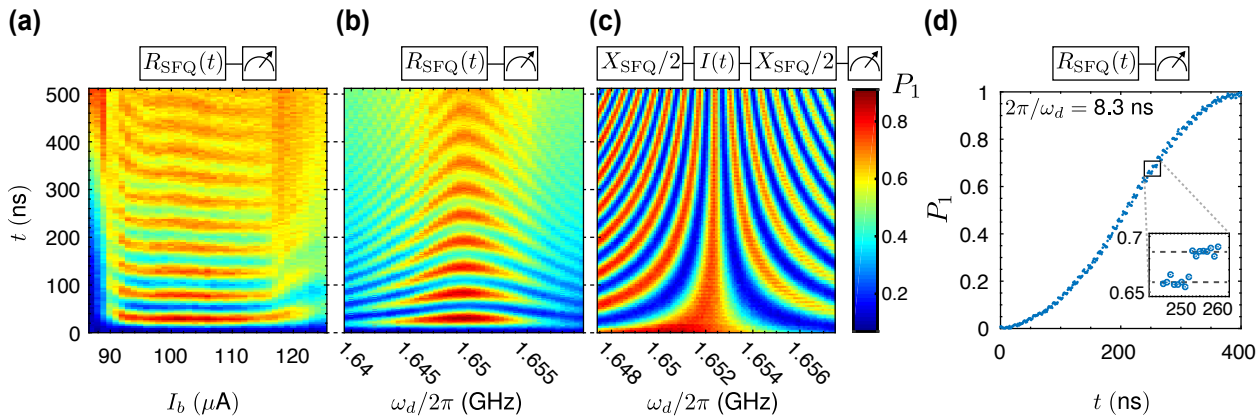

Figure 4.7: Basic qubit operations driven by SFQ pulses. **(a)** SFQ-based Rabi oscillations as a function of bias current I_b to the SFQ driver circuit. Here, $\omega_d = \omega_{10}/3 \approx 1.65$ GHz. **(b)** Rabi chevron experiment and **(c)** Ramsey fringe experiment where the SFQ pulse frequency ω_d is varied slightly in the vicinity of $\omega_{10}/3$. **(d)** (main) Time trace of a single SFQ-based Rabi flop obtained with a pulse rate $\omega_{10}/41 = 120.90$ MHz. (inset) A zoom-in on discrete steps in $P_1(t)$ occurring every 8.3 ns, the SFQ pulse-to-pulse timing interval.

interferometry experiment [Fig. 4.7(c)]; we obtain familiar interference fringes oscillating with a frequency corresponding to three times the detuning of the SFQ pulse train from $\omega_{10}/3$. Another experiment we have performed is a wide-range sweep of the trigger tone frequency ω_d. In Fig. 4.8, we sweep ω_d from $\omega_{10}/10 \rightarrow \omega_{10}/4$, while monitoring the state of the qubit; at the various subharmonics of ω_{10} that we pass, we see indications of coherent oscillations.

By triggering the SFQ driver at a much lower frequency and delivering a dilute SFQ pulse train to the qubit, we can map out the terraced trajectory of the qubit state vector on the Bloch sphere evoked by the name of the DANTE pulse sequence. In Fig. 4.7(d) we show data from a qubit Rabi flop obtained with an SFQ pulse train triggered at a deep subharmonic $\omega_d = \omega_{10}/41$. The discrete steps induced by the individual SFQ pulses are evident and emphasized in the figure inset.

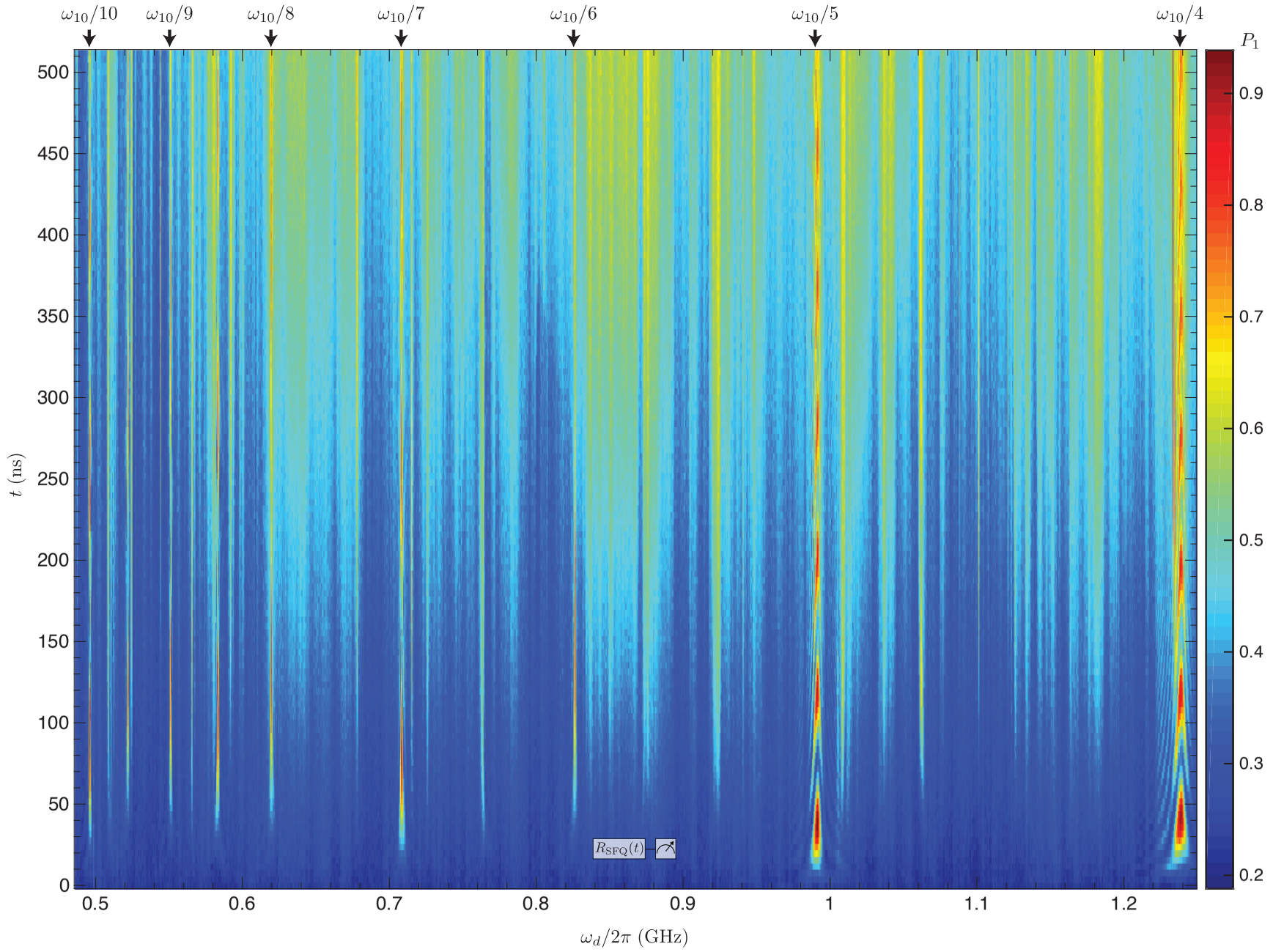

Figure 4.8: Rabi experiment as function of time and frequency. Here, the drive frequency is swept such that several of the qubit subharmonic frequencies are excited.

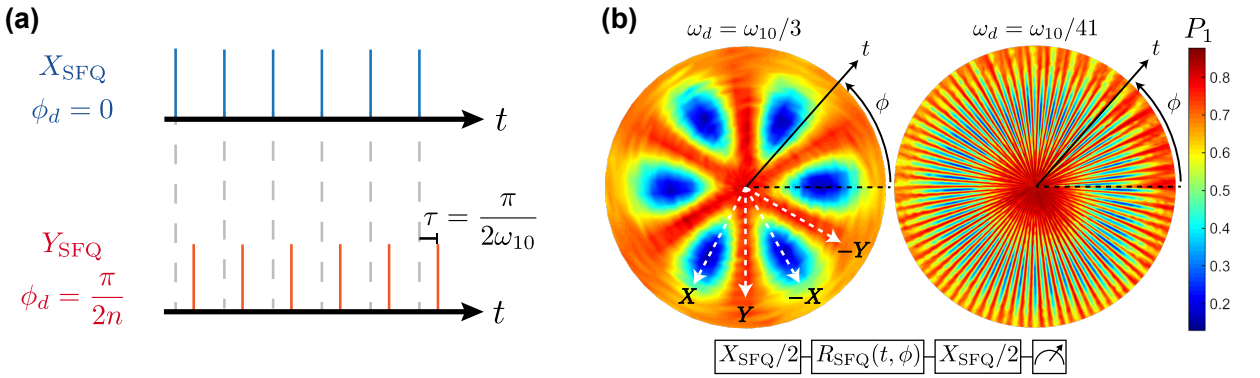

Figure 4.9: **(a)** Illustration depicting SFQ pulse sequences for orthogonal qubit control. The resonant X-sequence establishes a timing reference; a change in the relative timing of a second resonant sequence can be used to access different orientations of the qubit control vector in the equatorial plane of the Bloch sphere. A Y_{SFQ}-sequence is shifted in time by one quarter of the qubit oscillation period with respect to the X_{SFQ}-sequence. **(b)** Generalized Rabi scans for resonant SFQ pulse trains triggered at subharmonic frequency $\omega_{10}/3$ (left) and $\omega_{10}/41$ (right), respectively. The pulse sequence is shown below the figure. The radial coordinate is swept by incrementing the duration of $R_{\mathrm{SFQ}}(t, \phi)$ from 0 ns to 60 ns (left) or 660 ns (right), while the polar angle corresponds to the phase ϕ of the trigger waveform used to generate the pulse train. The length and phase of each $X_{\mathrm{SFQ}}/2$ pulse are fixed. Adjustment of the phase ϕ of the trigger waveform by $\pi/2n$ provides access to an orthogonal control axis; here, n is the subharmonic drive factor. The $2n$-fold symmetry of the plots is explained by the fact that subharmonic drive automatically yields an n-fold increase in the number of (time-shifted) resonant sequences that access the same control vector on the Bloch sphere, and by the fact that our sequence doesn't distinguish between positive and negative rotations (yielding an additional doubling of the symmetry of the plot). On the left panel, we label rays corresponding to trigger waveform phases that yield $\pm X_{\mathrm{SFQ}}, \pm Y_{\mathrm{SFQ}}$ rotations.

4.3.1 Orthogonal Axis Control with SFQ Pulses

Any complete qubit control scheme requires rotations about orthogonal axes. In the case of conventional microwave-based qubit control, the direction of the rotation is set by the phase of the pulse. For SFQ-based control, the relative timing of two resonant SFQ pulse trains determines the directions of the corresponding control vectors in the equatorial plane of the Bloch sphere. We first consider the case of resonant drive at the qubit fundamental frequency. We arbitrarily choose the relative timing of one sequence to correspond to the X_{SFQ}-rotation. For a second resonant pulse sequence that is shifted in time by τ with

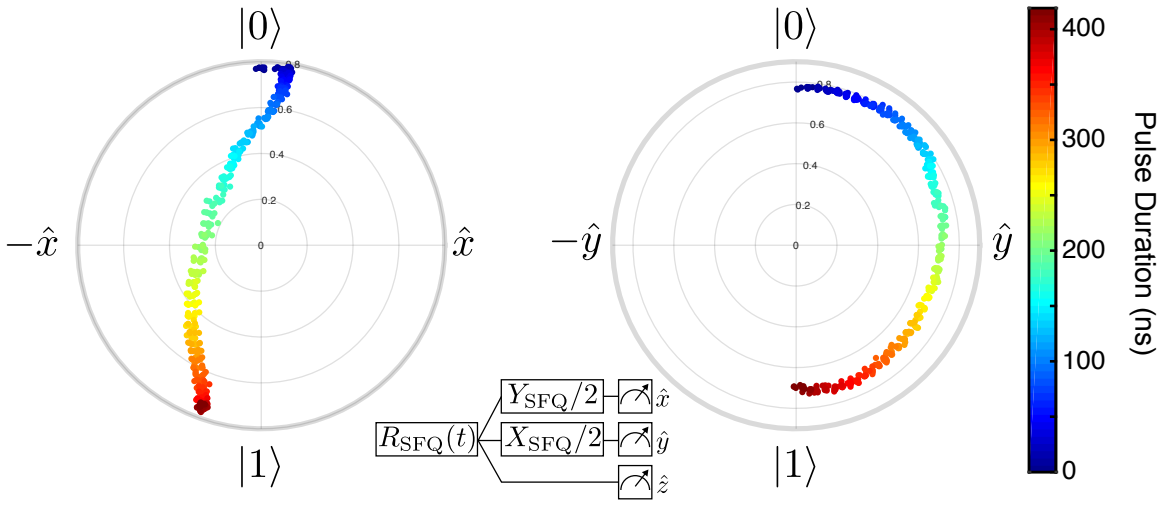

Figure 4.10: Trajectory of an X_{SFQ} pulse driven at $\omega_{10}/41$. Here, each rotation length is repeated three times followed by a different axis projection to perform the three measurements required to determine its coordinates on the Bloch sphere.

respect to the first, the qubit sees a control vector that is rotated by an angle $\phi = \omega_{10}\tau$ in the equatorial plane. For example, the pulse train for the Y_{SFQ}-gate is shifted by an amount $\tau = \pi/2\omega_{10}$ (one quarter of an oscillation period) with respect to that of the X_{SFQ}-gate; see Fig. 4.9(a). In practice, the relative timing between pulse trains τ is controlled by adjusting the phase of the SFQ trigger waveform using standard heterodyne techniques.

For SFQ drive at a subharmonic of the qubit frequency, timing shifts between sequences induce a faster rotation of the angle of the control vector by $\phi_n = n\omega_{10}\tau$, where n is the subharmonic drive factor. Figures 4.9(b, c) display generalized 2D Rabi data for qubits driven with SFQ pulse trains at $\omega_{10}/3$ and $\omega_{10}/41$, respectively. A Rabi pulse with varying duration and phase is inserted between two SFQ-based $\pi/2$ gates whose timing defines the X-direction. In these plots, the duration t of the control sequence is encoded in the radial direction, the polar coordinate is given by the phase of the SFQ trigger tone at frequency $\omega_d = \omega_{10}/n$, and the measured qubit population is plotted in false color. We see clear $2n$-fold symmetry in the scans: pulse trains shifted by $2\pi/n\omega_{10}$ are equivalent, while the additional factor of 2 comes from the fact that the sequence does not distinguish between positive and negative rotations. In the plots, polar angles that yield high-contrast Rabi

oscillations correspond to control in the $\pm$X directions, while polar angles that yield no oscillation correspond to orthogonal control in the $\pm Y_{SFQ}$ directions. We have used this style of orthogonal control to also perform tomography on the trajectory of an X_{SFQ} pulse driven at $\omega_{10}/41$. The data from this scan is shown in Fig. 4.10, where the colorscale is the pulse duration and the two plots show the full three-coordinate trajectory of the pulse.

4.3.2 Randomized Benchmarking of SFQ Gates

Gate Length ($\pi/2$ gates)	Gate Length (SFQ pulses)	Gate Sequences		
0	0	I		
1	23	$\pm$X/2		
		$\pm$Y/2		
2	46	X		
		Y		
		X/2,	$\pm$Y/2	
		$-$X/2,	$\pm$Y/2	
		Y/2,	$\pm$X/2	
		$-$Y/2,	$\pm$X/2	
3	69	X,	$\pm$Y/2	
		Y,	$\pm$X/2	
		$-$X/2,	$\pm$Y/2,	X/2
		$\pm$X/2,	Y/2,	$\pm$X/2
4	92	X,	Y	

Table 4.3: List of the 24 composite single-qubit Cliffords used in this work and their respective lengths in number of SFQ pulses.

With orthogonal control now established, it is possible to generate the full single-qubit Clifford set. Here, we have used interleaved RB [165, 172, 173] to evaluate the fidelity of SFQ-based Clifford gates. Here, we use the single-qubit composite Clifford set, which constitutes a complete group. A way one might think of this gate group is as an axes rotation set; when looking at the Bloch sphere, it is rotationally symmetric, and thus the $+x$-axis can be arbitrarily chosen to lie along one of six directions. Once the $+x$-axis is chosen, another rotation shows a symmetry in which there are four options for the $+z$-axis.

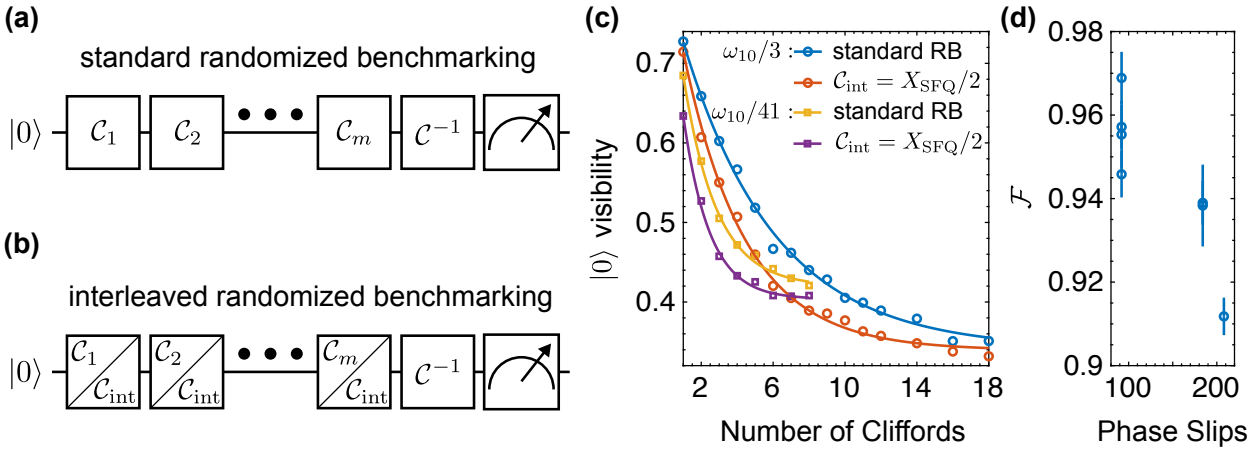

Figure 4.11: Randomized benchmarking (RB) of SFQ-based gates. **(a)** Protocol for randomized benchmarking of a quantum gate set [172, 173]. Here, the qubit initial state is assumed to be $|0\rangle$ and is operated on by m random Cliffords $\mathcal{C}_i$. The final Clifford $\mathcal{C}^{-1}$ is chosen such that it will invert the entire prior sequence and return the qubit to $|0\rangle$ in the absence of errors. **(b)** Protocol for benchmarking of a single gate $\mathcal{C}_{int}$ within the Clifford set, so-called interleaved randomized benchmarking [165]. Operationally, it is similar to the procedure in **(a)** except that the gate of interest is interleaved between the random Cliffords $\mathcal{C}_i$. **(c)** Depolarizing curves for all Cliffords and for the interleaved gate sequence designed to probe the $\mathcal{C}_{int} = X_{SFQ}/2$ gate as a function of the number of Clifford operations. The (blue, orange) traces correspond to SFQ sequences with pulse rate $\omega_d = \omega_{10}/3$, while the (yellow, purple) traces correspond to pulse rate $\omega_d = \omega_{10}/41$. A full list of gate fidelities is given in Table 4.4. **(d)** Gate fidelity $\mathcal{F}$ for pulse rate $\omega_d = \omega_{10}/3$ as a function of the number of phase slips in the driver circuit. Here, we see a general trend that a gate requiring more phase slips results in a lower gate fidelity. This can be understood by the idea that quasiparticles generated in the driving circuit for every phase slip are poisoning the qubit. This is discussed in detail in the main text.

Hence there are $6 \times 4 = 24$ single-qubit Clifford operations, which are outlined in Table 4.3.

The experiment is run as follows [165]:

1. Choose a value of m – the maximum practical value of this will depend on how quickly the system depolarizes

2. Select m random Cliffords from the list in Table 4.3

3. Starting at $|0\rangle$, apply the gate sequence

$$\mathcal{C}_{tot} = \left[\prod_{i=1}^{m} \mathcal{C}_i\right] \mathcal{C}^{-1}, \tag{4.12}$$

where $\mathcal{C}_i$ is a random Clifford and the final gate $\mathcal{C}^{-1}$ returns the qubit to $|0\rangle$. Measure the qubit state. This procedure is depicted in Fig. 4.11(a).

4. Repeat step 3 except this time replace the operator sequence with

$$\mathcal{C}_{\text{tot},i} = \left[\prod_{i=1}^{m} \mathcal{C}_i \mathcal{C}_{\text{int}}\right] \mathcal{C}^{-1}, \tag{4.13}$$

where $\mathcal{C}_{\text{int}}$ is a Clifford gate of interest to be benchmarked. Measure the qubit state. This procedure is depicted in Fig. 4.11(b).

5. Repeat this process starting at step 3 using the same randomly chosen sequence k times to build up the probability of measuring $|0\rangle$.

6. Start over from step 2, and repeat the entire above process j times for the same value of m. Here, larger values of j give a broader random sampling of gate-dependent errors from the whole Clifford set.

7. Start over from step 1, and repeat the entire protocol for several values of m.

Following the above procedure, one can plot the average post-sequence $|0\rangle$ visibility – in other words, the average probability of returning the qubit to $|0\rangle$ after both $\mathcal{C}_{\text{tot}}$ and $\mathcal{C}_{\text{tot},i}$ – and fit the two resulting depolarizing curves (with and without the interleaved gate $\mathcal{C}_{\text{int}}$) to a power law [165]

$$F_{\text{seq}}(m) = Ap^m + B, \tag{4.14}$$

where state preparation and measurement (SPAM) errors are absorbed into the constants A and B and the depolarizing parameter p represents the average error rate r over all Cliffords (calculated by $r = (d-1)(1-p)/d$, where $d = 2^n$ is the dimensionality of the system; n is the number of qubits). This will result in two depolarizing parameters: one for the standard RB and another for the interleaved gate sequence. These provide the error of the

Gate	$\mathcal{F}_{\omega_{10}/3}$	$\mathcal{F}_{\omega_{10}/41}$
X_{SFQ}	0.94(1)	0.91(2)
$X_{SFQ}/2$	0.955(8)	0.93(3)
$-X_{SFQ}/2$	0.957(5)	0.95(3)
Y_{SFQ}	0.939(5)	0.94(3)
$Y_{SFQ}/2$	0.969(6)	0.92(3)
$-Y_{SFQ}/2$	0.946(6)	0.95(2)

Table 4.4: SFQ gate fidelities measured with randomized benchmarking.

gate of interest by

$$r_{int} = \frac{(d-1)(1-p_{int}/p)}{d}, \tag{4.15}$$

where p_{int} (p) is the depolarizing parameter from the interleaved (standard) RB procedure. The gate fidelity is then defined by $\mathcal{F} = 1 - r_{int}$. This style of procedure has been used in a wide variety of applications in superconducting qubits including the automated calibration of quantum gates [174], the probing of phase noise on otherwise difficult-to-access timescales [175], and has also been used to characterize two-qubit gate processes [176, 177]. There is also work showing that one is able to efficiently benchmark non-Clifford gates in a similar fashion [178] as well as work in progress providing for three-qubit gate benchmarking [179].

Figure 4.11(c) shows example depolarizing curves and Table 4.4 lists extracted gate fidelities $\mathcal{F}$ for the X_{SFQ}, $\pm X_{SFQ}/2$, Y_{SFQ}, $\pm Y_{SFQ}/2$ gates realized with subharmonic drive at both $\omega_{10}/3$ (X_{SFQ}-gate time of 28 ns) and $\omega_{10}/41$ (X_{SFQ}-gate time of 380 ns). For drive at $\omega_{10}/3$, we find gate fidelities in the range 94-97%; for drive at $\omega_{10}/41$, the fidelities are only slightly lower, in the range from 91-95%. In all cases, infidelity is dominated by enhanced qubit relaxation and dispersion induced by QP poisoning from operation of the dissipative SFQ driver; we discuss this effect in detail in the next section. Generally, the shorter $\pi/2$ sequences show higher fidelity than the longer π sequences. This can be understood from the fact that the total number of generated QPs depends on the number of phase slips

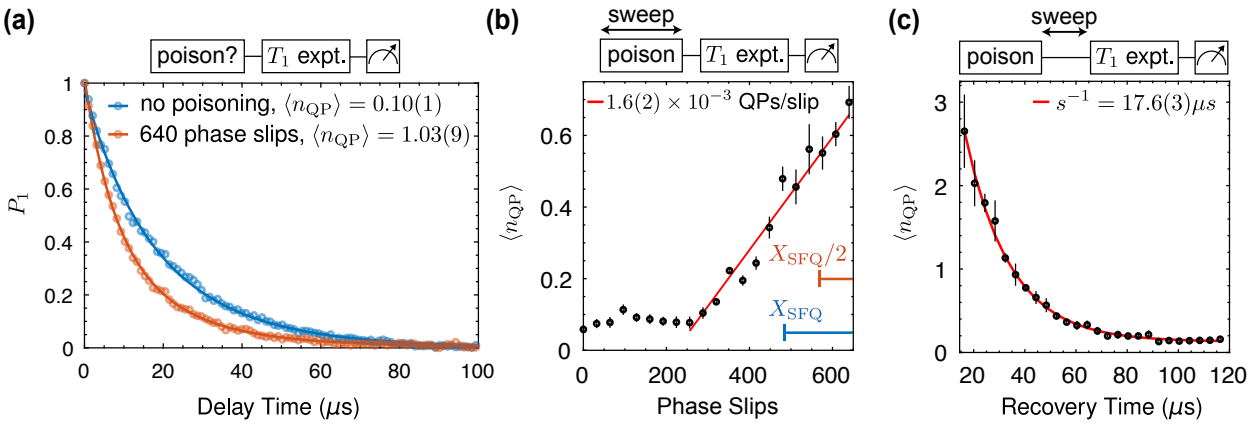

Figure 4.12: QP poisoning of the qubit induced by operation of the SFQ driver. **(a)** Energy decay curves with and without a prior applied poisoning pulse from the SFQ driver. The enhanced relaxation rate can be attributed to an increase in the mean number of QPs $\langle n_{QP} \rangle$ coupled to the qubit. **(b)** $\langle n_{QP} \rangle$ versus number of phase slips in the SFQ poisoning pulse. We find $1.6(2) \times 10^{-3}$ QPs couple to the qubit per JJ phase slip. The lengths of single X_{SFQ} (blue) and $X_{SFQ}/2$ (orange) gates are shown for reference. **(c)** QP recovery experiment for a fixed poisoning pulse (~ 20k phase slips) as a function of the time between the poisoning pulse and the T_1 experiment.

and hence on sequence length, and so the experimentally found relationship between gate fidelity $\mathcal{F}$ and the number of phase slips required to perform said gate is shown in Fig 4.11(d). It is also notable that gate fidelities at the two subharmonic drive frequencies are roughly comparable, despite the order-of-magnitude difference in sequence length. In the following, we provide a detailed discussion of QP poisoning in the quantum-classical hybrid circuit.

4.4 Quasiparticle Poisoning

Nonequilibrium QPs are a well-known source of decoherence [180, 181] and temporal instability [78, 182, 183] in Josephson qubits. There have been prior detailed studies of QP poisoning in phase [184, 185], charge [186], flux [78], and transmon [187, 188] qubits. A variety of approaches to the suppression of QP poisoning have been explored, including normal metal "traps" [189–192], optimization of device geometry [188], gap engineering [193, 194],

trapped magnetic flux vortices [188, 195], and dynamical QP pumping sequences [196]. Generally speaking, the most reliable strategy to suppress QP-induced decoherence is to minimize the generation rate of nonequilibrium QPs by housing the qubit in a light-tight enclosure with extensive IR filtering and by employing inline filters in order to minimize the flux of pair-breaking photons to the qubit chip [197, 198]. For the approach we pursue here, however, it is impossible to avoid QP generation at the device level. Each clock cycle of the trigger waveform induces four phase slips in the driver circuit, one in each JJ of the dc/SFQ converter; each phase slip is accompanied by QP generation. Since the SFQ driver and qubit circuit are located on the same substrate, the generated QPs will poison the qubit circuit either by direct diffusion or by phonon-mediated coupling [190].

4.4.1 QP Effect on Qubit Characteristics

We investigate the influence of nonequilibrium QPs by intentionally poisoning the qubit with an off-resonant SFQ drive that generates QPs at a well-defined rate while producing negligible coherent excitation of the qubit. In the experiments described in this Section, all coherent qubit manipulations are performed using conventional microwave techniques, and the SFQ driver is used exclusively to generate QPs. Figure 4.12(a) shows energy relaxation curves for two separate T_1 experiments, one with and one without a prior poisoning pulse consisting of 640 phase slips delivered at a rate $\omega_d/2\pi = 1.6$ GHz; the poisoning pulse length corresponds to approximately seven $X_{SFQ}/2$ gates. We fit the measured relaxation curves to the following relation to extract the mean number of QPs coupled to the qubit $\langle n_{QP} \rangle$ by the poisoning pulse [182]

$$P_1(t) = \exp\left[\langle n_{QP} \rangle \left(e^{-t/T_{1,QP}} - 1\right) - t/T_{1,R}\right]; \tag{4.16}$$

here, $1/T_{1,QP}$ is the decay rate of the qubit per QP and $1/T_{1,R}$ is the residual decay rate from all other loss channels. In the absence of an explicit poisoning pulse, we find a background

$\langle n_{QP} \rangle = 0.10(1)$ [blue curve in Fig. 4.12(a)]. In contrast, the 640-phase slip poisoning pulse leads to $\langle n_{QP} \rangle = 1.03(9)$ [orange curve in Fig. 4.12(a)]. In Fig. 4.12(b) we show results from a series of poisoning experiments where the length of the poisoning pulse is varied prior to the T_1 scan. We observe a slow initial turn-on of QP poisoning. For short poisoning pulses, it is likely that nonequilibrium QP density in the vicinity of the SFQ driver is too low to provide for significant phonon-mediated poisoning of the qubit [190], as this process relies on high local QP densities to promote recombination and phonon emission in the vicinity of the SFQ driver. However, following approximately 250 phase slips, we observe a linear increase in $\langle n_{QP} \rangle$ with respect to the number of phase slips in the poisoning pulse. In this regime, we find that a single phase slip in the SFQ driver couples approximately $1.6(2) \times 10^{-3}$ QPs to the qubit. In a related experiment, we insert a variable delay between a fixed QP poisoning pulse and the T_1 scan. In Fig. 4.12(c) we plot $\langle n_{QP} \rangle$ as a function of recovery time following the QP poisoning pulse. We observe an exponential decay of $\langle n_{QP} \rangle$ with an effective trapping time of $s^{-1} = 17.6(3)$ μs; this trapping time is consistent with that observed in prior studies of QP poisoning of linear microwave modes in thin-film devices [190].

The complex QP admittance seen by the qubit includes both real and imaginary parts; while the former leads to enhanced relaxation, the latter induces a qubit frequency shift. We have examined the connection between QP loss and dispersion in our device by performing both T_1 and Ramsey experiments following intentional QP poisoning pulses both with a variable number of phase slips and fixed recovery time [Figs. 4.13(a-c)] and a fixed number of phase slips followed by a variable recovery time [Figs. 4.13(d-f)]; these scans provide access to both the QP contribution Γ to the qubit relaxation rate and to the frequency shift $\delta\omega_{10}$ induced by the presence of nonequilibrium QPs as prescribed by

$$\Gamma \simeq \frac{\mathrm{Re}\{Y_{QP}(\omega_{10})\}}{C} \tag{4.17}$$

$$\delta\omega_{10} \simeq -\frac{\mathrm{Im}\{Y_{QP}(\omega_{10})\}}{2C}. \tag{4.18}$$

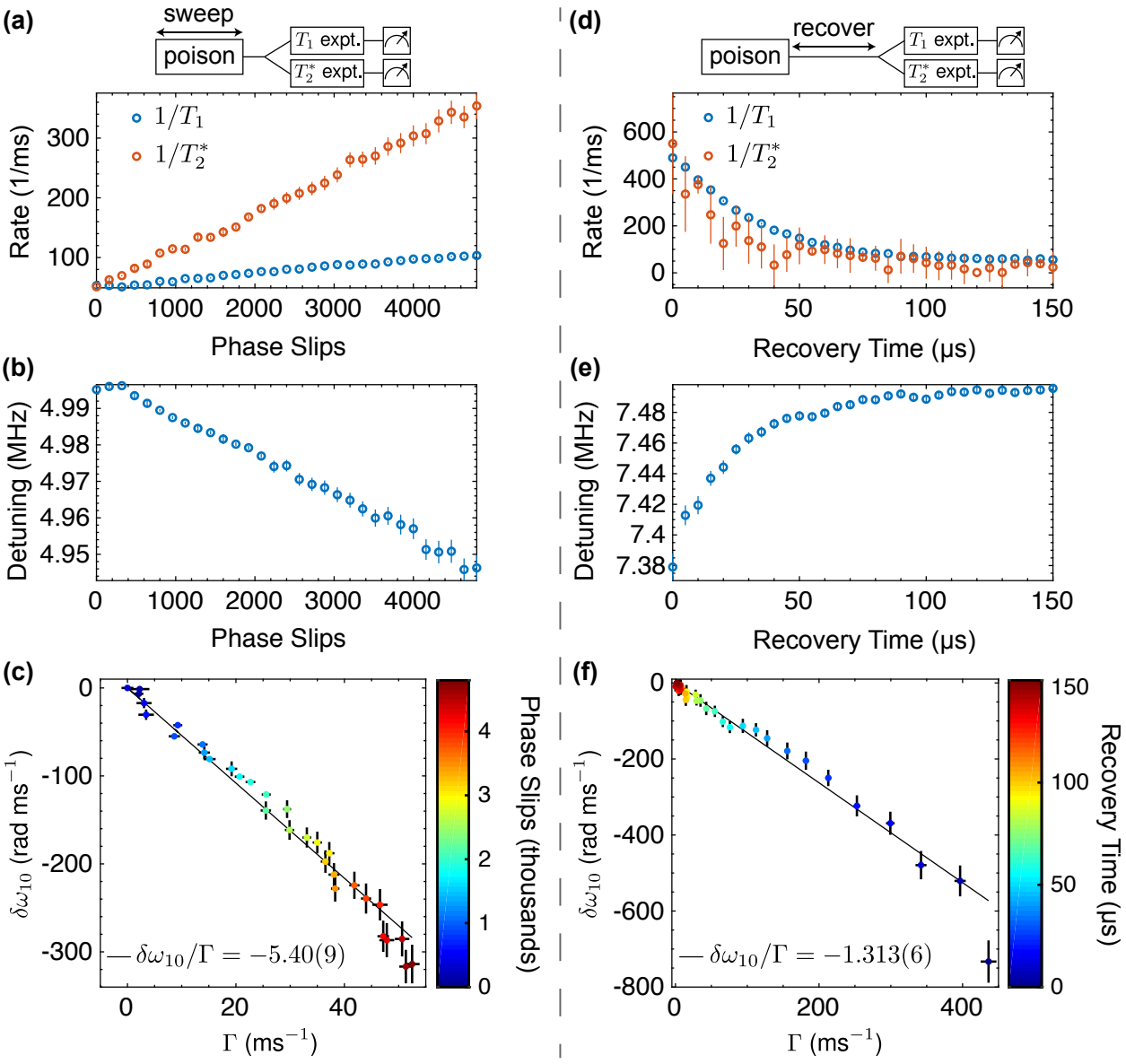

Figure 4.13: **(a)** Qubit relaxation and dephasing rates as functions of the number of phase slips used to poison the circuit for a fixed recovery time of 24 ns. The experiment block sequence above the plot is valid for panels **(a-c)**. **(b)** Extracted Ramsey detuning as a function of the number of phase slips used to poison the circuit for a fixed recovery time of 24 ns. Here, there was a purposeful detuning of 5 MHz from the qubit frequency at zero poisoning. **(c)** Parametric plot of qubit frequency shift $\delta\omega_{10}$ versus QP-induced decay rate Γ using data from **(b)** and **(a)**, respectively. **(d)** Qubit relaxation and dephasing rates as functions of recovery time for a fixed number of circuit poisoning phase slips. The experiment block sequence above the plot is valid for panels **(d-f)**. **(e)** Extracted Ramsey detuning as a function of recovery time for a fixed number of circuit poisoning phase slips. Here, there was a purposeful detuning of 7.5 MHz from the qubit frequency at zero poisoning. **(f)** Parametric plot of qubit frequency shift $\delta\omega_{10}$ versus QP-induced decay rate Γ using data from **(e)** and **(d)**, respectively.

In Fig. 4.13(c, f) we show parametric plots of $\delta\omega_{10}$ versus Γ for various numbers of phase slips and recovery times, respectively; we observe a clear linear relationship between QP loss and dispersion in both cases, however with a different linear slope for both experiments. Within a simplified model that assumes rapid relaxation of nonequilibrium QPs to the gap edge, the ratio of $\delta\omega_{10}$ to Γ can be expressed as [181, 185]

$$\frac{\delta\omega_{10}}{\Gamma} = -\frac{1}{2}\left[1 + \pi\sqrt{\frac{\hbar\omega_{10}}{2\Delta}}\right], \tag{4.19}$$

where ω_{10} is the qubit fundamental transition frequency in the absence of QPs and 2Δ is the superconducting gap of the junction electrodes. A fit to our data in both cases yields a slope $\delta\omega_{10}/\Gamma$ that is larger than that predicted by Eq. (4.19); however, the assumption of low-energy QPs is likely invalid in our experiments, and it is expected that this slope will depend sensitively on the details of the QP distribution. This assertion is supported by the fact that for the two performed experiments in Fig. 4.13, we see two very different results for the $\delta\omega_{10}/\Gamma$ ratio.

4.4.2 QP Effect on Ramsey Experiment

As is visible in Fig. 4.7(c), the Ramsey fringes obtained using pulse-based $X_{SFQ}/2$ gates appear asymmetric in nature, which is not the expected case for a good qubit for which it should not matter whether the drive detuning is positive or negative from the qubit resonance [199]. In the context of the measured qubit frequency shift as a function of poisoning and recovery times in Figs. 4.13(b, e), we can begin to understand the mechanism causing this asymmetry in the interference pattern of Fig. 4.7(c). First, in Fig. 4.13(b) we see a linear trend in qubit frequency detuning as a function of drive time; in a Ramsey experiment, this happens during the $X_{SFQ}/2$ pulses which last for a time $t < \tau_{\pi/2}$. Then, in Fig. 4.13(e), we see an exponential decay of this qubit detuning back towards the true ω_{10}; this happens in a Ramsey experiment during the time period $\tau_{\pi/2} \leqslant t < \tau_{\pi/2} + \tau_{idle}$.

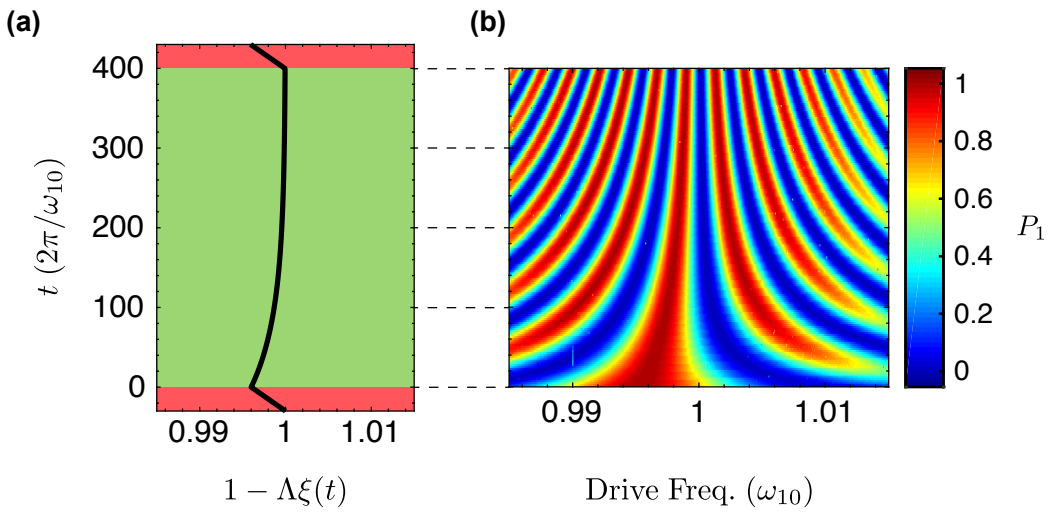

Figure 4.14: Ramsey interferometry simulation with dynamic qubit frequency. **(a)** Plot of the qubit detuning factor $\Lambda\xi(t)$ for $\Lambda = 0.004$ and $\xi(t)$ as in Eq. 4.21 and characteristic times listed in main text. The shaded red regions are the times during which simulated $X_{SFQ}/2$ pulses are being driven, inducing a frequency shift. The shaded green region is the idle time interleaved between the two $X_{SFQ}/2$ pulses. **(b)** Ramsey fringes obtained using the master equation solver in QuTIP [200] to solve the Hamiltonian in Eq. 4.20 by simulating a Ramsey pulse sequence. The asymmetry is in qualitative agreement with the asymmetry seen in Fig. 4.7(c).

Finally, the final X_{SFQ} pulse further linearly shifts the qubit, again for the duration $\tau_{\pi/2}$. This can be modeled using the time-dependent Hamiltonian

$$\hat{\mathcal{H}} = \frac{\hbar\omega_{10}}{2}\left[\mathcal{I} - (1+\Lambda\xi(t))\hat{\sigma}_z\right]; \tag{4.20}$$

$$\xi(t) = \begin{cases} t/\tau_{\pi/2} & t < \tau_{\pi/2} \\ e^{-(t-\tau_{\pi/2})/\tau_r} & \tau_{\pi/2} \leqslant t < \tau_{\pi/2} + \tau_{idle} \\ e^{-(\tau_{idle}-\tau_{\pi/2})/\tau_r} + (t - \tau_{idle} - \tau_{\pi/2})/\tau_{\pi/2} & \tau_{\pi/2} + \tau_{idle} \leqslant t \end{cases}, \tag{4.21}$$

where Λ is a factor by which the qubit precession time changes, $\xi(t)$ is the time-dependence of the detuning on the pulse timing of a simple Ramsey sequence, and τ_r is the recovery time of the qubit frequency while QPs exit the qubit system. Here, t is the full experiment time including the time during both the $X_{SFQ}/2$ pulses and the idle time interleaving them (so $0 < t \leqslant 2\tau_{\pi/2} + \tau_{idle}$). This Hamiltonian along with the appropriate Ramsey pulse

sequence has been simulated using the master-equation solver in QuTIP [200]. The pulse sequence, dynamic qubit frequency, and simulation results are shown in Fig. 4.14. Here, $\Lambda = 0.004$, $\tau_{\pi/2} = 30 \times (2\pi/\omega_{10})$, and the characteristic recovery time of the qubit frequency is $\tau_r = 3\tau_{\pi/2}$. We see a clear asymmetry in the simulated Ramsey fringes in similar fashion to those obtained by experiment in Fig. 4.7(c), giving us at least a qualitative explanation for the measured asymmetry in the experimental data.

4.5 Summary and Current Work

In this Chapter, we have described a quantum-classical hybrid circuit; it is a device which incorporates a superconducting transmon qubit with a superconducting classical logic circuit based on a dc/SFQ converter from the RSFQ SCE family cofabricated on the same Si chip. We have used the dc/SFQ converter circuit to drive arbitrary coherent operations on the transmon qubit, and we have characterize how well we are able to do this with this specific device by employing interleaved randomized benchmarking. We find gate fidelities top out at about $\mathcal{F} \sim 95\%$ on average when driving the converter at the third subharmonic of the qubit frequency. In investigating what potential limitations exist in our system, we explored in detail the deleterious effect of quasiparticles generated by our controller circuit on the transmon qubit. We then showed several results which point to enhanced decoherence and an inadvertent qubit frequency shift as potential culprits insofar as limitations to quantum operation fidelity.

4.5.1 Multi-chip Module

While the current design has the simplicity of being a single chip, it also suffers from the fact that the transmon qubit shares a substrate with a naturally dissipative circuit, the dc/SFQ converter. A natural next step then in the author's view is to look to the realm of multi-chip modules utilizing a flip-chip architecture to break the substrate connection

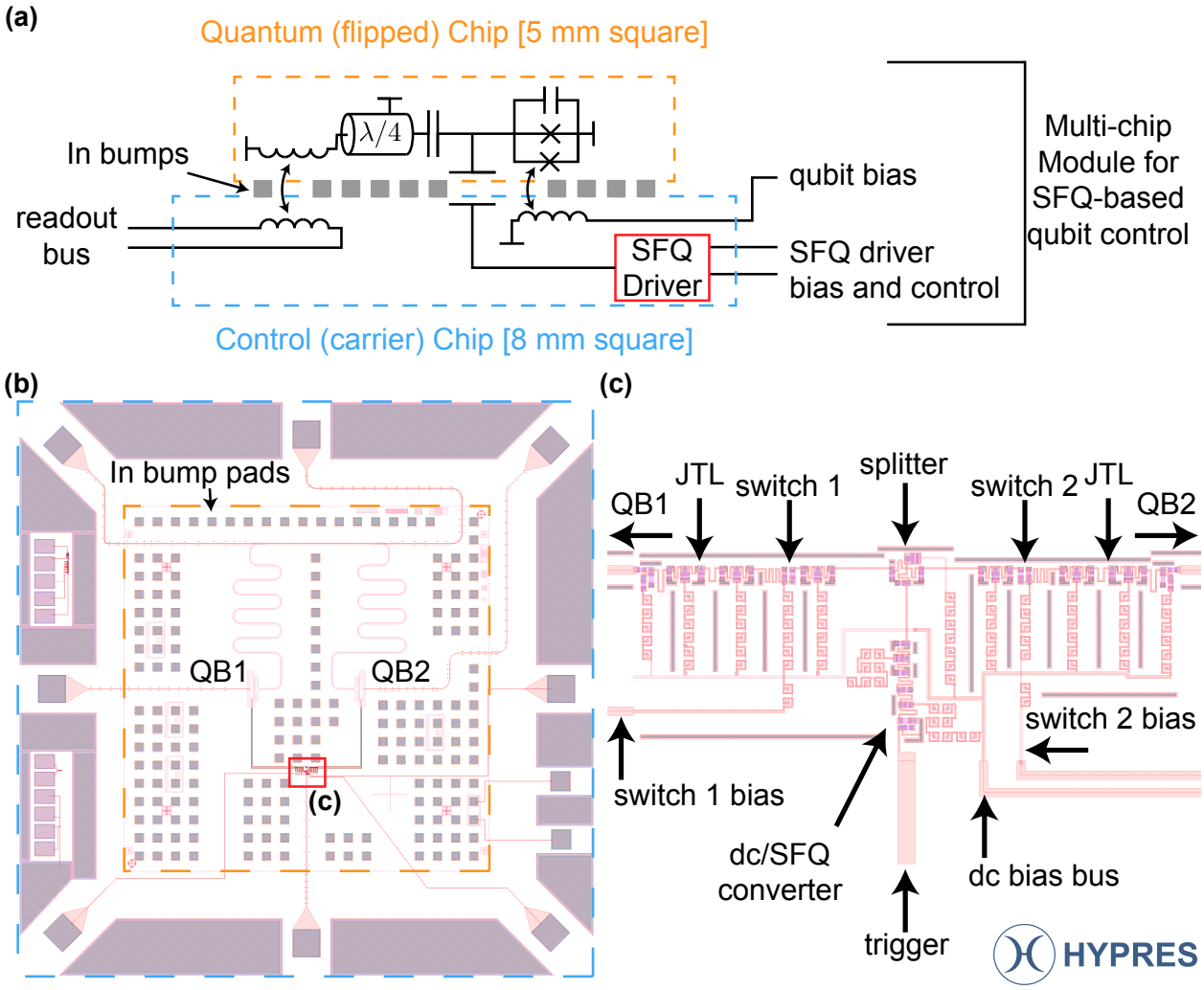

Figure 4.15: Proposed MCM for SFQ control of a qubit. **(a)** Schematic circuit diagram showing which circuit elements will reside on the quantum (flipped) chip and the classical (carrier) chip. Here, the two chips are arranged in a flip-chip architecture employing superconducting In bump bonds to mechanically assemble the MCM. A readout bus on the carrier is used to measure a $\lambda/4$ cavity on the flipped chip which is capacitively coupled to a flux-tunable transmon. The transmon bias is provided via a flux coupled into the SQUID loop from a current line on the carrier chip. SFQ pulses used for qubit control are capacitively coupled across the chip-to-chip gap to perform high-fidelity control. **(b)** Top-down view of the electronic layout of the first version of this device. The two qubits (QB1 and QB2) to be controlled are labeled. **(c)** Top-down view of the SFQ control circuitry in the first version of this device. Here, a single dc/SFQ converter sends an SFQ pulse to a splitter which results in an SFQ pulse moving both to the left and right for each clock cycle. The labeled switches control whether or not an SFQ pulse continues on the path towards its respective qubit. A common bus simultaneously biases the dc/SFQ converter, splitter, and JTLs. The electronic layouts presented in panels **(b, c)** were designed, drawn, and later fabricated by HYPRES, Inc, Elmsford, NY 10523.

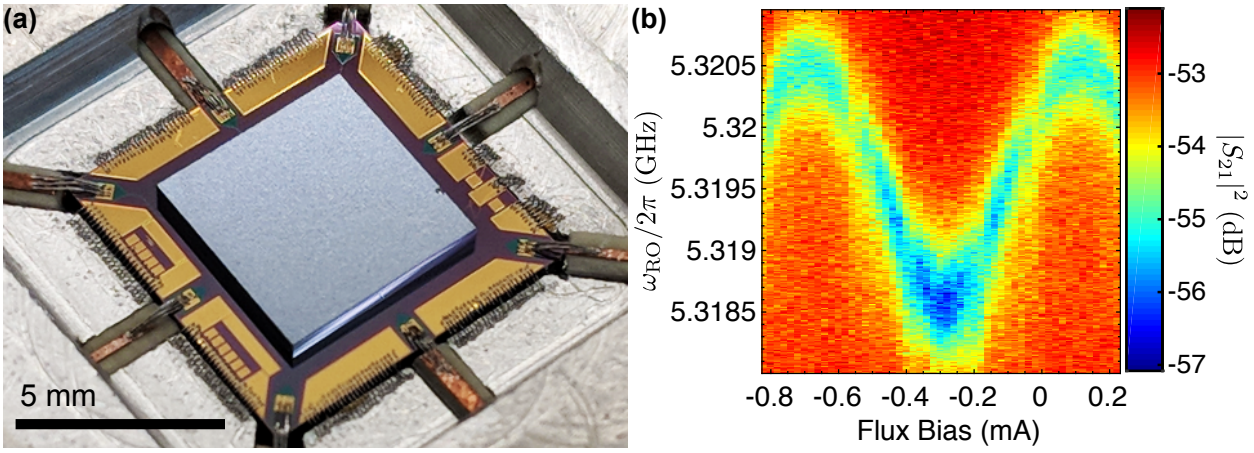

Figure 4.16: **(a)** Optical photograph of the assembled MCM wirebonded into one of our standard sample packages. The bottom (top) chip is the carrier (flipped) chip described in Fig. 4.15(.) The carrier chip was designed and fabricated using HYPRES Process #03-10-45 (Rev. #25), and the final MCM was assembled by HYPRES, Inc, Elmsford, NY 10523. Photo courtesy of J. Nelson, Syracuse University, Syracuse, NY 13244. **(b)** Cavity spectroscopy $|S_{21}|^2$ as a function of both readout frequency ω_{RO} and flux bias through the qubit SQUID loop. Here, the periodicity of the dispersively shifted dressed cavity resonance implies that the flux coupling to the qubit SQUID loop, the qubit-cavity coupling, and the cavity-readout bus coupling are all functional, and a more thorough characterization has yet to be done at the time of this writing. Data courtesy C. H. Liu, University of Wisconsin - Madison, Madison, WI 53706.

between the two circuits. This should reduce the apparent QP poisoning issue to the quantum circuit in two immediate ways: first, the galvanic connection between the classical circuit and quantum circuit will not be interrupted by indium bumps, which has a lower energy gap than niobium. This means that the indium will, in effect, act as a QP trap preventing stray broken Cooper-pairs from traveling to the quantum circuit. Second, the break of substrate should prevent phonon mediated QP poisoning, a dominant loss mechanism as reported by [190]. We believe this next step to be not impractical as far as qubit performance is concerned; there has been a great deal of progress in recent years towards MCMs for use with small-scale qubit arrays [201–206] including data suggesting that a properly engineering MCM can preserve the relatively high coherence times to which users of modern transmons have grown so accustomed [201, 206].

An initial draft of such an MCM is drawn in Fig. 4.15(a). In this design, only the

carrier chip would be subject to wirebonding into the eventual MCM package. All signals transferred between the classical and quantum chip are done so either capacitively or inductively; no signals (with the exception of ground currents) are purposefully transferred via direct galvanic connections. Figure 4.15(b) shows a top-down schematic overview of the designed circuit. Here, there are two qubit-resonator pairs, both of which are readout inductively via a readout bus on the carrier chip. Both qubits are controllable by a single SFQ control circuit (outlined in red). Figure 4.15(c) shows a detailed close-up of the SFQ control circuitry in this design. Here, a single dc/SFQ converter circuit feeds an SFQ pulse splitter, resulting in an SFQ pulse moving towards both qubits for each cycle of the trigger tone at frequency ω_d. However, there also exists a switch on either output of the splitter such that the experimentalist may selectively excite either qubit 1, qubit 2, or both depending on what they are trying to achieve (one can envision attempting to excite and measure both qubits simultaneously to shorten the total experimental time) with the constraint that both qubits will see SFQ pulses at the same rate of arrival due to the nature of the shared trigger line.

4.5.2 Preliminary MCM Results

To date, there has been a modest amount of progress towards realizing the SFQ control MCM outlined in the previous Section. First-round devices have been fabricated and measured in ADRs. Figure 4.16(a) shows an optical photograph of an assembled MCM which has been wirebonded into an Al box. Figure 4.16(b) shows that at least a few milestones have been met: we are able to 1) readout a microwave cavity via a chip-to-chip inductive coupling system, 2) infer that the qubit is coupled to the cavity in some reasonable fashion, and 3) measure the inductive coupling of the qubit flux line into the qubit SQUID loop. We have also been able to perform qubit spectroscopy (not shown) in order to identify the qubit transition frequency, but at the time of this writing the sample awaits experimental time in a DR for full circuit characterization to both measure the coherence of the qubits in

MCM and also to attempt high fidelity coherent manipulation of the qubits on the flipped chip using the SFQ circuitry on the carrier chip.

5 OUTLOOK

5.1 The Vision

One of the motivations for the intense research towards quantum information processing in the solid state is the success story of the miniaturization of classical computational devices made from same. At present, however, the relevant solid state qubit technologies (e.g., quantum dots and Josephson circuits, mentioned previously) are in their infancy with regard to the LSI (large-scale integration) explosion witnessed by transistor-based computers. There are significant physics and engineering challenges between the ~100 qubit level which some groups in Josephson computing are now reaching and an eventual large-scale ~ 100 million qubit processor necessary to build a practical factoring machine [9, 23]. At present, a typical experiment requires approximately one wire per qubit to control and readout small-scale quantum processors[1]. A fair concern for the practitioners of Josephson computing, then, is how does the experimenter control and measure 100 million qubits? The problem presents itselfat present, as requiring ~100 million control lines to carry signals from the room temperature electronics to the quantum processor at the mK stage of a dilution refrigerator DR. Physical volume limitations aside, the heatload on the mK plate would be well outside what any modern DR can handle[2].

It is therefore interesting to look towards CMOS; modern CPUs are composed of *tens of billions* of transistors while maintaining an interconnect count to the outside world of less than a few thousand. While there are a great many differences between the requirements of transistor-based CMOS processors and solid-state quantum processors, the takeaway is that new technologies had to be invented to scale classical computing to the behemoth it is

[1] See the system wiring diagrams of, e.g.,[156, 207–209] for some relatively modern examples of multi-qubit wiring diagrams.

[2] Modern DRs have a ~ 10 mK stage with a cooling power of, on the very high end, 100 μW. Assuming a heat load of 1 nW per coaxial cable delivering to the mK stage [210], 100 million wires would impart a total load of 100 mW. At present, the author is aware of no technology which can provide for a mK environment with such a high cooling power.

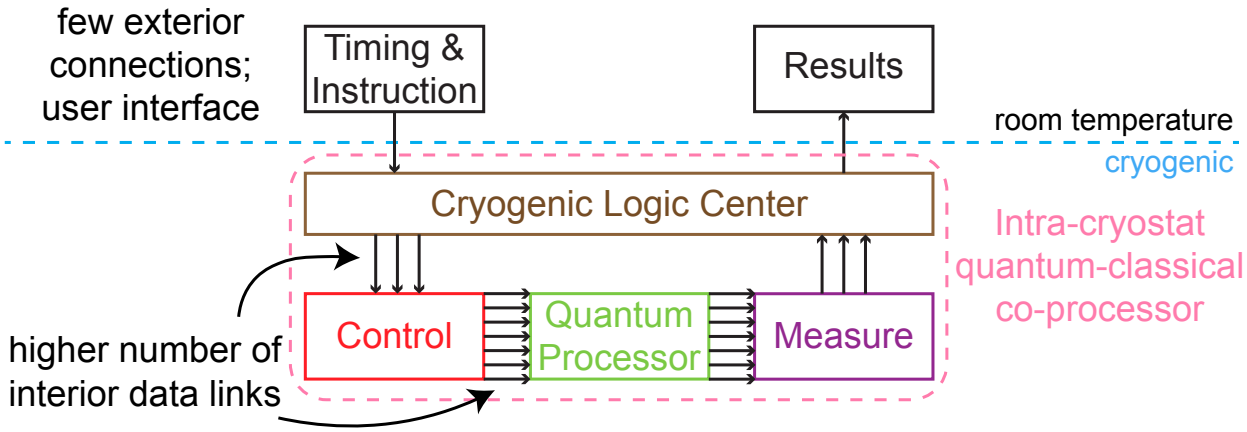

Figure 5.1: A vision for a control and measurement scheme of a one-day large-scale quantum processor. Here, only minimal connections to the outside world are required to provide the quantum-classical co-processor with instructions and to obtain calculation results while an enormity of cryogenic interconnects and logic devices does most of the requisite qubit control and measurement.

today, and among those achievements was the reduction of required input hardware to instruct the processor to perform a calculation and then relay the result back to memory or the instructor. Using this as a "jumping off point," one imagines a similar path should be expected for quantum processors; in fact, practitioners of superconducting qubits already have a potential path towards building an intra-cryostat, all-superconducting quantum-classical co-processor in the well-established technologies of classical logic devices based on superconducting circuits [211]. A simplified schematic outline for what this could look like from a logic/control standpoint is shown in Fig. 5.1, where the number of arrows connecting the individual blocks is meant to indicate a relative number of interconnects at different stages of computation. The "Cryogenic Logic Center" is left arbitrarily vague in construction because it is impossible at present time to state exactly what technology will work best for such an endeavor; at present, there have been numerous studies looking at cryogenic CMOS-based FPGAs [212–217] for the purposes of intra-cryostat logic and superconducting "flux-DACs" have also been demonstrated as a controller for a superconducting quantum annealer [218]. Both of these point in the direction of including a classical co-processor in

the many-qubit cryostat, a path which seems likely inevitable for a large-scale quantum processor.

5.2 Conclusion

In this thesis, we have described a scheme for coherent qubit control using quantized flux pulses derived from the SFQ digital logic family. The approach offers a path to tight integration of a classical coprocessor with a large-scale multiqubit circuit for the purpose of reducing heat load, latency, and overall system footprint. In current experiments, we access the full single-qubit Clifford set and achieve gate fidelities $\mathcal{F} \sim 95\%$, measured using interleaved RB. This result is limited by QP poisoning induced by operation of the dissipative SFQ pulse driver. However, there are several straightforward modifications that could be employed in a future implementation to significantly suppress QP poisoning. For example, it should be possible to fabricate the classical SFQ driver circuit and the qubit on separate chips that are flip-chip bonded in a multichip module (MCM). With such an MCM arrangement as depicted in Fig 4.15, SFQ pulses would be coupled to the qubit chip capacitively across the chip-to-chip gap of the MCM. The natural choice for the MCM bump bonds, indium, would provide a low-gap barrier to direct QP diffusion between the chips, and recombination phonons generated by QPs in the bumps would have insufficient energy to break pairs in the niobium groundplane of the quantum chip. The MCM approach would have the additional advantage of allowing a modular fabrication, obviating the need to develop a process flow that protects the delicate quantum circuit from materials-induced loss associated with the complex, multilayer SFQ driver stack. Ultimately, we view the MCM approach as the most promising path to scaling the two-dimensional surface code [23], as it provides for the necessary nearest-neighbor connectivity of the quantum array while allowing tight integration of proximal control and measurement elements. There has been significant recent progress in the development of robust superconducting

indium bump bonding of MCMs [201–206], and it has been shown that qubit coherence can be fully preserved in a properly designed MCM [201, 206]. There has also been work done to discuss a potential path forward for the integration of SFQ technology into the many-qubit cryostat of an eventual large-scale quantum processor [211].

A second straightforward modification to suppress QP poisoning would be to move from a high-J_c process for the SFQ driver circuit to a low-J_c, millikelvin-optimized process. SFQ control elements should remain robust against fluctuations at millikelvin temperatures for critical currents that are two orders of magnitude smaller than those used in the current work [219]; as the energy dissipated per phase slip scales linearly with critical current, a millikelvin-optimized SFQ driver is expected to generate nonequilibrium QPs at a factor ~100 lower rate. The inductances required for such an SFQ pulse driver would be correspondingly larger, leading to a larger physical footprint for the SFQ controller; global optimization of the SFQ control system would require tradeoffs between dissipation and physical size.

Finally, the incorporation of normal metal QP traps in the hybrid SFQ-qubit circuit or MCM is expected to significantly suppress QP poisoning. When QPs diffuse into a normal metal, they interact strongly with electrons and quickly relax below the gap edge, so that they are unable to re-enter the superconductor. The effectiveness of normal metal traps in removing nonequilibrium QPs has been demonstrated previously in a variety of contexts [189, 220–223]. In related work, it has been shown that appropriate engineering of the spatial profile of the superconducting gap in single-Cooper-pair transistor (SCPT) devices can be used to confine nonequilibrium QPs to regions of the circuit where they are unable to degrade device performance [193]. For the application we consider here, the generation of QPs is localized to the driver elements that undergo phase slips; the phase slips lead to an elevated local population of nonequilibrium QPs in the vicinity of the driver. Poisoning proceeds by multiple stages of phonon emission and pair-breaking, so that extensive coverage of the device with normal metal traps (as opposed to local coverage near

or surrounding the QP generation point) is required to suppress poisoning. The addition of QP traps has been shown to suppress QP poisoning of linear resonator modes by 1-2 orders of magnitude [190]. The optimal configuration of QP traps in a quantum-classical MCM is a question that would likely need to be addressed experimentally.

Once the problem of QP poisoning is addressed, we expect leakage out of the computational subspace to represent the dominant source of error in SFQ-based gates. While naive, resonant pulse sequences of the type explored here are expected to yield gate fidelity of order 99.9% [161], it has been shown that more complex SFQ pulse sequences involving variable pulse-to-pulse intervals can yield gates with fidelity better than 99.99% [162]. This is compatible with the fidelities of the best reported microwave-based gates and sufficient for scaling in the two-dimensional surface code, enabling the realization of a one-day fault-tolerant quantum computational machine based on Josephson devices.

DISCARD THIS PAGE

COLOPHON

This thesis was typeset with LaTeX and uses Gyre Pagella; it is based on a template by Will Benton located at

https://github.com/willb/wi-thesis-template.

Many of the figures for this thesis were generated using Adobe Illustrator and all data plots were generated in Matlab. All data were acquired using a custom experimental codebase written in Python2. Optical photographs were acquired using a Canon 70d DSLR body with a 200-mm telephoto zoom lens boosted by a 20-mm macro tube. Optical micrographs were taken using a NIKON optical microscope with digital camera attachment. All photo post-processing, if any, was performed with Adobe Photoshop.

The LaTeX source for this dissertation, as well as all of the figures and some of the data, is available on the World Wide Web at

https://gitlab.com/eleonardjr/thesis.

Last update: 4 September 2018

BIBLIOGRAPHY

[1] Editorial, *Beautiful machines*, Nat. Phys. **11**, 365 EP (2015).

[2] F. C. Williams and T. Kilburn, *Electronic Digital Computers*, Nature **162**, 487 EP (1948).

[3] Editorial, *Calculating Machines*, Nature **161**, 712 EP (1948).

[4] J. Bardeen and W. H. Brattain, *The Transistor, A Semi-Conductor Triode*, Phys. Rev. **74**, 230 (1948).

[5] S. B. Desai, S. R. Madhvapathy, A. B. Sachid, J. P. Llinas, Q. Wang, G. H. Ahn, G. Pitner, M. J. Kim, J. Bokor, C. Hu, H. S. P. Wong, and A. Javey, *Mos₂ transistors with 1-nanometer gate lengths*, Science **354**, 99 (2016).

[6] G. E. Moore, *Cramming More Components Onto Integrated Circuits*, Electronics **38**, 114 (1965).

[7] R. P. Feynman, *Simulating Physics with Computers*, Int. J. Theor. Phys. **21**, 467 (1982).

[8] R. P. Feynman, *Quantum mechanical computers*, Found. Phys. **16**, 507 (1986).

[9] P. Shor, *Polynomial-Time Algorithms for Prime Factorization and Discrete Logarithms on a Quantum Computer*, SIAM J. Comput. **26**, 1484 (1997).

[10] R. L. Rivest, A. Shamir, and L. Adleman, *A method for obtaining digital signatures and public-key cryptosystems*, Commun. ACM **21**, 120 (1978).

[11] L. K. Grover, *A fast quantum mechanical algorithm for database search*, in *Proc. 28th Annu. ACM Symp. Theory Comput.* (1996).

[12] B. P. Lanyon, J. D. Whitfield, G. G. Gillett, M. E. Goggin, M. P. Almeida, I. Kassal, J. D. Biamonte, M. Mohseni, B. J. Powell, M. Barbieri, A. Aspuru-Guzik, and A. G. White, *Towards quantum chemistry on a quantum computer*, Nat. Chem. **2**, 106 EP (2010).

[13] P. J. J. O'Malley, R. Babbush, I. D. Kivlichan, J. Romero, J. R. McClean, R. Barends, J. Kelly, P. Roushan, A. Tranter, N. Ding, B. Campbell, Y. Chen, Z. Chen, B. Chiaro, A. Dunsworth, A. G. Fowler, E. Jeffrey, E. Lucero, A. Megrant, J. Y. Mutus, M. Neeley, C. Neill, C. Quintana, D. Sank, A. Vainsencher, J. Wenner, T. C. White, P. V. Coveney, P. J. Love, H. Neven, A. Aspuru-Guzik, and J. M. Martinis, *Scalable Quantum Simulation of Molecular Energies*, Phys. Rev. X **6**, 031007 (2016).

[14] J. I. Colless, V. V. Ramasesh, D. Dahlen, M. S. Blok, M. E. Kimchi-Schwartz, J. R. McClean, J. Carter, W. A. de Jong, and I. Siddiqi, *Computation of Molecular Spectra on a Quantum Processor with an Error-Resilient Algorithm*, Phys. Rev. X **8**, 011021 (2018).

[15] M. A. Nielsen and I. L. Chuang, *Quantum Computation and Quantum Information* (Cambridge University Press, 2000).

[16] D. P. DiVincenzo, *The Physical Implementation of Quantum Computation*, Fortschr. Phys. **48**, 771 (2000).

[17] E. Knill, *Quantum computing with realistically noisy devices*, Nature **434**, 39 EP (2005).

[18] T. D. Ladd, F. Jelezko, R. Laflamme, Y. Nakamura, C. Monroe, and J. L. O'Brien, *Quantum computers*, Nature **464**, 45 EP (2010).

[19] C. Monroe, D. M. Meekhof, B. E. King, W. M. Itano, and D. J. Wineland, *Demonstration of a Fundamental Quantum Logic Gate*, Phys. Rev. Lett. **75**, 4714 (1995).

[20] A. R. Calderbank and P. W. Shor, *Good quantum error-correcting codes exist*, Phys. Rev. A **54**, 1098 (1996).

[21] A. M. Steane, *Error Correcting Codes in Quantum Theory*, Phys. Rev. Lett. **77**, 793 (1996).

[22] A. M. Steane, *Enlargement of Calderbank-Shor-Steane quantum codes*, IEEE Trans. Inf. Theory **45**, 2492 (1999).

[23] A. G. Fowler, M. Mariantoni, J. M. Martinis, and A. N. Cleland, *Surface codes: Towards practical large-scale quantum computation*, Phys. Rev. A **86**, 032324 (2012).

[24] C. Monroe, *Quantum information processing with atoms and photons*, Nature **416**, 238 EP (2002).

[25] I. A. Walmsley and M. G. Raymer, *Toward Quantum-Information Processing with Photons*, Science **307**, 1733 (2005).

[26] P. Kok, W. J. Munro, K. Nemoto, T. C. Ralph, J. P. Dowling, and G. J. Milburn, *Linear optical quantum computing with photonic qubits*, Rev. Mod. Phys. **79**, 135 (2007).

[27] G. J. Milburn, *Photons as qubits*, Phys. Scr. **2009**, 014003 (2009).

[28] P. G. Kwiat, K. Mattle, H. Weinfurter, A. Zeilinger, A. V. Sergienko, and Y. Shih, *New High-Intensity Source of Polarization-Entangled Photon Pairs*, Phys. Rev. Lett. **75**, 4337 (1995).

[29] P. G. Kwiat, E. Waks, A. G. White, I. Appelbaum, and P. H. Eberhard, *Ultrabright source of polarization-entangled photons*, Phys. Rev. A **60**, R773 (1999).

[30] X.-L. Wang, Y.-H. Luo, H.-L. Huang, M.-C. Chen, Z.-E. Su, C. Liu, C. Chen, W. Li, Y.-Q. Fang, X. Jiang, J. Zhang, L. Li, N.-L. Liu, C.-Y. Lu, and J.-W. Pan, *18-Qubit Entanglement with Six Photons' Three Degrees of Freedom*, Phys. Rev. Lett. **120**, 260502 (2018).

[31] M. Saffman, T. G. Walker, and K. Mølmer, *Quantum information with Rydberg atoms*, Rev. Mod. Phys. **82**, 2313 (2010).

[32] M. Saffman, *Quantum computing with atomic qubits and rydberg interactions: progress and challenges*, J. Phys. B **49**, 202001 (2016).

[33] J. M. Auger, S. Bergamini, and D. E. Browne, *Blueprint for fault-tolerant quantum computation with Rydberg atoms*, Phys. Rev. A **96**, 052320 (2017).

[34] K. R. Brown, J. Kim, and C. Monroe, *Co-designing a scalable quantum computer with trapped atomic ions*, npj Quantum Inf. **2**, 16034 EP (2016).

[35] K. M. Maller, M. T. Lichtman, T. Xia, Y. Sun, M. J. Piotrowicz, A. W. Carr, L. Isenhower, and M. Saffman, *Rydberg-blockade controlled-not gate and entanglement in a two-dimensional array of neutral-atom qubits*, Phys. Rev. A **92**, 022336 (2015).

[36] T. Xia, M. Lichtman, K. Maller, A. W. Carr, M. J. Piotrowicz, L. Isenhower, and M. Saffman, *Randomized Benchmarking of Single-Qubit Gates in a 2D Array of Neutral-Atom Qubits*, Phys. Rev. Lett. **114**, 100503 (2015).

[37] D. Loss and D. P. DiVincenzo, *Quantum computation with quantum dots*, Phys. Rev. A **57**, 120 (1998).

[38] F. A. Zwanenburg, A. S. Dzurak, A. Morello, M. Y. Simmons, L. C. L. Hollenberg, G. Klimeck, S. Rogge, S. N. Coppersmith, and M. A. Eriksson, *Silicon quantum electronics*, Rev. Mod. Phys. **85**, 961 (2013).

[39] E. Kawakami, P. Scarlino, D. R. Ward, F. R. Braakman, D. E. Savage, M. G. Lagally, M. Friesen, S. N. Coppersmith, M. A. Eriksson, and L. M. K. Vandersypen, *Electrical control of a long-lived spin qubit in a si/sige quantum dot*, Nat. Nanotechnol. **9**, 666 EP (2014).

[40] J. T. Muhonen, J. P. Dehollain, A. Laucht, F. E. Hudson, R. Kalra, T. Sekiguchi, K. M. Itoh, D. N. Jamieson, J. C. McCallum, A. S. Dzurak, and A. Morello, *Storing quantum information for 30 seconds in a nanoelectronic device*, Nat. Nanotechnol. **9**, 986 EP (2014).

[41] M. Veldhorst, J. C. C. Hwang, C. H. Yang, A. W. Leenstra, B. de Ronde, J. P. Dehollain, J. T. Muhonen, F. E. Hudson, K. M. Itoh, A. Morello, and A. S. Dzurak, *An addressable quantum dot qubit with fault-tolerant control-fidelity*, Nat. Nanotechnol. **9**, 981 EP (2014).

[42] J. Clarke and F. K. Wilhelm, *Superconducting quantum bits*, Nature **453**, 1031 (2008).

[43] M. H. Devoret and R. J. Schoelkopf, *Superconducting Circuits for Quantum Information: An Outlook*, Science **339**, 1169 (2013).

[44] J. M. Gambetta, J. M. Chow, and M. Steffen, *Building logical qubits in a superconducting quantum computing system*, npj Quantum Inf. **3**, 2 (2017).

[45] W.-Y. Liu, D.-N. Zheng, and S.-P. Zhao, *Superconducting quantum bits*, Chin. Phys. B **27**, 027401 (2018).

[46] C. Neill, P. Roushan, K. Kechedzhi, S. Boixo, S. V. Isakov, V. Smelyanskiy, A. Megrant, B. Chiaro, A. Dunsworth, K. Arya, R. Barends, B. Burkett, Y. Chen, Z. Chen, A. Fowler, B. Foxen, M. Giustina, R. Graff, E. Jeffrey, T. Huang, J. Kelly, P. Klimov, E. Lucero, J. Mutus, M. Neeley, C. Quintana, D. Sank, A. Vainsencher, J. Wenner, T. C. White,

H. Neven, and J. M. Martinis, *A blueprint for demonstrating quantum supremacy with superconducting qubits*, Science **360**, 195 (2018).

[47] H. K. Onnes, *Further experiments with liquid helium. C. On the change of electric resistance of pure metals at very low temperatures etc. IV. The resistance of pure mercury at helium temperatures*, Proc. R. Neth. Acad. Arts Sci. **13**, 1274 (1911).

[48] H. K. Onnes, *Further experiments with Liquid Helium. D. On the change of Electrical Resistance of Pure Metals at very low Temperatures, etc. V. The Disappearance of the resistance of mercury*, Proc. R. Neth. Acad. Arts Sci. **14**, 113 (1911).

[49] J. Bardeen, L. N. Cooper, and J. R. Schrieffer, *Theory of Superconductivity*, Phys. Rev. **108**, 1175 (1957).

[50] M. Tinkham, *Introduction to Superconductivity*, 2nd ed. (McGraw-Hill, Inc., 1996).

[51] A. Barone, *Physics and applications of the Josephson effect* (John Wiley & Sons, 1982).

[52] K. K. Likharev, *Dynamics of Josephson junctions and circuits* (OPA Amsterdam, B.V., 1984).

[53] G. J. Dolan, *Offset masks for lift-off photoprocessing*, Appl. Phys. Lett. **31**, 337 (1977).

[54] B. D. Josephson, *Possible new effects in superconductive tunnelling*, Phys. Lett. **1**, 251 (1962).

[55] B. D. Josephson, *The discovery of tunnelling supercurrents*, Rev. Mod. Phys. **46**, 251 (1974).

[56] P. Siekevitz, *Powerhouse of the Cell*, Sci. Am. **197**, 131 (1957).

[57] P. W. Anderson and J. M. Rowell, *Probable Observation of the Josephson Superconducting Tunneling Effect*, Phys. Rev. Lett. **10**, 230 (1963).

[58] J. Clarke, A. N. Cleland, M. H. Devoret, D. Esteve, and J. M. Martinis, *Quantum Mechanics of a Macroscopic Variable: The Phase Difference of a Josephson Junction*, Science **239**, 992 (1988).

[59] D. E. McCumber, *Effect of ac Impedance on dc Voltage-Current Characteristics of Superconductor Weak-Link Junctions*, J. Appl. Phys. **39**, 3113 (1968).

[60] W. C. Stewart, *Current-voltage characteristics of Josephson junctions*, Appl. Phys. Lett. **12**, 277 (1968).

[61] J. Koch, T. M. Yu, J. Gambetta, A. A. Houck, D. I. Schuster, J. Majer, A. Blais, M. H. Devoret, S. M. Girvin, and R. J. Schoelkopf, *Charge-insensitive qubit design derived from the cooper pair box*, Phys. Rev. A **76**, 042319 (2007).

[62] Y. Makhlin, G. Schön, and A. Shnirman, *Quantum-state engineering with Josephson-junction devices*, Rev. Mod. Phys. **73**, 357 (2001).

[63] W. D. Oliver and P. B. Welander, *Materials in superconducting quantum bits*, Mater. Res. Bull. **38**, 816 (2013).

[64] G. Wendin, *Quantum information processing with superconducting circuits: a review*, Rep. Prog. Phys. **80**, 106001 (2017).

[65] Y. Nakamura, Y. A. Pashkin, and J. S. Tsai, *Coherent control of macroscopic quantum states in a single-cooper-pair box*, Nature **398**, 786 EP (1999).

[66] J. M. Martinis, *Superconducting phase qubits*, Quantum Inf. Process. **8**, 81 (2009).

[67] I. Chiorescu, Y. Nakamura, C. J. P. M. Harmans, and J. E. Mooij, *Coherent Quantum Dynamics of a Superconducting Flux Qubit*, Science **299**, 1869 (2003).

[68] V. Bouchiat, D. Vion, P. Joyez, D. Esteve, and M. H. Devoret, *Quantum coherence with a single Cooper pair*, Phys. Scr. **1998**, 165 (1998).

[69] N. H. Bonadeo, J. Erland, D. Gammon, D. Park, D. S. Katzer, and D. G. Steel, *Coherent Optical Control of the Quantum State of a Single Quantum Dot*, Science **282**, 1473 (1998).

[70] R. C. Ramos, M. A. Gubrud, A. J. Berkley, J. R. Anderson, C. J. Lobb, and F. C. Wellstood, *Design for effective thermalization of junctions for quantum coherence*, IEEE Trans. Appl. Supercond. **11**, 998 (2001).

[71] J. M. Martinis, S. Nam, J. Aumentado, and C. Urbina, *Rabi Oscillations in a Large Josephson-Junction Qubit*, Phys. Rev. Lett. **89**, 117901 (2002).

[72] J. E. Mooij, T. P. Orlando, L. Levitov, L. Tian, C. H. van der Wal, and S. Lloyd, *Josephson Persistent-Current Qubit*, Science **285**, 1036 (1999).

[73] T. P. Orlando, J. E. Mooij, L. Tian, C. H. van der Wal, L. S. Levitov, S. Lloyd, and J. J. Mazo, *Superconducting persistent-current qubit*, Phys. Rev. B **60**, 15398 (1999).

[74] C. H. van der Wal, A. C. J. ter Haar, F. K. Wilhelm, R. N. Schouten, C. J. P. M. Harmans, T. P. Orlando, S. Lloyd, and J. E. Mooij, *Quantum Superposition of Macroscopic Persistent-Current States*, Science **290**, 773 (2000).

[75] P. Kumar, S. Sendelbach, M. A. Beck, J. W. Freeland, Z. Wang, H. Wang, C. C. Yu, R. Q. Wu, D. P. Pappas, and R. McDermott, *Origin and reduction of $1/f$ magnetic flux noise in superconducting devices*, Phys. Rev. Appl. **6**, 041001 (2016).

[76] F. C. Wellstood, C. Urbina, and J. Clarke, *Low-frequency noise in dc superconducting quantum interference devices below 1 K*, Appl. Phys. Lett. **50**, 772 (1987).

[77] M. B. Weissman, 1/f *noise and other slow, nonexponential kinetics in condensed matter*, Rev. Mod. Phys. **60**, 537 (1988).

[78] F. Yan, S. Gustavsson, A. Kamal, J. Birenbaum, A. P. Sears, D. Hover, T. J. Gudmundsen, D. Rosenberg, G. Samach, S. Weber, J. L. Yoder, T. P. Orlando, J. Clarke, A. J. Kerman, and W. D. Oliver, *The flux qubit revisited to enhance coherence and reproducibility*, Nat. Comms. **7**, 12964 (2016).

[79] P. V. Klimov, J. Kelly, Z. Chen, M. Neeley, A. Megrant, B. Burkett, R. Barends, K. Arya, B. Chiaro, Y. Chen, A. Dunsworth, A. Fowler, B. Foxen, C. Gidney, M. Giustina, R. Graff, T. Huang, E. Jeffrey, E. Lucero, J. Y. Mutus, O. Naaman, C. Neill, C. Quintana, P. Roushan, D. Sank, A. Vainsencher, J. Wenner, T. C. White, S. Boixo, R. Babbush, V. N. Smelyanskiy, H. Neven, and J. M. Martinis, *Fluctuations of Energy-Relaxation Times in Superconducting Qubits*, Phys. Rev. Lett. **121**, 090502 (2018).

[80] J. Matisoo, *Measurement of current transfer time in a tunneling cryotron flip-flop, Proceedings of the IEEE*, Proc. IEEE (Lett.) **55**, 2052 (1967).

[81] W. Anacker, *Josephson Computer Technology: An IBM Research Project*, IBM J. Res. Dev. **24**, 107 (1980).

[82] O. Mukhanov, V. Semenov, and K. Likharev, *Ultimate performance of the RSFQ logic circuits*, IEEE Trans. Magn. **23**, 759 (1987).

[83] V. K. Kaplunenko, M. I. Khabipov, V. P. Koshelets, K. K. Likharev, O. A. Mukhanov, V. K. Semenov, I. L. Serpuchenko, and A. N. Vystavkin, *Experimental study of the RSFQ logic elements*, IEEE Trans. Magn. **25**, 861 (1989).

[84] K. K. Likharev and V. K. Semenov, *RSFQ logic/memory family: a new Josephson-junction technology for sub-terahertz-clock-frequency digital systems*, IEEE Trans. Appl. Supercond. **1**, 3 (1991).

[85] V. P. Andratsky and V. S. Bobrov, *Propagation of single flux quantum pulse of superconducting transmission line*, Cryogenics **30**, 1109 (1990).

[86] S. V. Polonsky, V. K. Semenov, and D. F. Schneider, *Transmission of Single-Flux-Quantum pulses along superconducting microstrip lines*, IEEE Trans. Appl. Supercond. **3**, 2598 (1993).

[87] Y. K. Kwong and V. Nandakumar, *Experimental evaluation of the Rapid Single Flux Quantum cells*, IEEE Trans. Appl. Supercond. **3** (1993), 10.1109/77.233876.

[88] S. V. Polonsky, V. K. Semenov, P. I. Bunyk, A. F. Kirichenko, A. Y. Kidiyarova-Shevchenko, O. A. Mukhanov, P. N. Shevchenko, D. F. Schneider, D. Y. Zinoviev, and K. K. Likharev, *New RSFQ Circuits*, IEEE Trans. Appl. Supercond. **3** (1993), 10.1109/77.233530.

[89] I. I. Soloviev, N. V. Klenov, S. V. Bakurskiy, M. Y. Kupriyanov, A. L. Gudkov, and A. S. Sidorenko, *Beyond Moore's technologies: operation principles of a superconductor alternative*, Beilstein J. Nanotechnol. **8**, 2689 (2017).

[90] D. E. Kirichenko, S. Sarwana, and A. F. Kirichenko, *Zero Static Power Dissipation Biasing of RSFQ Circuits*, IEEE Trans. Appl. Supercond. **21**, 776 (2011).

[91] O. A. Mukhanov, *Energy-Efficient Single Flux Quantum Technology*, IEEE Trans. Appl. Supercond. **21**, 760 (2011).

[92] Y. Harada, H. Nakane, N. Miyamoto, U. Kawabe, E. Goto, and T. Soma, *Basic operations of the quantum flux parametron*, IEEE Trans. Magn. **23**, 3801 (1987).

[93] M. Hosoya, W. Hioe, J. Casas, R. Kamikawai, Y. Harada, Y. Wada, H. Nakane, R. Suda, and E. Goto, *Quantum flux parametron: a single quantum flux device for Josephson supercomputer*, IEEE Trans. Appl. Supercond. **1**, 77 (1991).

[94] K. Inoue, N. Takeuchi, K. Ehara, Y. Yamanashi, and N. Yoshikawa, *Simulation and Experimental Demonstration of Logic Circuits Using an Ultra-Low-Power Adiabatic Quantum-Flux-Parametron*, IEEE Trans. Appl. Supercond. **23**, 1301105 (2013).

[95] N. Takeuchi, D. Ozawa, Y. Yamanashi, and N. Yoshikawa, *An adiabatic quantum flux parametron as an ultra-low-power logic device*, Supercond. Sci. Technol. **26**, 035010 (2013).

[96] Q. P. Herr, A. Y. Herr, O. T. Oberg, and A. G. Ioannidis, *Ultra-low-power superconductor logic*, J. Appl. Phys. **109**, 103903 (2011).

[97] J. M. Raimond, M. Brune, and S. Haroche, *Manipulating quantum entanglement with atoms and photons in a cavity*, Rev. Mod. Phys. **73**, 565 (2001).

[98] H. Mabuchi and A. C. Doherty, *Cavity Quantum Electrodynamics: Coherence in Context*, Science **298**, 1372 (2002).

[99] A. Blais, R.-S. Huang, A. Wallraff, S. M. Girvin, and R. J. Schoelkopf, *Cavity quantum electrodynamics for superconducting electrical circuits: An architecture for quantum computation*, Phys. Rev. A **69**, 062320 (2004).

[100] A. Wallraff, D. I. Schuster, A. Blais, L. Frunzio, R. S. Huang, J. Majer, S. Kumar, S. M. Girvin, and R. J. Schoelkopf, *Strong coupling of a single photon to a superconducting qubit using circuit quantum electrodynamics*, Nature **431**, 162 EP (2004).

[101] L. Frunzio, A. Wallraff, D. Schuster, J. Majer, and R. Schoelkopf, *Fabrication and characterization of superconducting circuit QED devices for quantum computation*, IEEE Trans. Appl. Supercond. **15**, 860 (2005).

[102] M. Göppl, A. Fragner, M. Baur, R. Bianchetti, S. Filipp, J. M. Fink, P. J. Leek, G. Puebla, L. Steffen, and A. Wallraff, *Coplanar waveguide resonators for circuit quantum electrodynamics, Journal of Applied Physics*, J. Appl. Phys. **104**, 113904 (2008).

[103] M. H. Devoret, *Quantum Fluctuations in Electrical Circuits*, in *Les Houches, Session LXIII*, edited by S. Reynaud, E. Giacobino, and J. Zinn-Justin (Elsevier Science B.V., 1995) p. 351.

[104] S. M. Girvin, *Circuit QED: superconducting qubits coupled to microwave photons*, in *Les Houches, Session XCVI*, edited by M. H. Devoret, B. Huard, R. J. Schoelkopf, and L. F. Cugliandolo (Oxford University Press, 2011) p. 113.

[105] E. T. Jaynes and F. W. Cummings, *Comparison of quantum and semiclassical radiation theories with application to the beam maser*, Proc. IEEE **51**, 89 (1963).

[106] C. C. Gerry and P. L. Knight, *Introductory Quantum Optics* (Cambridge University Press, 2005).

[107] D. C. McKay, C. J. Wood, S. Sheldon, J. M. Chow, and J. M. Gambetta, *Efficient z gates for quantum computing*, Phys. Rev. A **96**, 022330 (2017).

[108] D. Pozar, *Microwave Engineering*, 4th ed. (John Wiley & Sons, 2012).

[109] R. Barends, N. Vercruyssen, A. Endo, P. J. de Visser, T. Zijlstra, T. M. Klapwijk, P. Diener, S. J. C. Yates, and J. J. A. Baselmans, *Minimal resonator loss for circuit quantum electrodynamics*, Appl. Phys. Lett. **97**, 023508 (2010).

[110] A. Megrant, C. Neill, R. Barends, B. Chiaro, Y. Chen, L. Feigl, J. Kelly, E. Lucero, M. Mariantoni, P. J. J. O'Malley, D. Sank, A. Vainsencher, J. Wenner, T. C. White, Y. Yin, J. Zhao, C. J. Palmstrøm, J. M. Martinis, and A. N. Cleland, *Planar superconducting resonators with internal quality factors above one million*, Appl. Phys. Lett. **100**, 113510 (2012).

[111] M. A. Beck, J. A. Isaacs, D. Booth, J. D. Pritchard, M. Saffman, and R. McDermott, *Optimized coplanar waveguide resonators for a superconductor–atom interface*, Appl. Phys. Lett. **109**, 092602 (2016).

[112] A. A. Houck, J. A. Schreier, B. R. Johnson, J. M. Chow, J. Koch, J. M. Gambetta, D. I. Schuster, L. Frunzio, M. H. Devoret, S. M. Girvin, and R. J. Schoelkopf, *Controlling the Spontaneous Emission of a Superconducting Transmon Qubit*, Phys. Rev. Lett. **101**, 080502 (2008).

[113] M. Boissonneault, J. M. Gambetta, and A. Blais, *Dispersive regime of circuit QED: Photon-dependent qubit dephasing and relaxation rates*, Phys. Rev. A **79**, 013819 (2009).

[114] M. D. Reed, L. DiCarlo, B. R. Johnson, L. Sun, D. I. Schuster, L. Frunzio, and R. J. Schoelkopf, *High-Fidelity Readout in Circuit Quantum Electrodynamics Using the Jaynes-Cummings Nonlinearity*, Phys. Rev. Lett. **105**, 173601 (2010).

[115] C. C. Bultink, B. Tarasinski, N. Haandbæk, S. Poletto, N. Haider, D. J. Michalak, A. Bruno, and L. DiCarlo, *General method for extracting the quantum efficiency of dispersive qubit readout in circuit QED*, Appl. Phys. Lett. **112**, 092601 (2018).

[116] D. Bozyigit, C. Lang, L. Steffen, J. M. Fink, C. Eichler, M. Baur, R. Bianchetti, P. J. Leek, S. Filipp, M. P. da Silva, A. Blais, and A. Wallraff, *Antibunching of microwave-frequency photons observed in correlation measurements using linear detectors*, Nat. Phys. **7**, 154 EP (2010).

[117] G. J. Ribeill, D. Hover, Y. F. Chen, S. Zhu, and R. McDermott, *Superconducting low-inductance undulatory galvanometer microwave amplifier: Theory*, J. Appl. Phys. **110**, 103901 (2011).

[118] D. Hover, Y. F. Chen, G. J. Ribeill, S. Zhu, S. Sendelbach, and R. McDermott, *Superconducting low-inductance undulatory galvanometer microwave amplifier*, Appl. Phys. Lett. **100**, 063503 (2012).

[119] R. H. Koch, D. J. Van Harlingen, and J. Clarke, *Quantum noise theory for the dc SQUID*, Appl. Phys. Lett. **38**, 380 (1981).

[120] C. M. Caves, *Quantum limits on noise in linear amplifiers*, Phys. Rev. D **26**, 1817 (1982).

[121] K. McClaning and T. Vito, *Radio Receiver Design* (Noble Pub, 2001).

[122] Low Noise Factory AB, *LNF-LNC4_8C*, Specification sheet (last accessed: August 2018).

[123] E. A. Tholén, A. Ergül, D. Schaeffer, and D. B. Haviland, *Gain, noise and intermodulation in a nonlinear superconducting resonator*, EPJ Quantum Technol. **1**, 5 (2014).

[124] B. Yurke, L. R. Corruccini, P. G. Kaminsky, L. W. Rupp, A. D. Smith, A. H. Silver, R. W. Simon, and E. A. Whittaker, *Observation of parametric amplification and deamplification in a Josephson parametric amplifier*, Phys. Rev. A **39**, 2519 (1989).

[125] M. A. Castellanos-Beltran and K. W. Lehnert, *Widely tunable parametric amplifier based on a superconducting quantum interference device array resonator*, Appl. Phys. Lett. **91**, 083509 (2007).

[126] T. Yamamoto, K. Inomata, M. Watanabe, K. Matsuba, T. Miyazaki, W. D. Oliver, Y. Nakamura, and J. S. Tsai, *Flux-driven Josephson parametric amplifier*, Appl. Phys. Lett. **93**, 042510 (2008).

[127] M. Hatridge, R. Vijay, D. H. Slichter, J. Clarke, and I. Siddiqi, *Dispersive magnetometry with a quantum limited SQUID parametric amplifier*, Phys. Rev. B **83**, 134501 (2011).

[128] B. Abdo, F. Schackert, M. Hatridge, C. Rigetti, and M. Devoret, *Josephson amplifier for qubit readout*, Appl. Phys. Lett. **99**, 162506 (2011).

[129] J. Y. Mutus, T. C. White, E. Jeffrey, D. Sank, R. Barends, J. Bochmann, Y. Chen, Z. Chen, B. Chiaro, A. Dunsworth, J. Kelly, A. Megrant, C. Neill, P. J. J. O'Malley, P. Roushan, A. Vainsencher, J. Wenner, I. Siddiqi, R. Vijay, A. N. Cleland, and J. M. Martinis, *Design and characterization of a lumped element single-ended superconducting microwave parametric amplifier with on-chip flux bias line*, Appl. Phys. Lett. **103**, 122602 (2013).

[130] J. Y. Mutus, T. C. White, R. Barends, Y. Chen, Z. Chen, B. Chiaro, A. Dunsworth, E. Jeffrey, J. Kelly, A. Megrant, C. Neill, P. J. J. O'Malley, P. Roushan, D. Sank, A. Vainsencher, J. Wenner, K. M. Sundqvist, A. N. Cleland, and J. M. Martinis, *Strong environmental coupling in a Josephson parametric amplifier*, Appl. Phys. Lett. **104**, 263513 (2014).

[131] N. Bergeal, R. Vijay, V. E. Manucharyan, I. Siddiqi, R. J. Schoelkopf, S. M. Girvin, and M. H. Devoret, *Analog information processing at the quantum limit with a Josephson ring modulator*, Nat. Phys. **6**, 296 EP (2010).

[132] N. Bergeal, F. Schackert, M. Metcalfe, R. Vijay, V. E. Manucharyan, L. Frunzio, D. E. Prober, R. J. Schoelkopf, S. M. Girvin, and M. H. Devoret, *Phase-preserving amplification near the quantum limit with a Josephson ring modulator*, Nature **465**, 64 EP (2010).

[133] B. Abdo, K. Sliwa, L. Frunzio, and M. Devoret, *Directional Amplification with a Josephson Circuit*, Phys. Rev. X **3**, 031001 (2013).

[134] B. Abdo, K. Sliwa, S. Shankar, M. Hatridge, L. Frunzio, R. Schoelkopf, and M. Devoret, *Josephson Directional Amplifier for Quantum Measurement of Superconducting Circuits*, Phys. Rev. Lett. **112**, 167701 (2014).

[135] B. Ho Eom, P. K. Day, H. G. LeDuc, and J. Zmuidzinas, *A wideband, low-noise superconducting amplifier with high dynamic range*, Nat. Phys. **8**, 623 EP (2012).

[136] C. Bockstiegel, J. Gao, M. R. Vissers, M. Sandberg, S. Chaudhuri, A. Sanders, L. R. Vale, K. D. Irwin, and D. P. Pappas, *Development of a Broadband NbTiN Traveling Wave Parametric Amplifier for MKID Readout*, J. Low Temp. Phys. **176**, 476 (2014).

[137] M. R. Vissers, R. P. Erickson, H. S. Ku, L. Vale, X. Wu, G. C. Hilton, and D. P. Pappas, *Low-noise kinetic inductance traveling-wave amplifier using three-wave mixing*, Appl. Phys. Lett. **108**, 012601 (2016).

[138] R. P. Erickson and D. P. Pappas, *Theory of multiwave mixing within the superconducting kinetic-inductance traveling-wave amplifier*, Phys. Rev. B **95**, 104506 (2017).

[139] C. Macklin, K. O'Brien, D. Hover, M. E. Schwartz, V. Bolkhovsky, X. Zhang, W. D. Oliver, and I. Siddiqi, *A near–quantum-limited Josephson traveling-wave parametric amplifier*, Science **350**, 307 (2015).

[140] T. C. White, J. Y. Mutus, I. C. Hoi, R. Barends, B. Campbell, Y. Chen, Z. Chen, B. Chiaro, A. Dunsworth, E. Jeffrey, J. Kelly, A. Megrant, C. Neill, P. J. J. O'Malley, P. Roushan, D. Sank, A. Vainsencher, J. Wenner, S. Chaudhuri, J. Gao, and J. M. Martinis, *Traveling wave parametric amplifier with Josephson junctions using minimal resonator phase matching*, Appl. Phys. Lett. **106**, 242601 (2015).

[141] A. B. Zorin, *Josephson Traveling-Wave Parametric Amplifier with Three-Wave Mixing*, Phys. Rev. Appl. **6**, 034006 (2016).

[142] D. Hover, S. Zhu, T. Thorbeck, G. J. Ribeill, D. Sank, J. Kelly, R. Barends, J. M. Martinis, and R. McDermott, *High fidelity qubit readout with the superconducting low-inductance undulatory galvanometer microwave amplifier*, Appl. Phys. Lett. **104**, 152601 (2014).

[143] T. Thorbeck, S. Zhu, E. Leonard, R. Barends, J. Kelly, J. M. Martinis, and R. McDermott, *Reverse Isolation and Backaction of the SLUG Microwave Amplifier*, Phys. Rev. Appl. **8**, 054007 (2017).

[144] Y. Liu, S. J. Srinivasan, D. Hover, S. Zhu, R. McDermott, and A. A. Houck, *High fidelity readout of a transmon qubit using a superconducting low-inductance undulatory galvanometer microwave amplifier*, New J. Phys. **16**, 113008 (2014).

[145] K. Kuroda and M. Yuda, *Niobium–stress influence on Nb/Al–oxide/Nb Josephson junctions*, J. Appl. Phys. **63**, 2352 (1988).

[146] V. Ambegaokar and A. Baratoff, *Tunneling Between Superconductors,* Phys. Rev. Lett. **10**, 486 (1963).

[147] J. Clarke, C. D. Tesche, and R. P. Giffard, *Optimization of dc SQUID voltmeter and magnetometer circuits,* J. Low Temp. Phys. **37**, 405 (1979).

[148] L. Ranzani, L. Spietz, and J. Aumentado, *Broadband calibrated scattering parameters characterization of a superconducting quantum interference device amplifier,* Appl. Phys. Lett. **103**, 022601 (2013).

[149] L. Ranzani, L. Spietz, Z. Popovic, and J. Aumentado, *Two-port microwave calibration at millikelvin temperatures,* Rev. Sci. Instrum. **84**, 034704 (2013).

[150] J. M. Martinis, S. Nam, J. Aumentado, K. M. Lang, and C. Urbina, *Decoherence of a superconducting qubit due to bias noise,* Phys. Rev. B **67**, 094510 (2003).

[151] R. J. Schoelkopf, A. A. Clerk, S. M. Girvin, K. W. Lehnert, and M. H. Devoret, *Noise and measurement backaction in superconducting circuits: qubits as spectrometers of quantum noise,* in *Proc. SPIE 5115* (2003).

[152] D. I. Schuster, A. Wallraff, A. Blais, L. Frunzio, R. S. Huang, J. Majer, S. M. Girvin, and R. J. Schoelkopf, *ac Stark Shift and Dephasing of a Superconducting Qubit Strongly Coupled to a Cavity Field,* Phys. Rev. Lett. **94**, 123602 (2005).

[153] A. P. Sears, A. Petrenko, G. Catelani, L. Sun, H. Paik, G. Kirchmair, L. Frunzio, L. I. Glazman, S. M. Girvin, and R. J. Schoelkopf, *Photon shot noise dephasing in the strong-dispersive limit of circuit QED,* Phys. Rev. B **86**, 180504 (2012).

[154] R. Barends, J. Kelly, A. Megrant, A. Veitia, D. Sank, E. Jeffrey, T. C. White, J. Mutus, A. G. Fowler, B. Campbell, Y. Chen, Z. Chen, B. Chiaro, A. Dunsworth, C. Neill, P. O'Malley, P. Roushan, A. Vainsencher, J. Wenner, A. N. Korotkov, A. N. Cleland, and J. M. Martinis, *Superconducting quantum circuits at the surface code threshold for fault tolerance,* Nature **508**, 500 (2014).

[155] D. Ristè, S. Poletto, M. Z. Huang, A. Bruno, V. Vesterinen, O. P. Saira, and L. DiCarlo, *Detecting bit-flip errors in a logical qubit using stabilizer measurements,* Nat. Comms. **6**, 6983 (2015).

[156] J. Kelly, R. Barends, A. G. Fowler, A. Megrant, E. Jeffrey, T. C. White, D. Sank, J. Y. Mutus, B. Campbell, Y. Chen, Z. Chen, B. Chiaro, A. Dunsworth, I. C. Hoi, C. Neill, P. J. J. O'Malley, C. Quintana, P. Roushan, A. Vainsencher, J. Wenner, A. N. Cleland, and J. M. Martinis, *State preservation by repetitive error detection in a superconducting quantum circuit,* Nature **519**, 66 (2015).

[157] X. Zhou, J. L. Habif, A. M. Herr, M. J. Feldman, and M. F. Bocko, *A tipping pulse scheme for a rf-SQUID qubit,* IEEE Trans. Appl. Supercond. **11**, 1018 (2001).

[158] D. S. Crankshaw, J. L. Habif, X. Zhou, T. P. Orlando, M. J. Feldman, and M. F. Bocko, *An RSFQ variable duty cycle oscillator for driving a superconductive qubit,* IEEE Trans. Appl. Supercond. **13**, 966 (2003).

[159] V. K. Semenov and D. V. Averin, *SFQ control circuits for Josephson junction qubits*, IEEE Trans. Appl. Supercond. **13**, 960 (2003).

[160] K. G. Fedorov, A. V. Shcherbakova, M. J. Wolf, D. Beckmann, and A. V. Ustinov, *Fluxon Readout of a Superconducting Qubit*, Phys. Rev. Lett. **112**, 160502 (2014).

[161] R. McDermott and M. G. Vavilov, *Accurate Qubit Control with Single Flux Quantum Pulses*, Phys. Rev. Appl. **2**, 014007 (2014).

[162] P. J. Liebermann and F. K. Wilhelm, *Optimal Qubit Control Using Single-Flux Quantum Pulses*, Phys. Rev. Appl. **6**, 024022 (2016).

[163] G. Bodenhausen, R. Freeman, and G. A. Morris, *A simple pulse sequence for selective excitation in Fourier transform NMR*, J. Magn. Reson. **23**, 171 (1976).

[164] G. A. Morris and R. Freeman, *Selective excitation in Fourier transform nuclear magnetic resonance*, J. Magn. Reson. **29**, 433 (1978).

[165] E. Magesan, J. M. Gambetta, B. R. Johnson, C. A. Ryan, J. M. Chow, S. T. Merkel, M. P. da Silva, G. A. Keefe, M. B. Rothwell, T. A. Ohki, M. B. Ketchen, and M. Steffen, *Efficient Measurement of Quantum Gate Error by Interleaved Randomized Benchmarking*, Phys. Rev. Lett. **109**, 080505 (2012).

[166] E. L. Jr., M. A. Beck, J. Nelson, B. G. Christensen, T. Thorbeck, C. Howington, A. Opremcak, I. V. Pechenezhskiy, K. Dodge, N. P. Dupuis, J. Ku, F. Schlenker, J. Suttle, C. Wilen, S. Zhu, M. G. Vavilov, B. L. T. Plourde, and R. McDermott, *Digital coherent control of a superconducting qubit*, arXiv:1806.07930 (2018).

[167] E. M. Purcell, H. C. Torrey, and R. V. Pound, *Resonance Absorption by Nuclear Magnetic Moments in a Solid*, Phys. Rev. **69**, 37 (1946).

[168] A. Rylyakov and D. Y. Zinoviev, *RSFQ Cell Library*, The State University of New York (last accessed: July 2018).

[169] S. Shapiro, *Josephson Currents in Superconducting Tunneling: The Effect of Microwaves and Other Observations*, Phys. Rev. Lett. **11**, 80 (1963).

[170] M. D. Hutchings, J. B. Hertzberg, Y. Liu, N. T. Bronn, G. A. Keefe, M. Brink, J. M. Chow, and B. L. T. Plourde, *Tunable Superconducting Qubits with Flux-Independent Coherence*, Phys. Rev. Appl. **8**, 044003 (2017).

[171] J. M. Martinis, K. B. Cooper, R. McDermott, M. Steffen, M. Ansmann, K. D. Osborn, K. Cicak, S. Oh, D. P. Pappas, R. W. Simmonds, and C. C. Yu, *Decoherence in josephson qubits from dielectric loss*, Phys. Rev. Lett. **95**, 210503 (2005).

[172] E. Knill, D. Leibfried, R. Reichle, J. Britton, R. B. Blakestad, J. D. Jost, C. Langer, R. Ozeri, S. Seidelin, and D. J. Wineland, *Randomized benchmarking of quantum gates*, Phys. Rev. A **77**, 012307 (2008).

[173] E. Magesan, J. M. Gambetta, and J. Emerson, *Scalable and Robust Randomized Benchmarking of Quantum Processes*, Phys. Rev. Lett. **106**, 180504 (2011).

[174] J. Kelly, R. Barends, B. Campbell, Y. Chen, Z. Chen, B. Chiaro, A. Dunsworth, A. G. Fowler, I. C. Hoi, E. Jeffrey, A. Megrant, J. Mutus, C. Neill, P. J. J. O'Malley, C. Quintana, P. Roushan, D. Sank, A. Vainsencher, J. Wenner, T. C. White, A. N. Cleland, and J. M. Martinis, *Optimal Quantum Control Using Randomized Benchmarking*, Phys. Rev. Lett. **112**, 240504 (2014).

[175] P. J. J. O'Malley, J. Kelly, R. Barends, B. Campbell, Y. Chen, Z. Chen, B. Chiaro, A. Dunsworth, A. G. Fowler, I. C. Hoi, E. Jeffrey, A. Megrant, J. Mutus, C. Neill, C. Quintana, P. Roushan, D. Sank, A. Vainsencher, J. Wenner, T. C. White, A. N. Korotkov, A. N. Cleland, and J. M. Martinis, *Qubit Metrology of Ultralow Phase Noise Using Randomized Benchmarking*, Phys. Rev. Appl. **3**, 044009 (2015).

[176] A. D. Córcoles, J. M. Gambetta, J. M. Chow, J. A. Smolin, M. Ware, J. Strand, B. L. T. Plourde, and M. Steffen, *Process verification of two-qubit quantum gates by randomized benchmarking*, Phys. Rev. A **87**, 030301 (2013).

[177] M. Reagor, C. B. Osborn, N. Tezak, A. Staley, G. Prawiroatmodjo, M. Scheer, N. Alidoust, E. A. Sete, N. Didier, M. P. da Silva, E. Acala, J. Angeles, A. Bestwick, M. Block, B. Bloom, A. Bradley, C. Bui, S. Caldwell, L. Capelluto, R. Chilcott, J. Cordova, G. Crossman, M. Curtis, S. Deshpande, T. El Bouayadi, D. Girshovich, S. Hong, A. Hudson, P. Karalekas, K. Kuang, M. Lenihan, R. Manenti, T. Manning, J. Marshall, Y. Mohan, W. O'Brien, J. Otterbach, A. Papageorge, J.-P. Paquette, M. Pelstring, A. Polloreno, V. Rawat, C. A. Ryan, R. Renzas, N. Rubin, D. Russel, M. Rust, D. Scarabelli, M. Selvanayagam, R. Sinclair, R. Smith, M. Suska, T.-W. To, M. Vahidpour, N. Vodrahalli, T. Whyland, K. Yadav, W. Zeng, and C. T. Rigetti, *Demonstration of universal parametric entangling gates on a multi-qubit lattice*, Sci. Adv. **4** (2018).

[178] A. W. Cross, E. Magesan, L. S. Bishop, J. A. Smolin, and J. M. Gambetta, *Scalable randomised benchmarking of non-Clifford gates*, npj Quantum Inf. **2**, 16012 EP (2016).

[179] D. C. McKay, S. Sheldon, J. A. Smolin, J. M. Chow, and J. M. Gambetta, *Three Qubit Randomized Benchmarking*, arXiv:1712.06550 (2017).

[180] J. M. Martinis, M. Ansmann, and J. Aumentado, *Energy Decay in Superconducting Josephson-Junction Qubits from Nonequilibrium Quasiparticle Excitations*, Phys. Rev. Lett. **103**, 097002 (2009).

[181] G. Catelani, J. Koch, L. Frunzio, R. J. Schoelkopf, M. H. Devoret, and L. I. Glazman, *Quasiparticle Relaxation of Superconducting Qubits in the Presence of Flux*, Phys. Rev. Lett. **106**, 077002 (2011).

[182] I. M. Pop, K. Geerlings, G. Catelani, R. J. Schoelkopf, L. I. Glazman, and M. H. Devoret, *Coherent suppression of electromagnetic dissipation due to superconducting quasiparticles*, Nature **508**, 369 (2014).

[183] U. Vool, I. M. Pop, K. Sliwa, B. Abdo, C. Wang, T. Brecht, Y. Y. Gao, S. Shankar, M. Hatridge, G. Catelani, M. Mirrahimi, L. Frunzio, R. J. Schoelkopf, L. I. Glazman, and M. H. Devoret, *Non-Poissonian Quantum Jumps of a Fluxonium Qubit due to Quasiparticle Excitations*, Phys. Rev. Lett. **113**, 247001 (2014).

[184] K. M. Lang, S. Nam, J. Aumentado, C. Urbina, and J. M. Martinis, *Banishing quasiparticles from Josephson–junction qubits: why and how to do it*, IEEE Trans. Appl. Supercond. **13**, 989 (2003).

[185] M. Lenander, H. Wang, R. C. Bialczak, E. Lucero, M. Mariantoni, M. Neeley, A. D. O'Connell, D. Sank, M. Weides, J. Wenner, T. Yamamoto, Y. Yin, J. Zhao, A. N. Cleland, and J. M. Martinis, *Measurement of energy decay in superconducting qubits from nonequilibrium quasiparticles*, Phys. Rev. B **84**, 024501 (2011).

[186] R. M. Lutchyn, L. I. Glazman, and A. I. Larkin, *Kinetics of the superconducting charge qubit in the presence of a quasiparticle*, Phys. Rev. B **74**, 064515 (2006).

[187] D. Ristè, C. C. Bultink, M. J. Tiggelman, R. N. Schouten, K. W. Lehnert, and L. DiCarlo, *Millisecond charge-parity fluctuations and induced decoherence in a superconducting transmon qubit*, Nat. Comms. **4**, 1913 EP (2013).

[188] C. Wang, Y. Y. Gao, I. M. Pop, U. Vool, C. Axline, T. Brecht, R. W. Heeres, L. Frunzio, M. H. Devoret, G. Catelani, L. I. Glazman, and R. J. Schoelkopf, *Measurement and control of quasiparticle dynamics in a superconducting qubit*, Nat. Comms. **5**, 5836 (2014).

[189] R. P. Riwar, A. Hosseinkhani, L. D. Burkhart, Y. Y. Gao, R. J. Schoelkopf, L. I. Glazman, and G. Catelani, *Normal-metal quasiparticle traps for superconducting qubits*, Phys. Rev. B **94**, 104516 (2016).

[190] U. Patel, I. V. Pechenezhskiy, B. L. T. Plourde, M. G. Vavilov, and R. McDermott, *Phonon-mediated quasiparticle poisoning of superconducting microwave resonators*, Phys. Rev. B **96**, 220501 (2017).

[191] A. Hosseinkhani, R. P. Riwar, R. J. Schoelkopf, L. I. Glazman, and G. Catelani, *Optimal Configurations for Normal-Metal Traps in Transmon Qubits*, Phys. Rev. Appl. **8**, 064028 (2017).

[192] R. P. Riwar, L. I. Glazman, and G. Catelani, *Dissipation by normal-metal traps in transmon qubits*, Phys. Rev. B **98**, 024502 (2018).

[193] J. Aumentado, M. W. Keller, J. M. Martinis, and M. H. Devoret, *Nonequilibrium Quasiparticles and* 2e *Periodicity in Single-Cooper-Pair Transistors*, Phys. Rev. Lett. **92**, 066802 (2004).

[194] L. Sun, L. DiCarlo, M. D. Reed, G. Catelani, L. S. Bishop, D. I. Schuster, B. R. Johnson, G. A. Yang, L. Frunzio, L. Glazman, M. H. Devoret, and R. J. Schoelkopf, *Measurements of Quasiparticle Tunneling Dynamics in a Band-Gap-Engineered Transmon Qubit*, Phys. Rev. Lett. **108**, 230509 (2012).

[195] I. Nsanzineza and B. L. T. Plourde, *Trapping a single vortex and reducing quasiparticles in a superconducting resonator,* Phys. Rev. Lett. **113**, 117002 (2014).

[196] S. Gustavsson, F. Yan, G. Catelani, J. Bylander, A. Kamal, J. Birenbaum, D. Hover, D. Rosenberg, G. Samach, A. P. Sears, S. J. Weber, J. L. Yoder, J. Clarke, A. J. Kerman, F. Yoshihara, Y. Nakamura, T. P. Orlando, and W. D. Oliver, *Suppressing relaxation in superconducting qubits by quasiparticle pumping,* Science **354**, 1573 (2016).

[197] R. Barends, J. Wenner, M. Lenander, Y. Chen, R. C. Bialczak, J. Kelly, E. Lucero, P. O'Malley, M. Mariantoni, D. Sank, H. Wang, T. C. White, Y. Yin, J. Zhao, A. N. Cleland, J. M. Martinis, and J. J. A. Baselmans, *Minimizing quasiparticle generation from stray infrared light in superconducting quantum circuits,* Appl. Phys. Lett. **99**, 113507 (2011).

[198] A. D. Córcoles, J. M. Chow, J. M. Gambetta, C. Rigetti, J. R. Rozen, G. A. Keefe, M. Beth Rothwell, M. B. Ketchen, and M. Steffen, *Protecting superconducting qubits from radiation,* Appl. Phys. Lett. **99**, 181906 (2011).

[199] N. F. Ramsey, *A Molecular Beam Resonance Method with Separated Oscillating Fields,* Phys. Rev. **78**, 695 (1950).

[200] J. R. Johansson, P. D. Nation, and F. Nori, *QuTiP 2: A Python framework for the dynamics of open quantum systems,* Comp. Phys. Comms. **184**, 1234 (2013).

[201] D. Rosenberg, D. Kim, R. Das, D. Yost, S. Gustavsson, D. Hover, P. Krantz, A. Melville, L. Racz, G. O. Samach, S. J. Weber, F. Yan, J. L. Yoder, A. J. Kerman, and W. D. Oliver, *3D integrated superconducting qubits,* npj Quantum Inf. **3**, 42 (2017).

[202] W. O'Brien, M. Vahidpour, J. T. Whyland, J. Angeles, J. Marshall, D. Scarabelli, G. Crossman, K. Yadav, Y. Mohan, C. Bui, V. Rawat, R. Renzas, N. Vodrahalli, A. Bestwick, and C. Rigetti, *Superconducting Caps for Quantum Integrated Circuits,* arXiv:1708.02219 (2017).

[203] Q. Liu, M. Li, K. Dai, K. Zhang, G. Xue, X. Tan, H. Yu, and Y. Yu, *Extensible 3D architecture for superconducting quantum computing,* Appl. Phys. Lett. **110**, 232602 (2017).

[204] N. T. Bronn, V. P. Adiga, S. Olivadese, X. Wu, J. Chow, and D. P. Pappas, *High coherence plane breaking packaging for superconducting qubits,* Quantum Sci. Technol. (2018).

[205] B. Foxen, J. Y. Mutus, E. Lucero, R. Graff, A. Megrant, Y. Chen, C. Quintana, B. Burkett, J. Kelly, E. Jeffrey, Y. Yang, A. Yu, K. Arya, R. Barends, Z. Chen, B. Chiaro, A. Dunsworth, A. Fowler, C. Gidney, M. Giustina, T. Huang, P. Klimov, M. Neeley, C. Neill, P. Roushan, D. Sank, A. Vainsencher, J. Wenner, T. C. White, and J. M. Martinis, *Qubit compatible superconducting interconnects,* Quantum Sci. Technol. **3**, 014005 (2018).

[206] R. Das, J. Yoder, D. Rosenberg, D. Kim, D. Yost, J. Mallek, D. Hover, V. Bolkhovsky, A. Kerman, and W. Oliver, *Cryogenic Qubit Integration for Quantum Computing*, in *IEEE 68th ECTC* (2018) pp. 504–514.

[207] O. P. Saira, J. P. Groen, J. Cramer, M. Meretska, G. de Lange, and L. DiCarlo, *Entanglement Genesis by Ancilla-Based Parity Measurement in 2D Circuit QED,* Phys. Rev. Lett. **112**, 070502 (2014).

[208] A. D. Córcoles, E. Magesan, S. J. Srinivasan, A. W. Cross, M. Steffen, J. M. Gambetta, and J. M. Chow, *Demonstration of a quantum error detection code using a square lattice of four superconducting qubits,* Nat. Comms. **6**, 6979 EP (2015).

[209] S. Caldwell, N. Didier, C. A. Ryan, E. A. Sete, A. Hudson, P. Karalekas, R. Manenti, M. Reagor, M. P. d. Silva, R. Sinclair, E. Acala, N. Alidoust, J. Angeles, A. Bestwick, M. Block, B. Bloom, A. Bradley, C. Bui, L. Capelluto, R. Chilcott, J. Cordova, G. Crossman, M. Curtis, S. Deshpande, T. E. Bouayadi, D. Girshovich, S. Hong, K. Kuang, M. Lenihan, T. Manning, A. Marchenkov, J. Marshall, R. Maydra, Y. Mohan, W. O'Brien, C. Osborn, J. Otterbach, A. Papageorge, J. P. Paquette, M. Pelstring, A. Polloreno, G. Prawiroatmodjo, V. Rawat, R. Renzas, N. Rubin, D. Russell, M. Rust, D. Scarabelli, M. Scheer, M. Selvanayagam, R. Smith, A. Staley, M. Suska, N. Tezak, D. C. Thompson, T. W. To, M. Vahidpour, N. Vodrahalli, T. Whyland, K. Yadav, W. Zeng, and C. Rigetti, *Parametrically Activated Entangling Gates Using Transmon Qubits,* arXiv:1706.06562 (2017).

[210] S. Krinner, S. Storz, P. Kurpiers, P. Magnard, J. Heinsoo, R. Keller, J. Luetolf, C. Eichler, and A. Wallraff, *Engineering cryogenic setups for 100-qubit scale superconducting circuit systems,* arXiv:1806.07862 (2018).

[211] R. McDermott, M. G. Vavilov, B. L. T. Plourde, F. K. Wilhelm, P. J. Liebermann, O. A. Mukhanov, and T. A. Ohki, *Quantum–classical interface based on single flux quantum digital logic,* Quantum Sci. Technol. **3**, 024004 (2018).

[212] J. M. Hornibrook, J. I. Colless, I. D. Conway Lamb, S. J. Pauka, H. Lu, A. C. Gossard, J. D. Watson, G. C. Gardner, S. Fallahi, M. J. Manfra, and D. J. Reilly, *Cryogenic Control Architecture for Large-Scale Quantum Computing,* Phys. Rev. Appl. **3**, 024010 (2015).

[213] D. J. Reilly, *Engineering the quantum-classical interface of solid-state qubits,* npj Quantum Inf. **1**, 15011 EP (2015).

[214] I. D. Conway Lamb, J. I. Colless, J. M. Hornibrook, S. J. Pauka, S. J. Waddy, M. K. Frechtling, and D. J. Reilly, *An FPGA-based instrumentation platform for use at deep cryogenic temperatures,* Rev. Sci. Instrum. **87**, 014701 (2016).

[215] H. Homulle, S. Visser, and E. Charbon, *A Cryogenic 1 GSa/s, Soft-Core FPGA ADC for Quantum Computing Applications, IEEE Transactions on Circuits and Systems I: Regular Papers*, IEEE Trans. Circuits Syst. {I} **63**, 1854 (2016).

[216] H. Homulle, S. Visser, B. Patra, G. Ferrari, E. Prati, F. Sebastiano, and E. Charbon, *A reconfigurable cryogenic platform for the classical control of quantum processors, Review of Scientific Instruments*, Review of Scientific Instruments **88**, 045103 (2017).

[217] F. Sebastiano, H. Homulle, B. Patra, R. Incandela, J. van Dijk, L. Song, M. Babaie, A. Vladimirescu, and E. Charbon, *Cryo-CMOS Electronic Control for Scalable Quantum Computing*, in *Proc. 54th Annual Design Automation Conf.*, DAC '17 (ACM, New York, NY, USA, 2017) pp. 13:1–13:6.

[218] P. I. Bunyk, E. M. Hoskinson, M. W. Johnson, E. Tolkacheva, F. Altomare, A. J. Berkley, R. Harris, J. P. Hilton, T. Lanting, A. J. Przybysz, and J. Whittaker, *Architectural Considerations in the Design of a Superconducting Quantum Annealing Processor*, IEEE Trans. Appl. Supercond. **24**, 1 (2014).

[219] M. G. Castellano, L. Grönberg, P. Carelli, F. Chiarello, C. Cosmelli, R. Leoni, S. Poletto, G. Torrioli, J. Hassel, and P. Helistö, *Characterization of a fabrication process for the integration of superconducting qubits and rapid-single-flux-quantum circuits*, Supercond. Sci. Technol. **19**, 860 (2006).

[220] J. N. Ullom, P. A. Fisher, and M. Nahum, *Measurements of quasiparticle thermalization in a normal metal*, Phys. Rev. B **61**, 14839 (2000).

[221] J. P. Pekola, D. V. Anghel, T. I. Suppula, J. K. Suoknuuti, A. J. Manninen, and M. Manninen, *Trapping of quasiparticles of a nonequilibrium superconductor*, Appl. Phys. Lett. **76**, 2782 (2000).

[222] F. Giazotto, T. T. Heikkilä, A. Luukanen, A. M. Savin, and J. P. Pekola, *Opportunities for mesoscopics in thermometry and refrigeration: Physics and applications*, Rev. Mod. Phys. **78**, 217 (2006).

[223] J. T. Muhonen, M. Meschke, and J. P. Pekola, *Micrometre-scale refrigerators*, Rep. Prog. Phys. **75**, 046501 (2012).